



# Tracing the Coevolution Path of Supermassive Black Holes and Spheroids with AKARI-selected Ultraluminous IR Galaxies at Intermediate Redshifts

Xiaoyang Chen<sup>1,2,3</sup> , Masayuki Akiyama<sup>1</sup> , Kohei Ichikawa<sup>1,2</sup> , Hirofumi Noda<sup>4</sup>, Yoshiaki Toba<sup>5,6,7</sup> , Issei Yamamura<sup>8,9</sup>,  
Toshihiro Kawaguchi<sup>10</sup> , Abdurro' UF<sup>6</sup> , and Mitsuru Kokubo<sup>1</sup>

<sup>1</sup> Astronomical Institute, Tohoku University, 6-3 Aramaki, Aoba-ku, Sendai, Miyagi 980-8578, Japan; [xy.chen@astr.tohoku.ac.jp](mailto:xy.chen@astr.tohoku.ac.jp)

<sup>2</sup> Frontier Research Institute for Interdisciplinary Sciences, Tohoku University, Sendai 980-8578, Japan

<sup>3</sup> ALMA Project, National Astronomical Observatory of Japan, 2-21-1, Osawa, Mitaka, Tokyo 181-8588, Japan

<sup>4</sup> Department of Earth and Space Science, Graduate School of Science, Osaka University, 1-1 Machikaneyama-cho, Toyonaka-shi, Osaka 560-0043, Japan

<sup>5</sup> Department of Astronomy, Kyoto University, Kitashirakawa-Oiwake-cho, Sakyo-ku, Kyoto 606-8502, Japan

<sup>6</sup> Academia Sinica Institute of Astronomy and Astrophysics, 11F of Astronomy-Mathematics Building, AS/NTU, No.1, Section 4, Roosevelt Road, Taipei 10617, Taiwan

<sup>7</sup> Research Center for Space and Cosmic Evolution, Ehime University, 2-5 Bunkyo-cho, Matsuyama, Ehime 790-8577, Japan

<sup>8</sup> Institute of Space and Astronautical Science, JAXA, 3-1-1 Yoshinodai, Chuo-ku, Sagami-hara, Kanagawa 252-5210, Japan

<sup>9</sup> Department of Space and Astronautical Science, SOKENDAI, 3-1-1 Yoshinodai, Chuo-ku, Sagami-hara, Kanagawa 252-5210, Japan

<sup>10</sup> Department of Economics, Management and Information Science, Onomichi City University, Hisayamada 1600-2, Onomichi, Hiroshima 722-8506, Japan

Received 2019 October 30; revised 2020 July 9; accepted 2020 July 12; published 2020 August 31

## Abstract

We present the stellar population and ionized-gas outflow properties of ultraluminous IR galaxies (ULIRGs) at  $z = 0.1\text{--}1.0$  that are selected from the AKARI far-IR all-sky survey. We construct a catalog of 1077 ULIRGs to examine feedback effects after major mergers. Of the 1077 ULIRGs, 202 are spectroscopically identified by SDSS and Subaru/FOCAS observations. Thanks to the deeper depth and higher resolution of AKARI compared to the previous Infrared Astronomical Satellite (IRAS) survey and reliable identification from the Wide-field Infrared Survey Explorer (WISE) mid-IR pointing, the sample is unique in identifying optically faint ( $i \sim 20$ ) IR-bright galaxies, which could be missed in previous surveys. A self-consistent spectrum and broadband spectral energy distribution (SED) decomposition method, which constrains stellar population properties in SED modeling based on spectral fitting results, has been employed for 149 ULIRGs whose optical continua are dominated by host galaxies. They are massive galaxies ( $M_{\text{star}} \sim 10^{11}\text{--}10^{12} M_{\odot}$ ) associated with intense star formation activities ( $\text{SFR} \sim 200\text{--}2000 M_{\odot} \text{ yr}^{-1}$ ). The sample covers a range of active galactic nucleus (AGN) bolometric luminosity of  $10^{10}\text{--}10^{13} L_{\odot}$ , and the outflow velocity measured from the [O III] 5007 Å line shows a correlation with AGN luminosity. Eight galaxies show extremely fast outflows with velocity up to  $1500\text{--}2000 \text{ km s}^{-1}$ . However, the coexistence of vigorous starbursts and strong outflows suggests the star formation has not been quenched during the ULIRG phase. By deriving the stellar mass and mass fraction of the young stellar population, we find no significant discrepancies between stellar properties of ULIRGs with weak and powerful AGNs. The results are not consistent with the merger-induced evolutionary scenario, which predicts that star formation-dominated ULIRGs will show smaller stellar masses and younger stellar populations compared to AGN-dominated ULIRGs.

*Unified Astronomy Thesaurus concepts:* [Ultraluminous infrared galaxies \(1735\)](#); [Infrared galaxies \(790\)](#); [Active galactic nuclei \(16\)](#); [Galaxy evolution \(594\)](#); [AGN host galaxies \(2017\)](#); [Starburst galaxies \(1570\)](#)

## 1. Introduction

Major mergers (interacting galaxies with a mass ratio smaller than three; e.g., Toomre 1977; Mihos & Hernquist 1996) of gas-rich disk galaxies are considered as the predominant mechanism to form the most massive supermassive black holes (SMBHs) and spheroidal populations in the universe from the normal spiral disk galaxies with moderately luminous active galactic nuclei (AGNs; e.g., Kauffmann & Haehnelt 2000; Hopkins et al. 2006; Bridge et al. 2007; Kartaltepe et al. 2010). According to the merger-induced scenario, ultraluminous IR galaxies (ULIRGs;  $L_{8\text{--}1000\mu\text{m}} > 10^{12} L_{\odot}$ ; e.g., Sanders et al. 1988) appear during the final coalescence of the galaxies after the massive inflows of cool gas triggering intense starbursts (SBs) in the nuclear regions (e.g., Sanders & Mirabel 1996; Rigopoulou et al. 1999; Dasyra et al. 2006; Hopkins et al. 2008). The massive inflowing gas also feeds the rapid growth of SMBHs, although they are initially small compared to the newly forming spheroid. The intense star formation (SF) activities enhance the formation of dust grains, which in turn attenuate the UV/optical radiation of young stars and AGNs

and reemit in the IR/submillimeter wavelength range. As a result of the rapid growth of SMBHs, the ULIRGs migrate from the previous SF-dominated phase to the AGN-dominated phase, with young post-SB stellar populations and bright but highly dust-reddened quasars (e.g., red quasars, Glikman et al. 2007; Urrutia et al. 2008; extremely red quasars, Ross et al. 2015; Goulding et al. 2018). The luminous quasars could ignite powerful outflowing wind and expel the remaining gas and dust out of the galaxies. The lifetime of ULIRGs is limited (e.g.,  $< 100 \text{ Myr}$ ; Inayoshi et al. 2018) due to the quick consumption of gas by the intense SF and the dispersion of gas by the supernova- and/or AGN-driven outflow, and the galaxies eventually evolve into elliptical galaxies with old stellar populations that host the typical unobscured quasars.

Recently, signatures of outflowing gas in multiphase have been found in various ULIRGs (neutral gas, Rupke & Veilleux 2011; Perna et al. 2015; ionized gas, Soto et al. 2012; Rodríguez Zaurín et al. 2013; Toba et al. 2017a; and molecular gas, Veilleux et al. 2013; Saito et al. 2017). Furthermore, spatially resolved spectroscopic observations of

ULIRGs show signatures that the outflows affect gas not only in their central nuclear regions ( $<1$  kpc scale) but also in their outer regions (1–10 kpc scale). For example, Westmoquette et al. (2012) presented integral field spectroscopic maps of 18 southern ULIRGs and found that 11 of them show evidence of spatially extended outflowing warm ionized gas. Harrison et al. (2012) presented kinematic measurements of eight ULIRGs at  $1.4 < z < 3.4$  and reported that in four of them, strong outflow signatures of the [O III] 5007 Å emission line with an FWHM of 700–1400 km s<sup>-1</sup> extends to a large scale (4–15 kpc) from the nucleus with large velocity offsets from the systemic redshifts (up to 850 km s<sup>-1</sup>). Chen et al. (2019) reported a discovery of a ULIRG that shows a fast outflow ( $v_{\text{out}} \sim 2000$  km s<sup>-1</sup>) extending to a radius of 4 kpc. Those observations support the idea that outflow plays an important role in the transition of a ULIRG from a vigorous SB to a quiescent galaxy.

The outflow in a ULIRG is expected to quench its vigorous SF; as a result, it is expected that the early-stage, SF-dominated ULIRGs have younger stellar populations than the late-stage, AGN-dominated ULIRGs (Netzer et al. 2007; Veilleux et al. 2009). Hou et al. (2011) investigated the stellar population of 160 Infrared Astronomical Satellite (IRAS)-selected ULIRGs and found that the mean stellar age and mass increase from SF- to AGN-dominated ULIRGs. However, the evolution sequence was questioned by other works on stellar populations of ULIRGs (e.g., Rodríguez Zaurín et al. 2010; Su et al. 2013), making the evolutionary path of ULIRGs still not conclusive. Systematic research on the properties of a large sample of ULIRGs is still required for better understanding of the evolutionary path of ULIRGs and their role in the coevolution of SMBHs and massive galaxies.

In this paper, in order to constrain the stellar population and outflow properties of ULIRGs, we apply a self-consistent spectrum and broadband spectral energy distribution (SED) analysis for 149 AKARI-selected ULIRGs whose optical spectra are dominated by their host galaxies (HGs). The construction of this ULIRG sample is introduced in Section 2. The details of the self-consistent spectrum-SED analysis method are explained in Section 3. In Section 4, we report the results on the properties of AGNs, HGs, and outflowing gas. The evolutionary scenario of the ULIRG population is discussed in Section 5 and the conclusion is summarized in Section 6. Throughout the paper, we adopt the cosmological parameters  $H_0 = 70$  km s<sup>-1</sup> Mpc<sup>-1</sup>,  $\Omega_m = 0.3$ , and  $\Omega_\Lambda = 0.7$ .

## 2. Sample Construction

### 2.1. Selection of Far-IR Sources from AKARI Catalog

The AKARI all-sky survey possesses higher spatial resolution than the previous far-infrared (FIR) all-sky survey by IRAS (e.g., 0.5–0.8 compared to 6') and is also deeper in wavelength around 90–100  $\mu\text{m}$ . The AKARI Far-Infrared Surveyor (FIS) Bright Source Catalogue (version 2, hereafter FISBSCv2;<sup>11</sup> Yamamura et al. 2016) contains a total of 918,056 sources observed at 65, 90, 140, and 160  $\mu\text{m}$ , in which 501,444 sources are detected in the main catalog.<sup>12</sup> The

FISBSCv2 covers 98% of the sky at 65 and 90  $\mu\text{m}$  and 99% of the sky at 140 and 160  $\mu\text{m}$ . The detection limit is 2.4, 0.44, 3.4, and 7.5 Jy at 65, 90, 140, and 160  $\mu\text{m}$ , respectively. In particular, the AKARI FIR survey provides the deepest data in terms of the FIR all-sky survey and thus provides a unique data set to construct a large sample of ULIRGs (e.g., Goto et al. 2011; Kilerci Eser et al. 2014; Toba et al. 2017b).

Since the Wide-S band (90  $\mu\text{m}$ ) is deeper than the other three bands of AKARI/FIS, we select FIR sources from the entire AKARI catalog (main + supplemental) with a signal-to-noise ratio (S/N) of at least 3 and high quality (fqual90 = 3) in the Wide-S band. In order to avoid the contamination of Galactic cirrus emission, we limited the sample to sources at least 5' away from any dusty regions with Galactic extinction  $E(B - V) > 0.10$  using the Galactic foreground dust map from Schlegel et al. (1998) and updated by Schlafly & Finkbeiner (2011). Additionally, in order to avoid the contamination from FIR flux of nearby bright galaxies, we ignore the AKARI sources within 0'.5 to the edge of those galaxies, which is selected from the HyperLEDA database (Makarov et al. 2014) with a diameter over 0'.5 in the major axis and total *I*-band magnitude brighter than 15. The size of the nearby bright galaxy in the direction to a given AKARI source is estimated assuming an elliptical morphology. Finally, 72,950 out of 918,056 AKARI 90  $\mu\text{m}$  sources are selected following the above conditions.

### 2.2. Cross-match of AKARI Sources with SDSS and WISE Catalogs

The 72,950 selected AKARI 90  $\mu\text{m}$  sources are then cross-matched with the Sloan Digital Sky Survey (SDSS) and Wide-field Infrared Survey Explorer (WISE) catalogs to identify their optical and mid-IR (MIR) counterparts. WISE possesses a deep detection depth ( $\sim 1$  mJy in the W3 band) and high spatial resolution ( $\sim 6''$  in the W1–W3 bands) and is useful to narrow down the positional uncertainty of the AKARI FIR sources.

The SDSS Data Release 15 (DR15; Aguado et al. 2019) is the third data release of SDSS-IV, which contains the recalibrated SDSS imaging catalogs, using the hypercalibration to PanSTARRS-1 implemented by Finkbeiner et al. (2016). The limiting magnitudes (95% completeness for point sources) are 22.0, 22.2, 22.2, 21.3, and 20.5 in the *u*, *g*, *r*, *i*, and *z* bands, respectively. We retrieved a model magnitude (called modelMag) in the five bands from the SDSS DR15 SkyServer.<sup>13</sup> The model magnitude is measured consistently through the same model profile in all bands, which is a good estimate of the total flux for extended sources, and provides an estimate of the unbiased colors of galaxies. The sources are selected with  $S/N > 5$  in the *i* band (i.e., modelMagerr\_i < 0.22). In order to avoid objects with unreliable photometry, we focus on the objects that have the photometric calibration status in the *i* band and matches the clean photometry flags.<sup>14</sup> The SDSS model magnitude was converted to flux following Stoughton et al. (2002). The Galactic extinction in the five bands is corrected with the dust map of Schlafly & Finkbeiner (2011) and the extinction law of Fitzpatrick (1999).

WISE performed an all-sky survey at 3.4 (W1), 4.6 (W2), 12 (W3), and 22 (W4)  $\mu\text{m}$  with angular resolutions of 6.1, 6.4, 6.5, and 12''.0, respectively (Wright et al. 2010). We queried the

<sup>11</sup> [https://www.ir.isas.jaxa.jp/AKARI/Observation/update/20160425\\_preliminary\\_release.html](https://www.ir.isas.jaxa.jp/AKARI/Observation/update/20160425_preliminary_release.html)

<sup>12</sup> The source in the FISBSCv2 main catalog is confirmed in two or more bands or detected in four or more scans in one band, while the source in the FISBSCv2 supplemental catalog is detected in only one band and two or three scans. See release note of FISBSCv2 catalog for details.

<sup>13</sup> <http://skyserver.sdss.org/dr15>

<sup>14</sup> <https://www.sdss.org/dr15/tutorials/flags/>

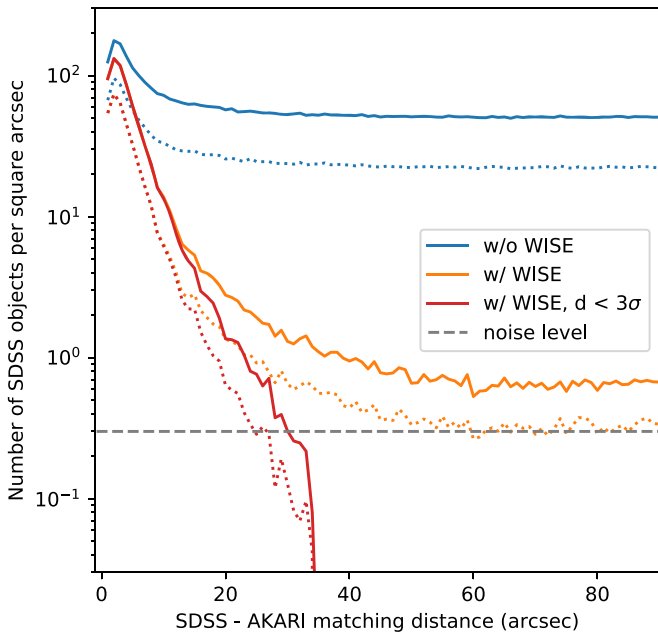


**Figure 1.** Number of SDSS counterparts per square arcsecond of the entire AKARI sample as a function of matching radius (blue). The associations that only contain the SDSS objects associated with the WISE W3-band detections are shown in orange. The SDSS-WISE associations within a searching radius of  $3\sigma_{\text{pos}}$  are shown in red. The solid and dotted curves denote the objects in the entire searching sky area and a rectangular SDSS survey region (R.A. =  $120^\circ$ – $250^\circ$ , decl. =  $0^\circ$ – $60^\circ$ ), respectively. The gray dashed line denotes the the contamination level for the cross-matching, i.e.,  $n_{\text{noise}} * N_A$ , where  $N_A = 11,539$  is the number of AKARI sources that have at least one SDSS counterpart associated with WISE detections in the rectangle region, and  $n_{\text{noise}}$  is the number of random SDSS-AKARI associations per square arcsecond per AKARI sources.

NASA/IPAC Infrared Science Archive (IRSA) for W1–W4 profile-fit magnitudes from the AllWISE Source Catalog (Cutri et al. 2014). In order to obtain reliable entries in the AllWISE catalog, the selection is limited to sources with  $S/N \geq 5$  in the W3 band. In addition, we only select sources that have a depth of coverage of at least 5 ( $W3m \geq 5$ ) and are not flagged as spurious detections of image artifacts in any band ( $cc\_flags = "0000"$ ). The WISE Vega magnitude was converted to flux densities with the flux and color corrections reported in Wright et al. (2010). We corrected for the Galactic extinction in the W1 and W2 bands using the dust map of Schlafly & Finkbeiner (2011) and the extinction law of Indebetouw et al. (2005).

Figure 1 shows the distribution of matching distances between AKARI sources and their possible optical counterparts. Duplicate matches, i.e., several SDSS objects associated with one AKARI object, are included in Figure 1 (blue curve). In this work, we only selected the SDSS objects associated with WISE W3-band detections (orange curve in Figure 1) as the candidates of true SDSS-AKARI associations. With a higher resolution ( $\sim 6''$  in the W1–W3 bands) than AKARI ( $\sim 40''$  in the Wide-S band), the WISE detections can effectively reduce the contamination from IR-faint SDSS sources. The WISE catalog is deep enough ( $\sim 1$  mJy in the W3 band) to detect FIR-dominated SB galaxies detected in the AKARI Wide-S band.

The positional uncertainties of the AKARI observations are required to determine a searching radius for the cross-matching. The release note of the FISBSCv2 catalog reported the cross-matching with the Two Micron All Sky Survey (2MASS)

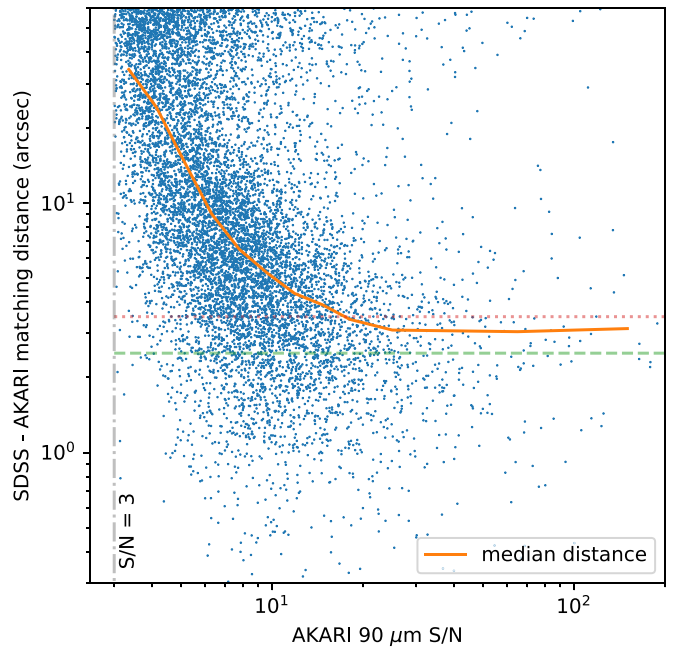


**Figure 2.** Relationship between AKARI  $90\ \mu\text{m}$  S/N and SDSS-AKARI matching distance. Only 9544 unique matches (every AKARI source has only one SDSS counterpart associated with WISE detection) within  $60''$  are shown in the plot (blue dots). The median distance per logarithmically spaced bin is shown with the orange solid line, which is used to estimate the positional uncertainty. The horizontal lines show the AKARI positional error levels in the major ( $3.5''$ ; red dotted) and minor ( $2.5''$ ; green dashed) axes reported in the release note of the FISBSCv2 catalog.

Redshift Survey Catalog (2MRS; Huchra et al. 2012) within  $30''$  and shown that 9128 AKARI sources have 2MRS counterparts. The positional errors ( $3.5''$  in the major axis and  $2.5''$  in the minor axis) recorded in the FISBSCv2 catalog are the standard deviation of the positional differences of the 9128 AKARI-2MRS associations, which could be a good proxy of the positional uncertainty of bright sources. However, ULIRGs usually appear at flux range close to the detection limit; the positional uncertainties of these faint sources could be larger. Figure 2 shows the distribution of the SDSS-AKARI matching distance as a function of AKARI  $90\ \mu\text{m}$  S/N with a searching radius of  $60''$ . Only 9544 unique matches, i.e., only one SDSS object found within  $60''$  for each AKARI source, are plotted in Figure 2. The distribution indicates that the positional uncertainty depends on the  $90\ \mu\text{m}$  S/N. Since the coordinate differences of the matching in R.A. and decl. ( $d_{\text{R.A.}}$  and  $d_{\text{decl.}}$ ) follow a Gaussian distribution with a mean of zero and variance of  $\sigma^2$ , the average of the matching distance with the definition  $[d_{\text{R.A.}}^2 + d_{\text{decl.}}^2]^{1/2}$  in each S/N bin can be a good estimate of  $\sigma$ . We derive the median distance in each logarithmically spaced S/N bin (orange curve in Figure 2), and the positional error ( $\sigma_{\text{pos}}$ ) for each AKARI source is estimated with linear interpolation; then, we employ  $3\sigma_{\text{pos}}$  as the searching radius for SDSS-AKARI associations. Selected are 14,680 SDSS objects for 12,310 AKARI sources within  $3\sigma_{\text{pos}}$  radius.

In order to discuss the completeness of the cross-matching for the AKARI catalog, we focus on a rectangular sky region (R.A. =  $120^\circ$ – $250^\circ$ , decl. =  $0^\circ$ – $60^\circ$ ) that is fully covered by the SDSS survey, in which 5641 AKARI sources show SDSS-WISE counterparts within a  $3\sigma_{\text{pos}}$  radius. Considering the total number of AKARI sources in the focused region, the  $3\sigma_{\text{pos}}$  selection covers  $5641/11,539 \simeq 49\%$  of the sources in the

entire AKARI catalog. The matching ratios are  $3922/5477 \simeq 72\%$  and  $1719/6062 \simeq 28\%$  for the FISBSCv2 main and supplemental catalogs, respectively. For the remaining 1558 (4345) AKARI sources without SDSS-WISE counterparts in the main (supplemental) catalog, 205 (296) AKARI sources do not show any SDSS counterparts within a  $3\sigma_{\text{pos}}$  matching radius; 158 (342) AKARI sources do not show any WISE counterparts within a  $3\sigma_{\text{pos}}$  matching radius; 513 (315) and 444 (196) AKARI sources are removed due to bad image quality in the SDSS  $i$  band and WISE W3 band, respectively; and 35 (96) and 388 (3602) AKARI sources are removed due to the low S/N of the SDSS-WISE counterparts in the  $i$  and W3 bands, respectively. If we ignore the failed cases due to bad image quality in the  $i$  or W3 band, the completeness is 84% and 31% for the FISBSCv2 main and supplemental catalogs, respectively. If we employ a  $5\sigma_{\text{pos}}$  selection radius and again ignore the failed cases due to bad image quality in the  $i$  or W3 band, the completeness of the supplemental catalog increases to 39%, but it stays the same for the main catalog. The origins of the unmatched AKARI sources could be the cirrus dust emission heated by remote stars in the Milky Way or the artificial objects in the FISBSCv2 catalog, e.g., side-lobe false sources.

The reliability of the cross-matching is evaluated in two ways, i.e., the contamination level from matching by chance and the likelihood of true associations in matching with multiple objects. We again focus on the rectangular sky region (R.A. =  $120^\circ$ – $250^\circ$ , decl. =  $0^\circ$ – $60^\circ$ ) to determine the contamination level. The contamination level of the cross-matching for the entire AKARI sample in the focused R.A. and decl. ranges can be described as  $n_{\text{noise}}^* N_A$ , where  $N_A = 11,539$  is the total number of AKARI sources in the rectangular region. Here  $n_{\text{noise}}$  is the number density of random SDSS-AKARI associations per square arcsecond per AKARI sources, which is estimated to be  $0.3/N_A \simeq 2 \times 10^{-5} \text{ arcsec}^{-2}$  from Figure 1. The expectation of random associations for an AKARI source within a given searching radius ( $3\sigma_{\text{pos}}$ ) can be assumed as  $9\pi\sigma_{\text{pos}}^2 n_{\text{noise}}$ . If  $n_{\text{match}}$  SDSS objects with WISE detections are found within  $3\sigma_{\text{pos}}$ , for each of the SDSS objects with WISE detections, the probability of a stochastic match is  $9\pi\sigma_{\text{pos}}^2 n_{\text{noise}}/n_{\text{match}}$ , which is used to evaluate the contamination level of a given association. Of the cross-matched SDSS counterparts within  $3\sigma_{\text{pos}}$ , 97% show contamination levels smaller than 3%.

For multiple SDSS objects associated with a given AKARI source, the likelihood ratio of each SDSS object can be defined as (e.g., Hwang et al. 2007)

$$\text{LR}_{\text{SA}} = \frac{\exp(-\frac{r_{\text{SA}}^2}{2\sigma_{\text{SA}}^2})}{N_{i < i_0}}, \quad (1)$$

where  $r_{\text{SA}}$  is the distance for each SDSS-AKARI association;  $\sigma_{\text{SA}}^2 = \sigma_{\text{SDSS}}^2 + \sigma_{\text{AKARI}}^2$ , where  $\sigma_{\text{SDSS}}$  and  $\sigma_{\text{AKARI}}$  are the positional errors of the SDSS and AKARI sources; and  $N_{i < i_0}$  denotes the number of galaxies with an  $i$ -band flux brighter than this object with an  $i$ -band magnitude  $i_0$ . The probability of an SDSS candidate being a real counterpart can be defined as  $p_{\text{SA}} = \text{LR}_{\text{SA}} / \sum_{i=1}^N \text{LR}_{\text{SA},i}$ , where  $N$  denotes the number of SDSS candidates associated with a given AKARI source. With WISE photometry as an intermediate step to connect SDSS and AKARI objects, we can also calculate the likelihood ratios for the SDSS-WISE matches and WISE-AKARI matches using

similar definitions as

$$\text{LR}_{\text{SW}} = \frac{\exp(-\frac{r_{\text{SW}}^2}{2\sigma_{\text{SW}}^2})}{N_{i < i_0}}, \quad \text{LR}_{\text{WA}} = \frac{\exp(-\frac{r_{\text{WA}}^2}{2\sigma_{\text{WA}}^2})}{N_{\text{W3} < \text{W3}_0}}, \quad (2)$$

where  $r_{\text{SW}}$  and  $r_{\text{WA}}$  are the matching distances for each SDSS-WISE and WISE-AKARI association;  $\sigma_{\text{SW}}^2 = \sigma_{\text{SDSS}}^2 + \sigma_{\text{WISE}}^2$  and  $\sigma_{\text{WA}}^2 = \sigma_{\text{WISE}}^2 + \sigma_{\text{AKARI}}^2$ , where  $\sigma_{\text{WISE}}$  is the positional error of WISE photometry; and  $N_{\text{W3} < \text{W3}_0}$  denotes the number of galaxies with a W3 band flux brighter than this object. Here  $N_{i < i_0}$  and  $N_{\text{W3} < \text{W3}_0}$  can be estimated from the cumulative functions of magnitude distributions in the  $i$  and W3 bands for the entire SDSS and WISE samples. The probabilities of SDSS-WISE matches and WISE-AKARI matches can be estimated by normalizing the  $\text{LR}_{\text{SW}}$  and  $\text{LR}_{\text{WA}}$ , respectively, i.e.,  $p_{\text{SW}} = \text{LR}_{\text{SW}} / \sum_{i=1}^{N_{\text{SW}}} \text{LR}_{\text{SW},i}$ , where  $N_{\text{SW}}$  is the number of SDSS candidates associated with a given WISE source within  $3''$ , and  $p_{\text{WA}} = \text{LR}_{\text{WA}} / \sum_{i=1}^{N_{\text{WA}}} \text{LR}_{\text{WA},i}$ , where  $N_{\text{WA}}$  is the number of WISE candidates associated with a given AKARI source within  $3\sigma_{\text{pos}}$ . In order to take advantage of the better positional accuracy of WISE ( $<0''.5$ ) to reduce the number of SDSS candidates and enlarge the cross-matched catalog, we employ the selection threshold of  $p_{\text{SW}} > 0.9$  and  $p_{\text{WA}} > 0.9$ , instead of  $p_{\text{SA}} > 0.9$ . The selection provides a reliable catalog with 11,245 SDSS-WISE-AKARI associations out of 12,310 AKARI sources with 14,680 SDSS counterparts (Figure 3).

In addition to the likelihood method with WISE detections, the sample is also cross-matched with the Faint Images of the Radio Sky at Twenty cm (FIRST) survey catalog<sup>15</sup> of radio sources in 1.4 GHz. Selected are 759,427 FIRST sources with  $P(S) < 0.1$ , where  $P(S)$  indicates the probability that the source is spurious, e.g., a side lobe of a nearby bright source. Similar to Equation (2), we also calculate the likelihood ratio and probabilities for SDSS-FIRST matches ( $p_{\text{SF}}$ ) and FIRST-AKARI matches ( $p_{\text{FA}}$ ). Among all of the SDSS-AKARI associations, 4557 galaxies are identified with FIRST detections, i.e.,  $p_{\text{SF}} > 0.9$  and  $p_{\text{FA}} > 0.9$ . Of the 4557 galaxies, 355 are ruled out in the above SDSS-WISE-AKARI identifications with a low likelihood, i.e.,  $p_{\text{SW}} < 0.9$  or  $p_{\text{WA}} < 0.9$ . We add 341 of the 355 new SDSS-AKARI associations to the matched catalog, except for 14 conflicting cases, which means that for a given AKARI source, the cross-matching with FIRST observations indicates a different primary SDSS counterpart from the one selected with WISE identification (i.e., in the conflicting case, we choose WISE-identified sources instead of FIRST-identified sources). Finally, we obtain a cross-matched catalog with 11,586 galaxies.

Among the 11,586 sources, 5247 objects are spectroscopically identified in SDSS legacy and BOSS surveys. The SDSS spectroscopic objects are selected with median S/N (snMedian)  $> 2$  and plate quality of “good” or “marginal,” as well as  $z\text{Warning} < 2^7$  (to avoid no-data for the fiber, bad targeting or unplugged fiber) and  $z\text{Warning} \neq 1$  (to avoid too little wavelength coverage). The SDSS photometric redshift is available for 6119 of the 6339 sources without spectroscopic observation, which is estimated using the kd-tree nearest-neighbor fit method.<sup>16</sup> The redshift information is not available

<sup>15</sup> [http://sundog.stsci.edu/first/catalogs/readme\\_14dec17.html](http://sundog.stsci.edu/first/catalogs/readme_14dec17.html)

<sup>16</sup> <https://www.sdss.org/dr12/algorithms/photoz/>

**Table 1**  
Cross-matching with 2MASS/IRAS/Herschel Catalogs

Catalog	Matching Radius	Matched Number
2MASS PSC	— <sup>a</sup>	9410 ( $K_s$ band)
IRAS FSC	$3\sigma_{\text{IRAS}}$ <sup>b</sup>	5812 ( $60 \mu\text{m}$ )
Herschel/PACS PSC	$6''$ ( $160 \mu\text{m}$ ) <sup>c</sup>	219 ( $160 \mu\text{m}$ )
Herschel/SPIRE PSC	$9''$ ( $250 \mu\text{m}$ ) <sup>c</sup>	1096 ( $250 \mu\text{m}$ )

**Notes.**

<sup>a</sup> We adopt the results from the SDSS archive.

<sup>b</sup> Here  $\sigma_{\text{IRAS}}$  is the length of the semimajor axis of the IRAS positional elliptical.

<sup>c</sup> The radius is taken as half of the beam size.

for the remaining 220 sources, which are removed in later analyses.

In order to obtain photometric information covering a wavelength range as wide as possible, we also cross-matched the above catalog with the 2MASS Point Source Catalog (PSC; Skrutskie et al. 2006), IRAS Faint Source Catalog (FSC; Moshir et al. 1990), Herschel/PACS Point Source Catalog (Herschel/PACS PSC<sup>17</sup>), and Herschel/SPIRE Point Source Catalog (Herschel/SPIRE PSC.<sup>18</sup>) The cross-matching conditions and results are summarized in Table 1.

### 2.3. Selection of ULIRGs with Two-band Estimated $L_{\text{IR}}$

Here we summarize a crude method to select ULIRGs from the cross-matched catalog. The total IR luminosity of a galaxy can be crudely estimated with the observed flux densities on the assumption that the galaxy follows an empirically derived SED. In order to estimate the contribution of AGNs to the total IR luminosity, we adopt two SEDs, one for the SB component and the other for the AGN torus component. The SB template is taken from the composite SED of 39 star-forming galaxies at  $z \sim 1$ , which was created by Kirkpatrick et al. (2012) by stacking Spitzer MIR spectroscopy and Herschel FIR photometry. The AGN torus template is taken from the typical quasar SED built by Elvis et al. (1984), which was modified by Xu et al. (2015) by removing the IR contribution of SF from the original SED. Both of the templates are shown in Figure 4. We use the fluxes in the W3 ( $12 \mu\text{m}$ ) and Wide-S ( $90 \mu\text{m}$ ) bands to evaluate the relative contributions of the two templates of the total SED. The IR luminosity of the AGN ( $L_{\text{AGN}}$ ) and SF ( $L_{\text{SF}}$ ) can be estimated by solving the following equation:

$$L_{\text{AGN}} \frac{\int S_{\text{AGN}}(z) T_i d\lambda}{\int T_i c / \lambda^2 d\lambda} + L_{\text{SF}} \frac{\int S_{\text{SF}}(z) T_i d\lambda}{\int T_i c / \lambda^2 d\lambda} = 4\pi D_L^2(z) F_i, \quad (3)$$

where  $i = 12, 90 \mu\text{m}$  indicates the W3 and Wide-S bands,  $S_{\text{AGN}}(z)$  and  $S_{\text{SF}}(z)$  mean the templates that are redshifted to the observed frame and normalized to unit integrated luminosity at 1–1000  $\mu\text{m}$ ,  $T_i$  and  $F_i$  are the transmission curves and fluxes in each band,  $c$  is the speed of light, and  $D_L(z)$  is the luminosity distance. The spectroscopic redshift is employed for the objects with SDSS spectral observations. We adopt the SDSS photometric redshifts for the objects with only imaging data.

<sup>17</sup> <https://doi.org/10.5270/esa-rw7rbo7>

<sup>18</sup> <https://doi.org/10.5270/esa-6gfkpzh>

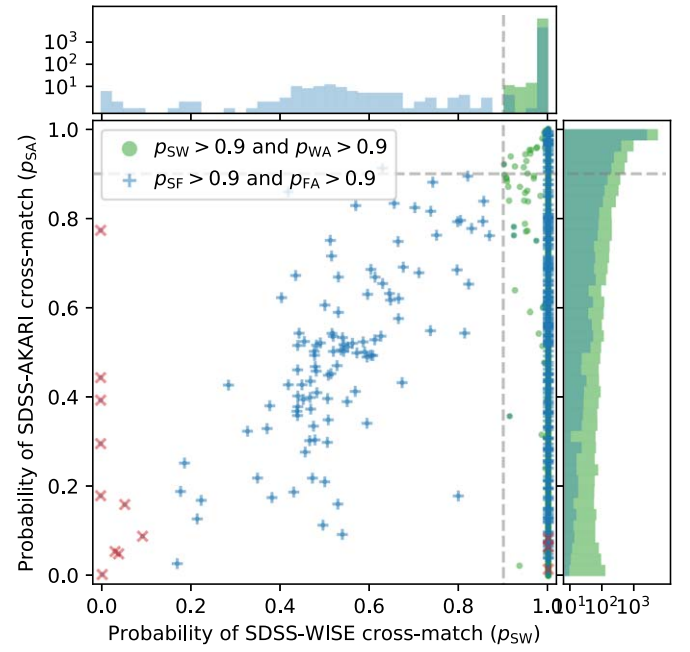


**Figure 3.** Distribution of probabilities of SDSS-WISE matches ( $p_{\text{SW}}$ ) and SDSS-AKARI matches ( $p_{\text{SA}}$ ). The green dots and histogram denote the associations selected with  $p_{\text{SW}} > 0.9$  and  $p_{\text{WA}} > 0.9$ , where  $p_{\text{WA}}$  is the probability of WISE-AKARI matches. The blue plus signs and histogram show the FIRST-identified objects with  $p_{\text{SF}} > 0.9$  and  $p_{\text{FA}} > 0.9$ . The red crosses denote the SDSS objects for which the FIRST detections show different primary sources for AKARI sources from SDSS-WISE-AKARI associations. We adopt the WISE-identified SDSS-AKARI matches in the conflicting cases; see text for details.

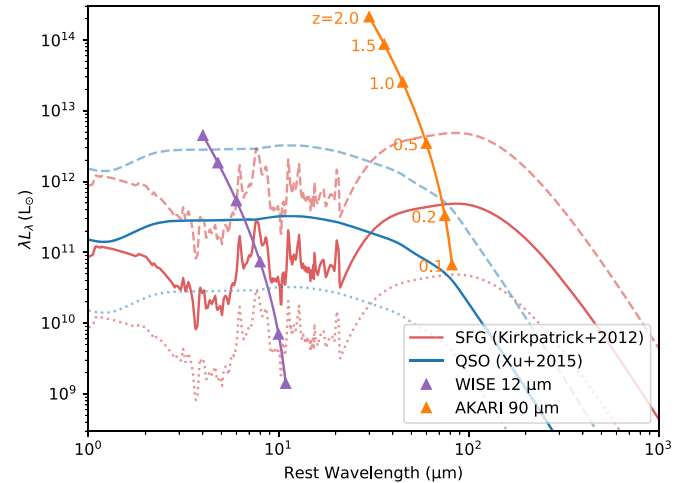


**Figure 4.** The SED templates of quasars (blue; Xu et al. 2015) and SBs (red; Kirkpatrick et al. 2012) used in the two-band IR luminosity estimation. The thick curves denote the SED templates normalized to integrated luminosity at 1–1000  $\mu\text{m}$  of ULIRG level ( $10^{12} L_{\odot}$ ), while the dotted and dashed curves denote the templates normalized to LIRG ( $10^{11} L_{\odot}$ ) and HyLIRG ( $10^{13} L_{\odot}$ ) levels, respectively. The violet and orange triangles show the detection limit of the WISE W3 ( $12 \mu\text{m}$ ) and AKARI Wide-S ( $90 \mu\text{m}$ ) bands at redshifts from 0.1 to 2.0.

The total IR luminosity and the AGN contribution to the total IR luminosity can be calculated as

$$L_{\text{IR}} = L_{\text{AGN}} + L_{\text{SF}}, \quad f_{\text{AGN}} = L_{\text{AGN}}/L_{\text{IR}}, \quad (4)$$

and the results are shown in Figure 5. Within the entire cross-matched catalog, 1077 galaxies are identified as ULIRGs with the threshold  $L_{\text{IR}} \geq 10^{12} L_{\odot}$ . In order to cover the

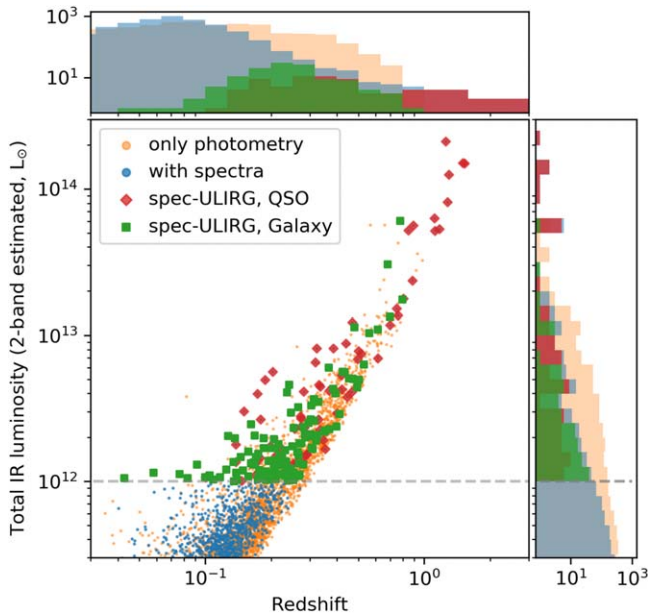


**Figure 5.** Distribution of the redshift ( $x$ -axis) and total IR luminosity ( $y$ -axis) estimated using the two-band estimation method. The objects with SDSS spectroscopy are shown with blue dots, and the objects with only photometric identification are shown with orange dots. The ULIRGs identified as quasars by the SDSS pipeline are shown with red diamonds, while the ULIRGs identified as galaxies are shown with green squares. The gray dashed line denotes the selection threshold of ULIRGs. Note that the two histograms are plotted in a logarithmic grid.

near-IR (NIR) emission of the AGN torus, the luminosity is integrated in the wavelength range of 1–1000  $\mu\text{m}$ , which is extended toward the short-wavelength range compared to the typically adopted wavelength range of 8–1000  $\mu\text{m}$ . Of the 1077 ULIRGs, 195 are spectroscopically identified in SDSS legacy and BOSS surveys with median  $S/N > 2$ . For the eight galaxies with  $2 < S/N < 3$ , we bin the observed spectra by two adjacent pixels in later analyses. All of the observed spectra are corrected for Galactic dust extinction with the Cardelli–Clayton–Mathis (CCM) extinction law (Cardelli et al. 1989) and the dust map updated by Schlafly & Finkbeiner (2011).

The majority of the ULIRGs ( $\sim 90\%$ ) show  $f_{\text{AGN}} \lesssim 0$ , indicating that their IR emission is dominated by SF activity. A negative  $f_{\text{AGN}}$  suggests that the SB template overestimates the MIR luminosity compared to the observed SED, which could be due to the higher fraction of the polycyclic aromatic hydrocarbon (PAH) component of the template or the residual AGN contribution in the SB template (with an average of about 10%; Kirkpatrick et al. 2012). We use the  $f_{\text{AGN}}$  from the two-band estimation with a fixed template for illustrative purposes only. The  $f_{\text{AGN}}$  estimated with a detailed SED analysis will be discussed in Section 4.1.

We construct a 90  $\mu\text{m}$  flux-limited ULIRG sample through the above cross-matching and luminosity estimation. However, the flux limit of the SDSS spectroscopic survey results in incompleteness of the sample of spectroscopically identified ULIRGs. The distribution of the  $i$ -band magnitude and 90  $\mu\text{m}$  flux of the ULIRG sample is shown in Figure 6, in which the blue dashed and dotted lines denote the flux limit of the SDSS legacy spectroscopic ( $i < 17.5$ ) and BOSS galaxy ( $i < 20.0$ ) surveys. The completeness of the optically bright subsample

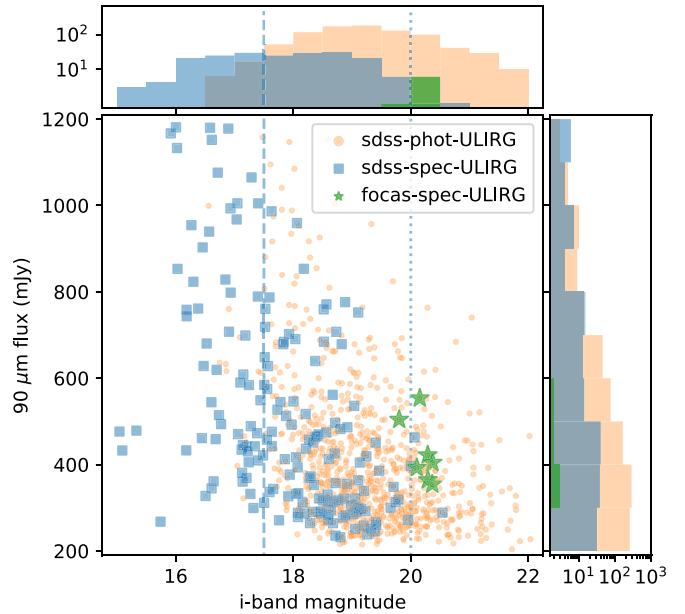


**Figure 6.** Distribution of  $i$ -band magnitude and 90  $\mu\text{m}$  flux of AKARI-selected ULIRGs, where the ULIRGs with SDSS spectroscopy are shown with blue squares and those with only photometric identification are shown with orange dots. The green stars denote the ULIRGs spectroscopically identified by FOCAS. Note that the histograms are plotted with numbers in a logarithmic grid.

( $i < 17.5$ ) is 78% (83/106), while that of the optically faint sample ( $17.5 < i < 20.0$ ) is 12% (112/971).

In order to understand the properties of extremely optically faint ULIRGs at intermediate redshifts ( $0.5 < z < 1$ ), we are conducting an optical follow-up program for AKARI-selected ULIRGs with  $20.0 < i < 21.0$  using FOCAS on the Subaru telescope. Seven objects are observed in a service program in S17A (S17A0216S; PI: Masayuki Akiyama). The details of the data reduction are described in Chen et al. (2019). Finally, we use all of the 202 spectroscopically identified ULIRGs (195 from SDSS and BOSS, seven from the FOCAS observation) as the final sample for later analyses.

### 3. A Self-consistent Spectrum–SED Decomposition Method

In order to determine the properties of the outflowing gas, stellar population, and SF rate (SFR), as well as the AGN luminosity, we develop a method to connect the optical spectral fitting and SED decomposition to obtain a self-consistent result. For simplicity, we briefly introduce the spectral fitting method in Section 3.1, then introduce the SED decomposition and spectrum–SED connection in Section 3.2. A more detailed description of the method can be found in Appendices A and B.

#### 3.1. Optical Spectral Fitting

The optical spectral fitting code is modified from the Quasar Spectral Fitting package (QSFit, v1.3.0; Calderone et al. 2017).<sup>19</sup> It is an IDL program based on MPFIT (Markwardt 2009), which uses the Levenberg–Marquardt (LM) technique to solve the least-squares problem. The original code of QSFit is specialized to the analysis of spectra of quasar-dominated systems, e.g., a power-law continuum with broad Balmer lines. We modified the codes to support the fitting with a HG

<sup>19</sup> <http://qsfit.inaf.it>

component with multiple stellar populations, as well as the automatic separation between quasar and HG spectra under a given threshold. The fitting procedure is also optimized for the detection of outflowing gas emission lines.

The model used to fit the observed spectrum is a collection of several components, which can be classified into three categories: (1) AGN continua, e.g., power-law continuum; (2) HG continua, e.g., stellar continuum; and (3) emission lines, e.g., H $\alpha$  and [O III]. The AGN continua consist of a power-law continuum representing the radiation originating from the accretion disk, a Balmer continuum with blending high-order Balmer emission lines (H11–H50), and a blending iron emission line pseudocontinuum. In order to model the SF history (SFH) of a galaxy in the spectral fitting, we introduce two stellar populations: one is an underlying main stellar (MS) population, and the other represents the ongoing SB population. The stellar library of Bruzual & Charlot (2003) with a Salpeter (1955) initial mass function (IMF) and solar metallicity is adopted in this work. The SFH of the MS and SB components is described with SFR as a function of time:  $\text{SFR}_{\text{MS}}(t) = \text{SFR}_{\text{MS}}(t_0)\exp(-(t - t_0)/\tau_{\text{SF}})$  and  $\text{SFR}_{\text{SB}}(t) = \text{constant}$ , respectively. In the fitting procedure, we account for most of the emission lines that could be covered by the observed spectrum from Ly $\alpha$  to [S III] 9531 Å. The majority of the emission lines are described with a combination of a narrow profile to account for the emission from the H II region and/or AGN narrow-line region (NLR) and a broad profile to represent the outflowing gas and/or the emission line from the AGN broad-line region (BLR). In order to calculate the uncertainties of the best-fit parameters, we use the Monte Carlo resampling method. Thirty mock spectra are generated for each observed spectrum, and similar fitting processes are performed for the mock spectra. Hence, the uncertainty of a given parameter can be estimated from the distribution of the best-fit values of the mock spectra. The details of the fitting procedure are explained in Appendix A.2.

We identify the optical spectra as quasar- or HG-dominated for each ULIRG in the sample. The quasar-dominated spectra are separated from the HG-dominated ones using two indicators of the AGN BLR feature. The first BLR indicator is the sum of the equivalent width (EW) of observed Fe II and Balmer (pseudo)continua, i.e.,  $\text{EW}_{\text{FeII+BAC}} = \text{EW}_{\text{FeII}} + \text{EW}_{\text{BAC}}$ , to the underlying AGN power-law and stellar continua. The second BLR indicator is the 80% width of the line profile for permitted lines, i.e.,  $w_{80,\text{permitted}} = w_{80,\text{H}\beta}$ ,  $z \leq 0.8$  and  $w_{80,\text{MgII}}$ ,  $z > 0.8$ , where the choice of H $\beta$  and Mg II depends on the wavelength coverage. A spectrum is identified as quasar-dominated (e.g., Figure 7, upper panel) if it shows significant Balmer and iron (pseudo)continua, i.e.,  $\text{EW}_{\text{FeII+BAC}} \geq 100$  Å (e.g., Boroson & Green 1992), or significantly broad permitted lines, i.e.,  $w_{80,\text{permitted}} \geq 3000$  km s $^{-1}$ . Since the identification is based on BLR features, we also check the fitting quality with and without a power-law continuum if the spectrum only shows weak BLR features, i.e.,  $\text{EW}_{\text{FeII+BAC}} < 100$  Å and  $w_{80,\text{permitted}} < 3000$  km s $^{-1}$ . If the  $\chi^2$  without a power-law continuum exceeds at least three times the  $\chi^2$  with a power-law continuum, i.e., the spectral fitting fails without a power-law continuum, we classify the spectrum as belonging to a “weak BLR quasar”,<sup>20</sup> otherwise, the spectrum is HG-dominated (e.g., Figure 7, lower panel).

<sup>20</sup> A possible explanation is that the extinction of the BLR is much heavier than the accretion disk. It can also be due to the beaming of the nuclear component, e.g., BL Lac.

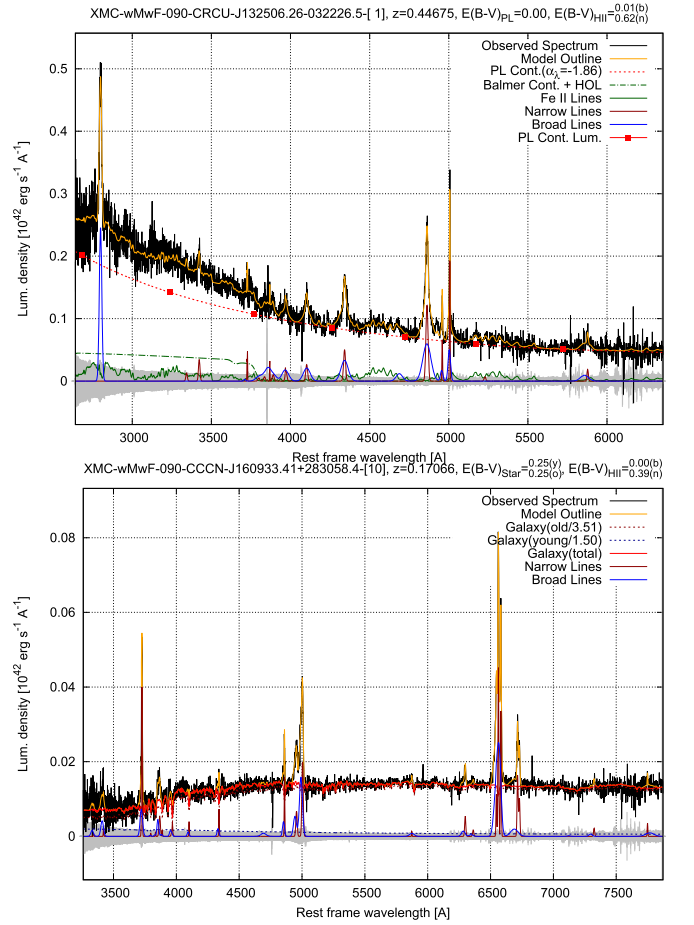


**Figure 7.** Example of a quasar-dominated (J132506.26–032226.5; upper panel) and an HG-dominated (J160933.41+283058.4; lower panel) optical spectrum. The observed spectrum is shown in black, and the measurement error is shown in gray at  $y = 0$ . The power-law continuum is shown by a red dotted line. The green dashed-dotted and solid curves denote the Balmer continuum and iron pseudocontinuum, respectively. The red and blue dotted curves denote the stellar continua of the MS and TSB components, respectively. The red and blue solid curves show the narrow and broad components of the emission lines, respectively.

Finally, 53 of the 202 spectroscopically observed ULIRGs are identified as quasar-dominated, in which two ULIRGs are identified as “weak BLR quasars,” and the remaining 149 ULIRGs are identified as HG-dominated. The identification results and the comparison with SDSS archived spectral classification are shown in Figure 8. Twenty-three ULIRGs that are classified as quasars by the SDSS pipeline are reidentified as HG-dominated by this fitting process. The different SDSS classification for 17 ULIRGs could be due to the misidentification of the broad [O III] emission line with FWHM over 1000 km s $^{-1}$ . Since the broad permitted lines and iron pseudocontinuum usually blend with the surrounding forbidden lines, e.g., [O III] 5007 Å, making it difficult to determine the properties of outflow, and the presence of a power-law continuum also affects the decomposition of stellar components, in later analyses with an SED decomposition, we only focus on the 149 ULIRGs with HG-dominated optical spectra.

### 3.2. Multiband SED Decomposition with Optical Spectral Fitting Results

Several fitting procedures have been developed in order to model the multiband SEDs of galaxies, e.g., MAGPHYS

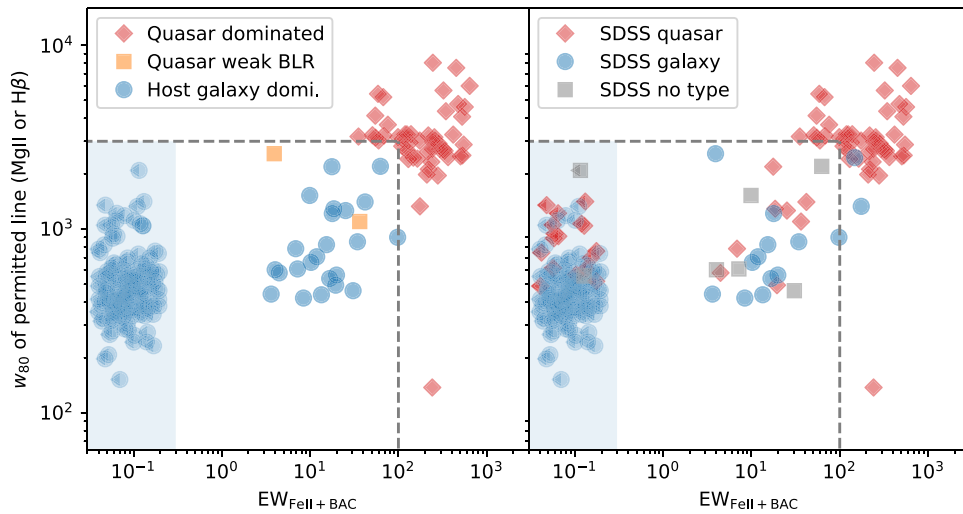


**Figure 8.** Spectral identification for AKARI-selected ULIRGs. The left panel shows the checking results according to the features of the AGN BLR, in which the  $x$ -axis denotes the sum of the EW of the observed Fe II and Balmer (pseudo)continua, i.e.,  $EW_{\text{FeII}+\text{BAC}} = EW_{\text{FeII}} + EW_{\text{BAC}}$ , to the underlying AGN power-law and stellar continua, and the  $y$ -axis denotes the 80% width of the permitted lines, i.e.,  $w_{80,\text{permitted}} = w_{80,\text{H}\beta}$ ,  $z \leq 0.8$  and  $w_{80,\text{MgII}}$ ,  $z > 0.8$ , where the choice of H $\beta$  and Mg II depends on the wavelength coverage. A spectrum is identified as quasar-dominated (red diamonds) if it shows  $EW_{\text{FeII}+\text{BAC}} \geq 100 \text{ \AA}$  or  $w_{80,\text{permitted}} \geq 3000 \text{ km s}^{-1}$ . Orange squares denote two spectra with weak BLR features; however, a power-law continuum is required to obtain a good spectral fitting. The pure galaxies are shown with blue circles. Note that for galaxies in the blue shaded region, no Fe II or Balmer (pseudo)continua are required in the fitting, i.e.,  $EW_{\text{FeII}+\text{BAC}} = 0$ . A random shift in the  $x$ -axis is added for such galaxies for the purpose of illustration. The right panel shows the identifications from the SDSS archive with the same axes as in the left panel.

(da Cunha et al. 2008) and CIGALE (Noll et al. 2009; Boquien et al. 2019). These codes usually invoke a huge (e.g.,  $\sim 10^5$ ) library of stellar SEDs to fit the UV–optical radiation of stars and obtain physical information such as stellar mass and SFR. In order to take advantage of the results from the spectral fitting discussed above, e.g., stellar continuum decomposition and extinction, in this work, we develop a new SED fitting code to obtain a self-consistent result between spectral and SED fitting analyses.

A widely adopted strategy of multiband SED decomposition is the so-called “energy balance,” which requires conservation between the attenuated primary radiation from stars and/or AGNs and the reemitted emission by the dust surrounding the primary emitters. We first consider the dust absorption and reemission in HGs. The real conditions and properties of dust in the galaxies can be very complicated (e.g., Galliano et al. 2008, 2018). In the fitting procedure, we employ a two-component model following the assumption in the optical spectral fitting, i.e., an old MS component with exponential SFH and an ongoing SB component with constant SFR. The optically observed SB components represent the young stars for which the birth clouds (BC) have been destroyed and migrated to the diffuse interstellar medium (ISM) dust. For simplicity, hereafter, we refer to the young stellar population embedded in optically thin diffuse ISM as the “transparent SB” (TSB) component, which corresponds to the young stellar population in the optical spectra, and the young stars that are almost fully absorbed by optically thick natal clouds in the optical band as the “attenuated SB” (ASB). We assume the ASB component has the same stellar population as the TSB component, which can be estimated from optical spectral fitting. The TSB component is assumed to be embedded in diffuse ISM dust with the same extinction for the MS component. Extinction of  $A_V = 100$  is assumed for the ASB component for all galaxies, which corresponds to a typical dense collapsing cloud with a spatial scale of 0.2 pc,  $n_{\text{H}_2} = 2 \times 10^5 \text{ cm}^{-3}$ , and a V-band opacity of  $3 \times 10^3 \text{ m}^2 \text{ Kg}^{-1}$  (Shu et al. 1987).

Here we employ the dust emission SED using The Heterogeneous Evolution Model for Interstellar Solids (THEMIS<sup>21</sup>) dust model (Jones et al. 2013; Köhler et al. 2014) updated by Nersesian et al. (2019). The diffuse ISM dust heated by the MS and TSB components is considered to be exposed in ambient starlight with a constant intensity, while the dust surrounding the young stars (ASB) is exposed in a power law–distributed starlight intensity, i.e.,  $dM/dU \propto U^{-\alpha}$  (e.g., Dale & Helou 2002; Draine & Li 2007; Dale et al. 2014).

In addition to the dust surrounding stars, the AGN can also contribute to the IR SED of the galaxy by the thermal emission from a thick layer of dust surrounding an accretion disk. The UV–optical radiation from the accretion disk is absorbed by the torus and then reemitted as torus thermal radiation. In this work, we employ the SKIRTor<sup>22</sup> torus model developed by Stalevski et al. (2012) and updated in Stalevski et al. (2016) using the 3D Monte Carlo radiative transfer code SKIRT (Baes et al. 2003, 2011). The SKIRTor model consists of a two-phase medium, i.e., a large number of high-density clumps embedded in a smooth dusty component of low-density grains. As explained in Section 3.1, only torus emission models of type 2 AGNs (for which the optical spectrum is dominated by a galaxy component) are used in the proceeding analyses. The observed flux of the torus emission ( $F_{\text{torus}}$ ) can be estimated from the IR SED decomposition. Then, the intrinsic luminosity of the AGN primary source ( $L_{\text{AGN}}$ ), i.e., the accretion disk, can be estimated from  $F_{\text{torus}}$  within the framework of the SKIRTor torus model using the energy conservation equation (see Equation (B2) in Appendix B.3). The most important parameter in the conversion from  $F_{\text{torus}}$  to  $L_{\text{AGN}}$  is the half-opening angle  $\Theta$  (or the covering factor of the torus). Since the torus is usually considered to be optically thick, the half-opening angle  $\Theta$  determines the fraction of the primary radiation of the AGN, which is absorbed and reemitted by the dusty torus. Recently,

<sup>21</sup> [https://www.ias.u-psud.fr/themis/THEMIS\\_model.html](https://www.ias.u-psud.fr/themis/THEMIS_model.html)

<sup>22</sup> <https://sites.google.com/site/skirtor/>

the study of X-ray-selected AGNs reported that the typical covering factor is about 0.6 (Stalevski et al. 2016; Mateos et al. 2017; Ichikawa et al. 2019), which corresponds to  $\Theta \sim 30^\circ$ . Since  $\Theta$  highly affects the estimation of  $L_{\text{AGN}}$ , and it is hard to determine with only a limited number of IR photometric data points, it is a proper choice to fix it to the typical value from the literature. The fitting with the fixed  $\Theta = 30^\circ$  results in an average absorption ratio of AGN primary radiation, i.e.,  $L_{\text{torus}}/L_{\text{AGN}}$ , of 0.22.

We consider the energy conservation in each emitter-absorber system, including all of the primary radiation components, i.e., MS, TSB, ASB, and AGN (accretion disk), as well as the dust reemitted components, i.e., ISM dust heated by MS and TSB, BC heated by ASB, and torus heated by AGN (see Equations (B1) and (B2) in Appendix B.3 for details). Note that in the integration of absorbed luminosity by dust, we set a lower limit of wavelength 912 Å, with an underlying assumption that most of the photons with energy higher than 13.6 eV are absorbed by the photoionization process of hydrogen and helium gas in the H II region, rather than attenuated by the dust (Draine & Li 2007).

In order to connect the spectral fitting results to the SED fitting process, we adopt the best-fit stellar continua and dust extinction as the input of SED fitting to constrain the stellar population. Two additional parameters, i.e.,  $C_{\text{ape,MS}}$  and  $C_{\text{ape,TSB}}$ , are employed to correct for the aperture loss of optical spectroscopy for extended MS and TSB components, respectively. The best-fit emission line profiles from spectral fitting are also used to represent their contribution to the broadband photometry. The average of  $C_{\text{ape,MS}}$  and  $C_{\text{ape,TSB}}$  is used to correct for the aperture loss of narrow lines from the H II region and AGN NLR and broad lines from outflowing gas. No aperture correction is considered for AGN continuum components and BLR emission lines.

Following the fitting strategy of CIGALE, we add an additional error (10% of the flux) to each photometric point to take into account uncertainties in the models in the minimization of  $\chi^2$ . Figure 9 shows one example of the best-fit SED model. In order to calculate the uncertainties of the best-fit parameters, we use the Monte Carlo resampling method. For each ULIRG, 100 mock photometric observations are generated by adding the random noise to the observed fluxes in each band. The random noise is Gaussian-distributed with the amplitude from the measurement error in each band. The same fitting processes are employed for the mock photometric data, and the scatters of the best-fit values are taken as the uncertainties of the parameters.

#### 4. Properties of the AKARI-selected ULIRGs from Spectrum–SED Decomposition

The total IR (1–1000  $\mu\text{m}$ ) luminosity, i.e.,  $L_{1-1000}$ , can be estimated with the best-fit SED models. Of the 149 galaxies with galaxy-dominated optical spectra (Section 3.1), 125 show  $L_{1-1000} \geq 10^{12} L_\odot$ , indicating that the two-band ULIRG selection method presented in Section 2.3 is effective to select ULIRGs.<sup>23</sup> The remaining 24 galaxies are luminous LIRGs with a median integrated luminosity of  $L_{1-1000} = 10^{11.9 \pm 0.1} L_\odot$ . We keep all of the 149 galaxies in later discussions.

<sup>23</sup> If we use the luminosity integrated in the 8–1000  $\mu\text{m}$  range, i.e.,  $L_{8-1000}$ , the number of selected ULIRGs is 111.

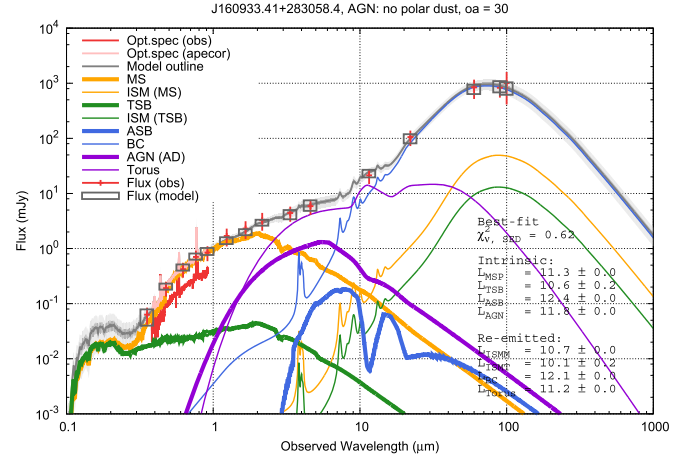


**Figure 9.** Best-fit SED decomposition for a ULIRG, J160933.41+283058.4. The red and pink curves denote the observed (Figure 7, lower panel) and aperture-corrected optical spectra, respectively. The observed fluxes in each band are shown with red plus signs with the error bar showing the  $3\sigma$  measurement errors, while the best-fit flux values are marked using gray open squares. The outline of the best-fit SED is shown with a gray curve, while the SEDs of the extinct primary radiation (i.e., MS, TSB, ASB, and AGN (accretion disk)) and dust reemitted emission (i.e., ISM, BC, and, torus) are shown by thick and thin colored curves, respectively. The same color is used for the primary source and the related dust component.

The bolometric luminosity of the entire galaxy can be defined as

$$\begin{aligned} L_{\text{Bol,Gal}} &= L_{\text{star}} + L_{\text{AGN}}, \\ &= C_{\text{ape,MS}} L_{\text{MS}}^{\text{SP}} + C_{\text{ape,TSB}} L_{\text{TSB}}^{\text{SP}} + L_{\text{ASB}} + L_{\text{AGN}}, \end{aligned} \quad (5)$$

where  $L_{\text{star}}$  is the total stellar bolometric luminosity;  $C_{\text{ape,MS}} L_{\text{MS}}^{\text{SP}}$  and  $C_{\text{ape,TSB}} L_{\text{TSB}}^{\text{SP}}$  are the aperture-corrected luminosity of stars in the MS and TSB components;  $L_{\text{ASB}}$  shows the radiation of ASB, i.e., the SBs hidden in the optical band, estimated from the FIR dust emission after reducing the contribution of the MS and TSB components; and  $L_{\text{AGN}}$  denotes the bolometric luminosity of the AGN, which is estimated from the best-fit torus SED (see Appendix B.3 for details). Here  $L_{\text{Bol,Gal}}$  describes the sum of the primary (intrinsic) UV–optical–NIR radiation from stars in the HG and the accretion disk of the AGN. The average  $L_{\text{Bol,Gal}}$  of the 149 selected galaxies is  $10^{12.6 \pm 0.3} L_\odot$ . We report the estimation of AGN luminosities in Section 4.1 and the properties of the HGs, e.g., stellar mass and SFR, in Section 4.2. The outflow detection is reported in Section 4.3.

##### 4.1. AGN Activities in the AKARI-selected ULIRGs

With the bolometric luminosity of AGN primary emission ( $L_{\text{AGN}}$ ) and the total bolometric luminosity of the galaxy ( $L_{\text{Bol,Gal}}$ ), we can define the AGN bolometric energy contribution as  $f_{\text{AGN}} = L_{\text{AGN}}/L_{\text{Bol,Gal}}$ . The distributions of  $f_{\text{AGN}}$  and  $L_{\text{Bol,Gal}}$  are shown in Figure 10. In order to check the reliability of the detection of AGNs in the galaxies, we evaluate the detection ratio of the MIR excess at rest 3–10  $\mu\text{m}$  (W1–W2 bands for galaxies at  $z \sim 0$  and W2–W3 bands for galaxies at  $z \sim 1$ ), which is the most significant feature of AGNs in the IR SED fitting. The detection ratio in one band, e.g., W1, can be calculated as  $\beta_{\text{AGN,W1}} = F_{\text{AGN,W1}}/\sigma_{\text{W1}}$ , where  $F_{\text{AGN,W1}}$  is the flux contributed from the AGN component, and  $\sigma_{\text{W1}} = \sigma_{\text{obs,W1}} + 10\%F_{\text{obs,W1}}$ , where  $F_{\text{obs,W1}}$  and  $\sigma_{\text{obs,W1}}$  are the

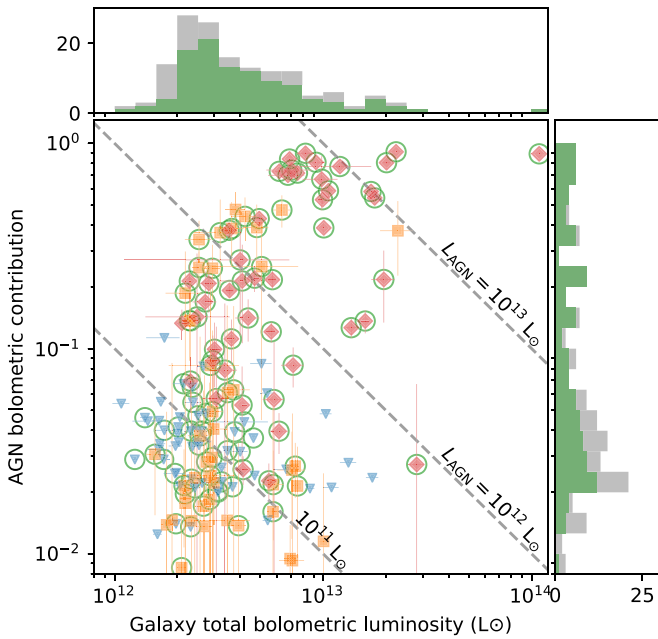


**Figure 10.** The AGN bolometric contribution ( $f_{\text{AGN}} = L_{\text{AGN}}/L_{\text{Bol, Gal}}$ ; y-axis) as a function of the total bolometric luminosities of the galaxy ( $L_{\text{Bol, Gal}}$ ; x-axis) of the AKARI-selected ULIRGs. The red diamonds denote the galaxies (47/149) with an AGN component detection ratio  $\beta_{\text{AGN}} > 3$  in the W1–W3 bands in the SED fitting. The orange squares denote the galaxies (46/149) with  $1 < \beta_{\text{AGN}} < 3$  in the W1–W3 bands. The blue triangles show the galaxies (56/149) with  $\beta_{\text{AGN}} < 1$ , for which we estimate the upper limit of  $f_{\text{AGN}}$  by scaling the mean AGN SED from the 47 galaxies with  $\beta_{\text{AGN}} > 3$  (see Section 4.1 for a detailed discussion). The gray histograms show the distributions for all 149 galaxies. The green circled markers and green histograms denote that they are selected using the 90% confidence criterion of the Assef et al. (2018) method. The gray dashed lines denote the positions of AGN bolometric luminosities of  $10^{11}$ ,  $10^{12}$ , and  $10^{13} L_{\odot}$ .

observed flux and measurement error in the W1 band. In order to take into account the uncertainty in the fitting model, 10% of the observed flux is included in the estimation of the total uncertainty in the W1 band. (see Section 3.2).

We consider the AGN component significantly detected if the galaxy shows  $\beta_{\text{AGN, MIR}} > 3$  in any one band among the W1, W2, and W3 bands. Among the 149 ULIRGs, 47 galaxies are selected with the threshold (red diamonds in Figure 10), which show a median  $f_{\text{AGN}}$  of 20% with S/N (i.e.,  $f_{\text{AGN}}/\sigma_{f_{\text{AGN}}}$ ) of 7. In the remaining 102 ULIRGs, 46 galaxies show  $\beta_{\text{AGN, MIR}} > 1$  in one band among W1–W3, for which the AGN is less significantly detected with a median  $f_{\text{AGN}}$  of 3% and S/N of 2 (orange squares in Figure 10). The remaining 56 galaxies show  $\beta_{\text{AGN, MIR}} < 1$  in all bands among W1–W3, which means the AGN component is not detected in those galaxies (blue triangles in Figure 10). In order to estimate the upper limits of  $f_{\text{AGN}}$  and  $L_{\text{AGN}}$  for the 56 galaxies, we first estimate the averaged AGN SED from the best-fit results of the 47 galaxies with  $\beta_{\text{AGN, MIR}} > 3$ , which are logarithmically averaged after normalization by AGN bolometric luminosity. The averaged AGN SED is then scaled until it exceeds  $1\sigma$  uncertainty, as shown above, in any bands among W1–W3 for a galaxy, and the  $f_{\text{AGN}}$  and  $L_{\text{AGN}}$  corresponding to the scaled AGN SED are employed as the upper limits for the galaxy.

We compare our AGN detection method with the AGN selection criteria with 90% reliability of Assef et al. (2018, hereafter A18), which also trace the AGN MIR excess but using the W1–W2 color. For the ULIRGs with significant AGN MIR excess, i.e.,  $\beta_{\text{AGN, MIR}} > 3$ , the two methods match well,

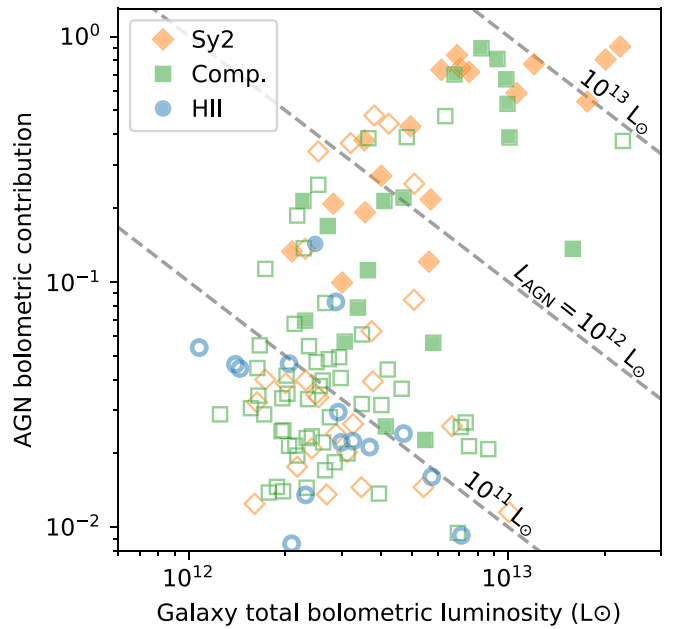


**Figure 11.** The AGN bolometric contribution ( $f_{\text{AGN}}$ ) as a function of the total bolometric luminosities of the galaxy ( $L_{\text{Bol, Gal}}$ ) of 131 AKARI-selected ULIRGs with BPT diagram classifications. The Seyfert 2 (orange diamonds), composite (green squares), and star-forming (H II; blue circles) galaxies are separated using the flux ratios of the narrow components of emission lines by the Kewley et al. (2001) and Kauffmann et al. (2003) curves. Filled symbols show the galaxies with significantly detected AGNs in the MIR bands ( $\beta_{\text{AGN, MIR}} > 3$  in Figure 10). Open symbols denote the galaxies with less significantly detected AGNs ( $1 < \beta_{\text{AGN, MIR}} < 3$ ) and only upper limits of AGN luminosities ( $\beta_{\text{AGN, MIR}} < 1$ ). The gray dashed lines denote the positions of AGN bolometric luminosities of  $10^{11}$ ,  $10^{12}$ , and  $10^{13} L_{\odot}$ .

and 46 of the 47 ULIRGs are selected with the A18 criteria. The matching ratios of A18 selection are 67% (31/46) and 48% (27/56) for the galaxies with  $1 < \beta_{\text{AGN, MIR}} < 3$  and  $\beta_{\text{AGN, MIR}} < 1$ , respectively, for which the blue W1–W2 color can be mainly contributed by the radiation of a stellar direct component or the bright PAH  $3.3 \mu\text{m}$  emission line in the SED decomposition here (e.g., Mateos et al. 2012; Ichikawa et al. 2017).

Another widely adopted method to identify AGNs (Seyfert 2 galaxies) is classification with the Baldwin–Phillips–Terlevich (BPT) diagram (Baldwin et al. 1981). Of the 149 galaxies, 131 have spectra that cover the wavelength range of the [O III], H $\beta$ , H $\alpha$ , and [N II] lines. We require that for each line, the fraction of bad pixels (e.g., contaminated by bright night sky lines) should be smaller than 25% from the 10th to 90th percentiles of the narrow-line profile. The classification is performed using the narrow lines, and the numbers of Seyfert 2, composite, and star-forming (H II) galaxies are 44, 72, and 15, respectively (Figure 11). The mean  $f_{\text{AGN}}$  values of the H II, composite, and Seyfert 2 galaxies are 4%, 13%, and 26%, respectively, suggesting a trend that as the AGN becomes luminous, it begins to dominate the ionization of the gas. The majority of the H II ULIRGs (14/15) show  $f_{\text{AGN}} < 10\%$ ; however, the Seyfert 2 galaxies cover a wide range from SF-dominated ( $f_{\text{AGN}} \sim 5\%$ ) to AGN-dominated ( $f_{\text{AGN}} \sim 50\%$ ) cases. One explanation for the SF-dominated ULIRGs but with Seyfert 2–like ionization could be that the H II regions ionized by stellar light are more dusty than the AGN NLR. Since the ionization in H II regions is dominated by young O/B-type stars, the line emission from the ionized gas could be severely

obscured by the dense dust surrounding the young stars (e.g., compact H II region; Stéphan et al. 2018). Therefore, although the SF activity could dominate the bolometric luminosity of the galaxy (e.g., low  $f_{\text{AGN}}$ ), it may only show a small contribution to the gas ionization observed in the optical band.

Finally, we show the relationship between  $L_{\text{AGN}}$  and the luminosity of the [O III] 5007 Å emission line. With a relatively high ionization potential (IP; 35.12 eV), the intensity of the [O III] line is usually considered to reflect the AGN activity (e.g., Kauffmann et al. 2003). The dust extinction is estimated with a Balmer decrement or extinction of stellar continuum when the Balmer lines are too weak (see Table A5 in Appendix A). We use the average of  $C_{\text{ape,MS}}$  and  $C_{\text{ape,TSB}}$  to correct for the aperture loss of the [O III] line. Note that if the [O III] line originates from a compact NLR (e.g.,  $< \sim 0.1$  kpc), there is no need to correct the [O III] line for aperture loss; thus, the corrected  $L_{[\text{OIII}]}$  could be considered as some upper limit in such a case. The results for 136 galaxies with high-quality detections of the [O III] line (measurement S/N over 5 and a fraction of bad pixels smaller than 25% from the 10th to 90th percentiles of the entire [O III] line profile) are shown in Figure 12. In order to determine the underlying functional relationship between  $L_{[\text{OIII}]}$  and  $L_{\text{AGN}}$ , which are considered as two independent variables, we employ an ordinary least-squares bisector fit after normalizing with the value ranges in both the  $x$ - and  $y$ -axes in a logarithmic grid (Isobe et al. 1990). The Schmitt binning method (Schmitt 1985) in the ASURV software<sup>24</sup> (Feigelson & Nelson 1985; Isobe et al. 1986; Lavalley et al. 1992) is used to account for the estimated upper limit of  $L_{\text{AGN}}$  for the ULIRGs with barely any AGN detection (i.e.,  $\beta_{\text{AGN,MIR}} < 1$ ).

The Spearman correlation coefficient ( $r_s$ ) and the  $p$ -value of the hypothesis testing are applied to describe the correlation between  $L_{[\text{OIII}]}$  and  $L_{\text{AGN}}$ . We obtain<sup>25</sup>

$$\log L_{[\text{OIII}]} = 0.68 (\pm 0.06) \log L_{\text{AGN}} + 34.90 (\pm 0.63), \quad (6)$$

with  $r_s = 0.41$  and a  $p$ -value of  $7 \times 10^{-7}$ . If only the 46 ULIRGs with significantly detected AGNs ( $\beta_{\text{AGN,MIR}} > 3$ ) are considered, the regression function is<sup>26</sup>

$$\log L_{[\text{OIII}]} = 0.74 (\pm 0.07) \log L_{\text{AGN}} + 33.78 (\pm 0.89), \quad (7)$$

with  $r_s = 0.49$  and a  $p$ -value of  $6 \times 10^{-4}$ . The coefficients indicate a correlation between estimated  $L_{[\text{OIII}]}$  and  $L_{\text{AGN}}$ , suggesting the consistency of the determination of the AGN's activity from the [O III] emission line and the IR SED decomposition.

The slope of the fitting function does not change between the entire sample and the sources with only significantly detected AGNs. We also compare the derived  $L_{[\text{OIII}]}-L_{\text{AGN}}$  regression functions to the empirical correlations for type 2 AGNs in the literature (Marconi et al. 2004; Berney et al. 2015; Ueda et al. 2015). The ULIRG sample shows a shallower  $L_{[\text{OIII}]}-L_{\text{AGN}}$  slope than that of typical type 2 AGNs (e.g., 0.7 versus 1.1; see

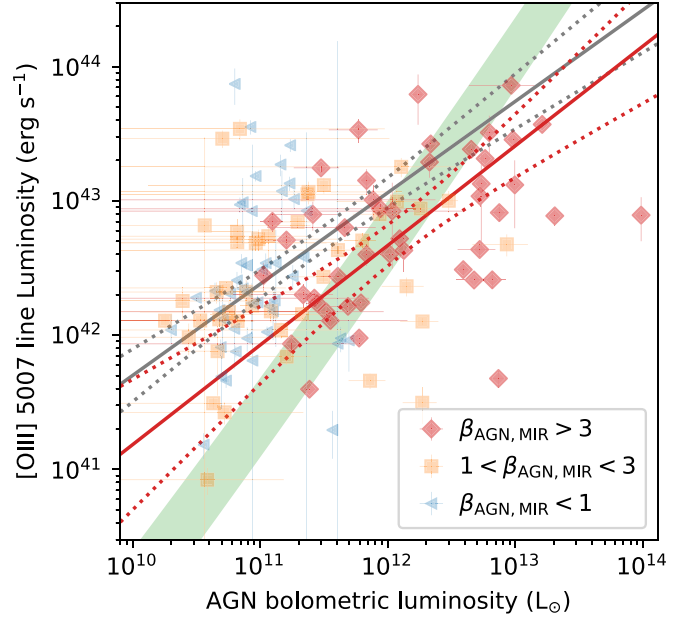


**Figure 12.** Corrected [O III] luminosity vs. AGN bolometric luminosity for 136 galaxies with [O III] line detection. The red, orange, and blue symbols correspond to the detection ratios of AGN MIR excess (see Section 4.1 and Figure 10). Note that for the galaxies with no AGN detection ( $\beta_{\text{AGN,MIR}} < 1$ ), the upper limit of  $L_{\text{AGN}}$  is used for plotting. The gray solid line is the ordinary least-squares bisector fitting function for the entire sample, and the red solid line is for the sources with significantly detected AGNs (red diamonds). The Schmitt (1985) binning method is used to account for the upper limit of  $L_{\text{AGN}}$  for the ULIRGs with no AGN detection in the fitting for the entire sample. The dotted lines denote the 95% confidence bands of the fitting lines. The green shaded region denotes the empirical  $L_{[\text{OIII}]}-L_{\text{AGN}}$  functions for type 2 AGNs using the  $L_{[\text{OIII}]}-L_{2-10\text{keV}}$  functions of Berney et al. (2015) and Ueda et al. (2015) and the X-ray bolometric corrector of Marconi et al. (2004).

Figure 12), which could be due to the higher contamination of [O III] emission from star-forming regions in the ULIRGs, especially with low AGN bolometric luminosity.

#### 4.2. Stellar Mass and SFR

The stellar decomposition in the optical spectral fitting results in the best-fit stellar population templates, which provide the mass-to-luminosity ratio of stars and the luminosity of the MS and TSB components; thus, the stellar masses  $M_{\text{MS}}^{\text{sp}}$  and  $M_{\text{TSB}}^{\text{sp}}$  can be estimated. However,  $M_{\text{MS}}^{\text{sp}}$  and  $M_{\text{TSB}}^{\text{sp}}$  only denote the masses of components within the 3'' fibers of SDSS spectroscopy observations (2'' for BOSS spectroscopy), not the masses of the whole galaxies, which should be corrected to the SDSS photometric fluxes of the entire galaxies. The aperture correction factors  $C_{\text{ape,MS}}$  and  $C_{\text{ape,TSB}}$  can be estimated in the SED fitting process, and the best-fit results show averages of  $C_{\text{ape,MS}} = 1.9 \pm 0.6$  and  $C_{\text{ape,TSB}} = 2.0 \pm 1.8$  for the entire sample. The mass of stars in the ASB component can be estimated from the reproduced intrinsic bolometric luminosity ( $L_{\text{ASB}}$ ) with the assumption that the ASB has the same stellar population (and the same mass-to-luminosity ratio) as the TSB components, i.e.,  $M_{\text{ASB}} = L_{\text{ASB}} (M_{\text{TSB}}^{\text{sp}} / L_{\text{TSB}}^{\text{sp}})$ . Therefore, the total stellar mass of the galaxy can be described as

$$M_{\text{star,tot}} = C_{\text{ape,MS}} M_{\text{MS}}^{\text{sp}} + \left( C_{\text{ape,TSB}} + \frac{L_{\text{ASB}}}{L_{\text{TSB}}^{\text{sp}}} \right) M_{\text{TSB}}^{\text{sp}}. \quad (8)$$

<sup>24</sup> A Python package in <http://python-asurv.sourceforge.net>.

<sup>25</sup> Note that the Schmitt binning method requires an arbitrary choice of the number of bins. The results shown in Equation (6) are derived using 10 bins in both the  $x$ - and  $y$ -axes. We also employ the regression method with a binning size from 8 to 20, and the derived fitting slope slightly changes from 0.64 to 0.70. We adopt the regression results with a binning size of 10 throughout the paper.

<sup>26</sup> We employ the original bisector linear regression instead of the Schmitt binning method for the ULIRGs with significantly detected AGNs.

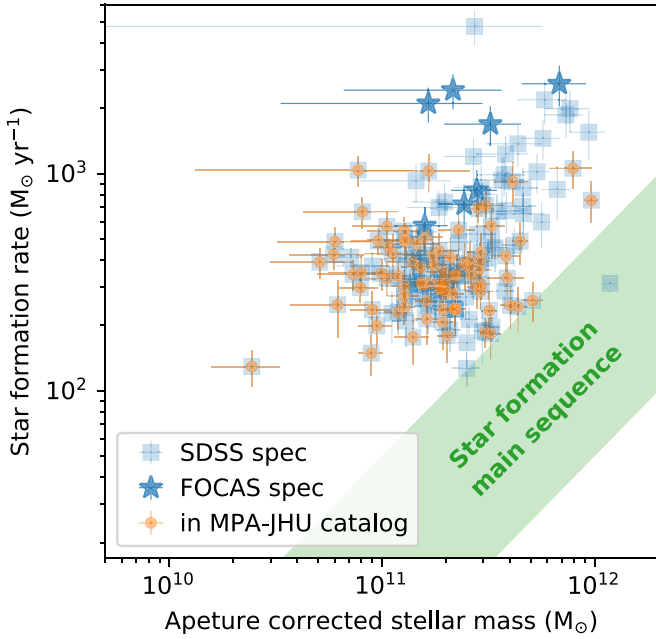


**Figure 13.** The SFR vs. total stellar mass ( $M_{\text{star}}$ ) for AKARI-selected ULIRGs. The SFR is estimated using the SFH from spectral fitting results and modified with SED decomposition (Equation (9)). The  $M_{\text{star}}$  denotes the total mass of old and young stellar populations, which is estimated using the SFH from spectral fitting results and corrected for aperture loss with SDSS photometry (Equation (8)). The blue squares and stars denote the galaxies spectroscopically identified by SDSS and FOCAS, respectively, while orange dots mark the galaxies that are reported in the sample of the MPA-JHU group. The green shaded region denotes the star-forming main sequence at  $z = 0-0.5$  (Peng & Maiolino 2014).

The total current SFR can be similarly described as the sum of the SFRs of the three stellar components,

$$\begin{aligned} \text{SFR}_{\text{star,tot}} &= \text{SFR}_{\text{MS}} + \text{SFR}_{\text{TSB}} + \text{SFR}_{\text{ASB}} \\ &= C_{\text{ape,MS}} \text{SFR}_{\text{MS}}^{\text{sp}} + \left( C_{\text{ape,TSB}} + \frac{L_{\text{ASB}}}{L_{\text{TSB}}^{\text{sp}}} \right) \text{SFR}_{\text{TSB}}^{\text{sp}}, \end{aligned} \quad (9)$$

where  $\text{SFR}_{\text{MS}}^{\text{sp}}$  and  $\text{SFR}_{\text{TSB}}^{\text{sp}}$  mean the simultaneous SFRs of the MS and TSB components estimated from the optical spectral fitting with an assumed exponential SFH.

Figure 13 shows the SFR– $M_{\text{star}}$  diagram for the AKARI-selected ULIRGs. The results indicate a population of massive galaxies with an average  $M_{\text{star}} = 4.1(\pm 1.3) \times 10^{11} M_{\odot}$ , which locates above the SF main sequence ( $z = 0-0.5$ ; Peng & Maiolino 2014), with an average SFR =  $390(\pm 290) M_{\odot} \text{ yr}^{-1}$ . Twelve ULIRGs have SFR  $> 1000 M_{\odot} \text{ yr}^{-1}$ , in which J115458.02+111428.8 ( $z = 0.798$ ,  $L_{1-1000} = 1.28 \times 10^{13} L_{\odot}$ ) shows the largest SFR close to  $5000 M_{\odot} \text{ yr}^{-1}$ .

Seventy galaxies in the total sample are covered by the galaxy catalog of the MPA-JHU group<sup>27</sup> (shown with orange dots in Figure 13). We compare the estimation of  $M_{\text{star}}$  for the 70 galaxies. The  $M_{\text{star}}$  in the MPA-JHU catalog was estimated using SDSS photometry after correcting for the contribution of emission lines using the optical spectra. Our results show consistency with the MPA-JHU group with an average factor of about 1.7. The discrepancy could be due to the different IMF used in the analysis. Compared to the IMF of Kroupa (2001)

used by the MPA-JHU group, the IMF of Salpeter (1955) employed in this work contains a larger number of low-mass stars and could yield a larger mass-to-luminosity ratio (e.g., Cappellari 2012), which leads to a higher estimate of stellar mass. Akiyama et al. (2008) found that for a typical SED with a rest UV color of 1.0, the ratio of estimated stellar masses using the IMFs of Salpeter (1955) and Kroupa (2001) is 1.8, which is fully consistent with the observed offset in this work.

However, the SFR of the 70 galaxies estimated in this work is 10–100 times higher than the results reported by MPA-JHU, which are estimated using optical emission line luminosity (Brinchmann et al. 2004) and optical galaxy photometry (Salim et al. 2007). The large difference is due to the heavy dust obscuration of SF regions in ULIRGs; thus, the SFR based only on optical detection can be significantly underestimated. In order to check the reliability of the SFR from the SED modeling, which considers a fully obscured SB to explain the observed FIR flux, we also compare with the results directly estimated from the integrated IR luminosity  $L_{8-1000}$ , which is estimated from the best-fit SED model, and the empirical relationship determined by Kennicutt (1998),

$$\text{SFR} (M_{\odot} \text{ yr}^{-1}) = 4.5 \times 10^{-44} L_{8-1000} (\text{erg s}^{-1}), \quad (10)$$

which is obtained with an assumption of continuous SBs of age 10–100 Myr with the IMF of Salpeter (1955). The SFR in this work is consistent with that from the Kennicutt (1998) relation with a factor of 1.8. The higher estimated values from the SED fitting could be due to the fact that we ignore the higher-energy photons ( $> 13.6 \text{ eV}$ ) in the dust extinction, which requires more young stars (higher SFR) to explain the FIR dust emission in the energy conservation equations (Equation (B1) in Appendix B.3).

#### 4.3. Outflow Velocity of Ionized Gas

The [O III] 5007 Å emission line kinematics is widely used as an indicator of the outflowing ionized gas (example shown in Figure 14). In order to describe the multicomponent profiles, following Zakamska & Greene (2014) and Perna et al. (2015), we employ the velocity defined from the normalized cumulative distribution,

$$F = \frac{\int_{-\infty}^{\nu_F} f(\nu') d\nu'}{\int_{-\infty}^{\infty} f(\nu') d\nu'}, \quad (11)$$

where  $f(\nu)$  is the flux per velocity unit from the best-fit spectrum,  $F$  equals the fraction of flux with velocity  $\nu \leq \nu_F$ , and  $|\nu_{50}|$  is the 50% flux velocity of the total [O III] line profile (narrow + broad components), which denotes the median velocity shift. The width comprising 80% of the total flux, i.e.,  $w_{80} \equiv \nu_{90} - \nu_{10}$ , is adopted to denote the width of the entire line profile, which is equivalent to 2.563 times the standard deviation for a single Gaussian profile. Figure 15 shows the measured velocity shifts ( $\nu_{50}$ ) and widths ( $w_{80}$ ) of the [O III] lines for 136 ULIRGs with S/N  $> 5$  for the observed [O III] flux. The measured  $w_{80}$  is correlated with  $\nu_{50}$ , indicating that the outflowing gas with a faster velocity shift tends to be more turbulent.

Of the 136 ULIRGs, 128 show an [O III] emission line blueshifted relative to the stellar continuum, i.e.,  $\nu_{50} < 0$ , indicating that the ionized gas moves toward the observer. Due to the obscuration of the dusty stellar disk to the emission in the

<sup>27</sup> [https://www.sdss.org/dr12/spectro/galaxy\\_mpajhu/](https://www.sdss.org/dr12/spectro/galaxy_mpajhu/)

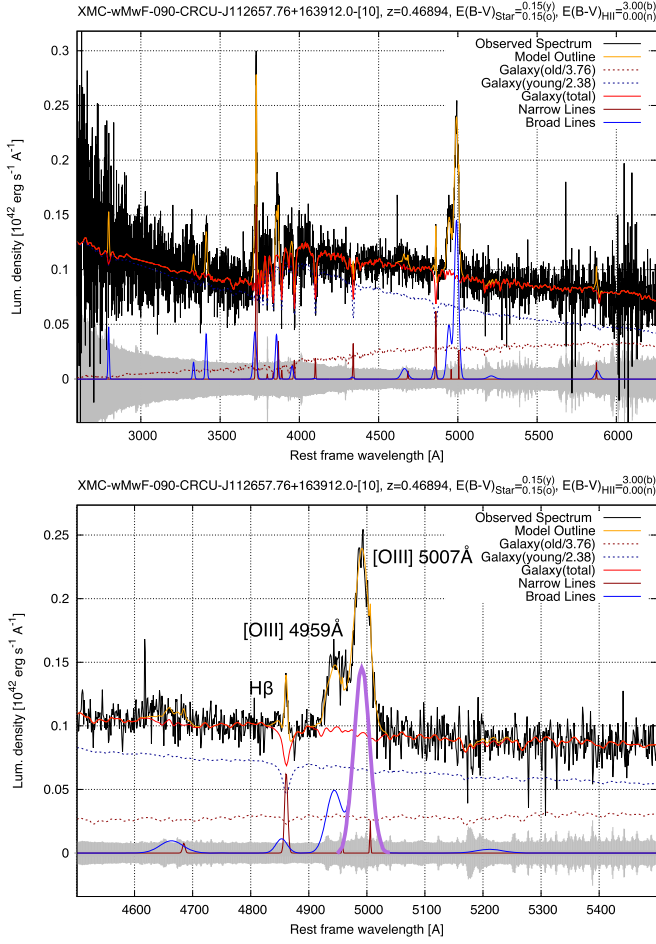


**Figure 14.** Optical spectral fitting (top) and zoom-in around the [O III] 5007 Å line (bottom) for J112657.76+163912.0, a ULIRG with an outflow velocity of  $v_{\text{out}} = 2061 \text{ km s}^{-1}$ . The broad component of its [O III] 5007 Å line is shown by the thick violet curve. Other lines are the same as those in Figure 7.

side far from the observer, we consider the observed [O III] emission line as dominated by the outflowing gas in the side near the observer. The remaining eight ULIRGs show a redshifted [O III] line ( $v_{50} > 0$ ), with three ULIRGs showing  $v_{50} > 100 \text{ km s}^{-1}$ , which could be due to predominant inflowing gas or a large inclination of the outflow direction compared to the perpendicular direction of the stellar disk.

Estimating the bulk outflow velocity from the observed line velocities is not straightforward, because the conversion depends on the geometry of the outflowing gas and the spatial distribution of velocity (Liu et al. 2013; Fiore et al. 2017). Veilleux et al. (2005) defined the maximum velocity of the outflow as  $v_{\text{out}} \approx |v_{\text{shift}}| + \text{FWHM}/2$  (see also Rupke et al. 2005; Westmoquette et al. 2012; Arribas et al. 2014), while other researchers adopted a partly different definition with a higher weight of line width, i.e.,  $v_{\text{out}} \approx |v_{\text{shift}}| + \text{FWHM}$  (Rupke & Veilleux 2013; Fiore et al. 2017). We employ the first definition assuming  $v_{\text{shift}} = v_{50}$  but replace FWHM with  $w_{80}$  following Manzano-King et al. (2019). We also compare the outflow velocity with the values from another definition,  $v_{\text{out}} = [v_{50}^2 + 3(w_{80}/2.56)^2]^{1/2}$ , which is usually used in the estimation of the kinetic energy (Harrison et al. 2014), and find that the two definitions yield consistent results with an average ratio of  $1.0 \pm 0.1$ .

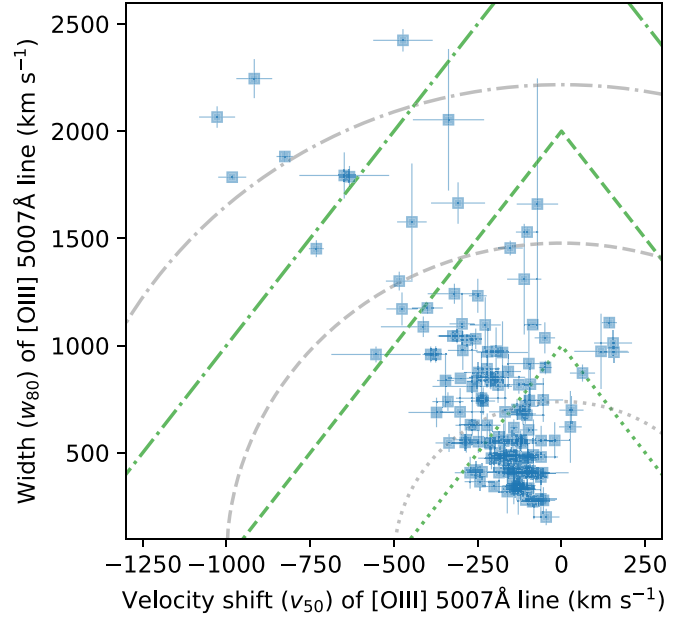


**Figure 15.** Velocity shifts ( $v_{50}$ ) and widths ( $w_{80}$ ) of 136 AKARI-selected ULIRGs with [O III] 5007 Å detection. The green lines denote the outflow velocity with the definition (this work)  $v_{\text{out}} = |v_{50}| + w_{80}/2$  of 500 (dotted), 1000 (dashed), and 1500 (dashed-dotted)  $\text{km s}^{-1}$ , respectively. The gray lines denote the outflow velocity with the kinetic energy definition (e.g., Harrison et al. 2014)  $v_{\text{out}} = [v_{50}^2 + 3(w_{80}/2.56)^2]^{1/2}$  of 500 (dotted), 1000 (dashed), and 1500 (dashed-dotted)  $\text{km s}^{-1}$ , respectively.

Finally, we compare the estimated outflow velocity ( $v_{\text{out}} = |v_{50}| + w_{80}/2$ ) with the rotation velocity ( $\sigma_{\text{star}}$ ) of the stellar disk. Here  $\sigma_{\text{star}}$  is estimated as the dispersion (FWHM / 2.35) in the absorption line features of the stellar continuum (see Appendix A for details). Among the 136 ULIRGs with [O III] detection, 87 show  $v_{\text{out}}/\sigma_{\text{rot}} > 3$  (Figure 16), suggesting that the outflow velocity exceeds the rotation velocity of the stellar disk in most of the ULIRGs.

## 5. Discussions

### 5.1. Relationship between Outflow Velocity and AGN Activity

The estimated outflow velocity ( $v_{\text{out}}$ ) and AGN bolometric luminosity ( $L_{\text{AGN}}$ ) of 136 ULIRGs with [O III] detection are shown in Figure 17 (left panel). The mean  $v_{\text{out}}$  of 54 ULIRGs with  $L_{\text{AGN}} > 3 \times 10^{11} L_{\odot}$  is  $820 \pm 460 \text{ km s}^{-1}$ , which is larger than the mean  $v_{\text{out}}$ ,  $480 \pm 200 \text{ km s}^{-1}$ , of the remaining 82 ULIRGs with  $L_{\text{AGN}} < 3 \times 10^{11} L_{\odot}$ , indicating a positive correlation between outflow velocity and AGN luminosity. We perform an ordinary least-squares bisector fit between  $v_{\text{out}}$  and  $L_{\text{AGN}}$  after normalizing with the value ranges in both the  $x$ - and  $y$ -axes in a logarithmic grid for the 136 galaxies. The Schmitt (1985) binning method is used to account for the estimated upper limit of  $L_{\text{AGN}}$  for the ULIRGs with barely any AGN detection (i.e.,  $\beta_{\text{AGN,MIR}} < 1$ ). The derived regression function is

$$\log v_{\text{out}} = 0.25 (\pm 0.02) \log L_{\text{AGN}} - 0.14 (\pm 0.23), \quad (12)$$

with  $r_s = 0.46$  and a  $p$ -value of  $2 \times 10^{-8}$ . The fitting method is also employed for the  $v_{\text{out}}$  and AGN bolometric contribution ( $f_{\text{AGN}}$ ), and the regression function is

$$\log v_{\text{out}} = 0.33 (\pm 0.03) \log f_{\text{AGN}} + 3.13 (\pm 0.04), \quad (13)$$

with  $r_s = 0.37$  and a  $p$ -value of  $1 \times 10^{-5}$ . We also investigate the association between  $v_{\text{out}}$  and the AGN Eddington ratio

( $\lambda_{\text{Edd}}$ ; Figure 18). In order to estimate the Eddington luminosity, we derive the mass of the central black hole ( $M_{\text{BH}}$ ) using the total stellar mass ( $M_{\text{star,tot}}$ ) and empirical  $M_{\text{BH}}-M_{\text{star}}$  relationship in the local universe (Reines & Volonteri 2015):

$$\log_{10}\left(\frac{M_{\text{BH}}}{10^8 M_{\odot}}\right) = 1.05 \times \log_{10}\left(\frac{M_{\text{star}}}{10^{11} M_{\odot}}\right) - 0.55. \quad (14)$$

Then, we obtain

$$\log v_{\text{out}} = 0.25 (\pm 0.02) \log \lambda_{\text{Edd}} + 2.90 (\pm 0.04), \quad (15)$$

with  $r_s = 0.34$  and a  $p$ -value of  $5 \times 10^{-5}$ .

Comparing the coefficients among the relations, i.e.,  $v_{\text{out}}-L_{\text{AGN}}$ ,  $v_{\text{out}}-f_{\text{AGN}}$ , and  $v_{\text{out}}-\lambda_{\text{Edd}}$ , we find that the outflow velocity is more tightly associated with the absolute power of the AGN ( $L_{\text{AGN}}$ ) than the relative intensity ( $f_{\text{AGN}}$  and  $\lambda_{\text{Edd}}$ ). These results suggest that intense AGN activity (e.g.,  $L_{\text{AGN}} > 3 \times 10^{11} L_{\odot}$ ,  $f_{\text{AGN}} > 0.1$ ,  $\lambda_{\text{Edd}} > 0.1$ ) is necessary to blow out a fast outflowing wind (e.g.,  $v_{\text{out}} > 1000 \text{ km s}^{-1}$ ). However, the galaxies with a powerful AGN but showing moderate outflow ( $v_{\text{out}} \sim 500 \text{ km s}^{-1}$ ) imply that the existence of a luminous AGN could not always invoke a strong outflow.

The bisector fit is also carried out only for the 46 galaxies with obvious AGN MIR excess features ( $\beta_{\text{AGN,MIR}} > 3$ ), and the regression results are shown with red lines in Figures 17 and 18 for the correlations. Compared to the results for the entire sample, the regression functions for the 46 galaxies show weaker correlations (e.g.,  $r_s = 0.26$  versus 0.46 for  $v_{\text{out}}-L_{\text{AGN}}$  coefficients), which is partly due to the lack of faint AGN sources (e.g.,  $L_{\text{AGN}} < 10^{11} L_{\odot}$ ) among the 46 galaxies.

Finally, we test the association between  $v_{\text{out}}$  and stellar bolometric luminosity ( $L_{\text{star}}$ ; Figure 17, right panel). The bisector fit function is

$$\log v_{\text{out}} = 0.86 (\pm 0.07) \log L_{\text{SF}} - 7.99 (\pm 0.82), \quad (16)$$

with  $r_s = 0.29$  and a  $p$ -value of  $7 \times 10^{-4}$ . The coefficient of the  $v_{\text{out}}-L_{\text{SF}}$  relation, 0.29, is smaller than the  $r_s = 0.46$  of the  $v_{\text{out}}-L_{\text{AGN}}$  relation, implying that the outflow velocity is more tightly associated with AGN activity.

## 5.2. Coexistence of Fast Outflows and Intense SBs

In the evolutionary scenario of massive galaxies, the AGN-driven outflows are required to be powerful enough to expel the gas completely from the HG potentials to effectively terminate SF in the HGs and remove the fuel for the proceeding accretion onto the black holes (e.g., Di Matteo et al. 2005; Hopkins et al. 2008). In order to check whether the fast outflowing gas is capable of escaping from the gravitational potential of the HG and the embedded halo, we estimate the escape velocity in different spatial scales.

First, we model the gravitational potential profile using the combination of bulge, disk, and dark matter halo components. The bulge and disk components are assumed to follow the de Vaucouleurs and exponential laws, respectively (e.g., Sofue et al. 2009). We adopt the average bulge-to-disk ratio of local ULIRGs, i.e., 1.5 (Veilleux et al. 2006), to estimate the masses of the bulge and disk from the total stellar mass (Equation (8)). The radii of the bulge and disk components are estimated using the empirical relationship between the radius and mass of local early- and late-type galaxies, respectively (Shen et al. 2003). The halo mass is estimated using stellar mass and the

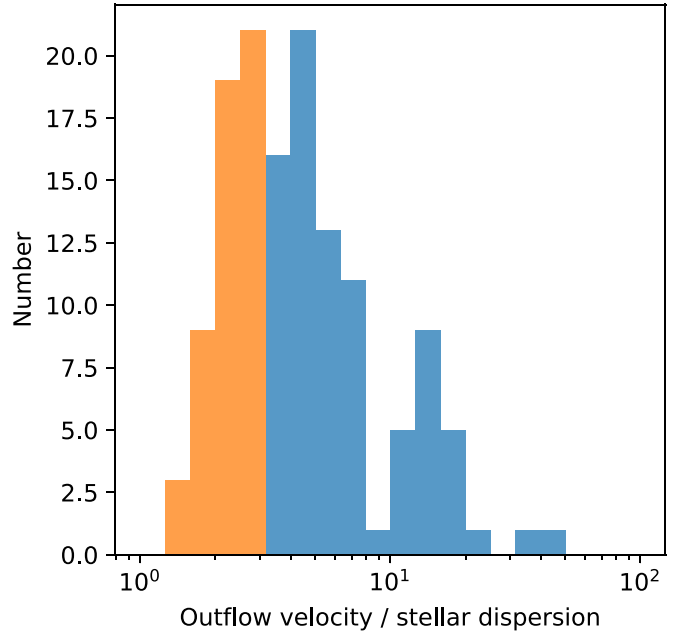


**Figure 16.** Histogram of the ratio  $v_{\text{out}}/\sigma_{\text{star}}$ , where  $v_{\text{out}}$  is the outflow velocity and  $\sigma_{\text{rot}}$  is the velocity dispersion of stellar continuum. Blue and orange histograms denote galaxies with  $v_{\text{out}}/\sigma_{\text{star}} > 3$  and  $< 3$ , respectively.

galaxy-to-halo mass ratio, which is a function of the galaxy stellar mass, from the multi-epoch abundance matching simulation (Moster et al. 2013). The gravitational potential at a given distance ( $r$ ) from the center,  $\Psi_{\text{halo}}(r)$ , can be calculated using a spherical Navarro–Frenk–White (NFW) potential profile (Navarro et al. 1996; Łokas & Mamon 2001). Then, the total gravitational potential can be calculated as  $\Psi(r) = \Psi_{\text{bulge}}(r) + \Psi_{\text{disk}}(r) + \Psi_{\text{halo}}(r)$ . We define the escape velocity as the minimum velocity required for the gas to travel from the galaxy center to an outer radius  $r_{\text{out}}$ , i.e.,  $v_{\text{esc}} = \sqrt{2|\Psi(r_{\text{in}} = 0) - \Psi(r_{\text{out}})|}$ . Then, the escape velocity of the halo, i.e.,  $v_{\text{esc,halo}}$ , is calculated at  $r_{\text{out}} = r_{\text{vir}}$ , where  $r_{\text{vir}}$  is the virial radius of the halo ( $\sim 500 \text{ kpc}$  for a galaxy with  $M_{\text{star}} = 10^{11} M_{\odot}$ ; see also Section 5.2.2 of Harrison et al. 2012). The escape velocity of the galaxy, i.e.,  $v_{\text{esc,gal}}$ , is calculated for  $r_{\text{out}} = 0.1 r_{\text{vir}}$ . Note that both  $v_{\text{esc,halo}}$  and  $v_{\text{esc,gal}}$  could be overestimated; since we assume a starting point at the center of the galaxy, the proportion of the overestimation is 10%–15% if we consider a starting point at the galaxy outskirts region, i.e.,  $r_{\text{in}} = 0.01 r_{\text{vir}}$  (5 kpc with  $M_{\text{star}} = 10^{11} M_{\odot}$ ) from the galaxy center (gray curves in Figure 19, top panel). The 136 ULIRGs with [O III] detections can be divided into three groups: (1) five ULIRGs with  $v_{\text{out}} > v_{\text{esc,halo}}$ ; (2) six ULIRGs with  $v_{\text{esc,gal}} < v_{\text{out}} \leq v_{\text{esc,halo}}$ ; and (3) 125 ULIRGs with  $v_{\text{out}} \leq v_{\text{esc,gal}}$  (Figure 19).

The comparison between the outflow and escape velocity suggests that five ULIRGs possess outflows that are fast enough to escape from the gravitational potential of the host halos, and the other six ULIRGs show the capability to escape from the HGs. However, those galaxies possess a comparable or even higher SFR and specific SFR (sSFR) compared to the ULIRGs with moderate outflows ( $v_{\text{out}} \leq v_{\text{esc,gal}}$ ; see Figure 19, middle and bottom panels). The coexistence of the strong outflow and vigorous SB possibly suggests that the SF has not yet been suppressed, even though the powerful wind shows the capability to blow the gas out of the intergalactic environment ( $v_{\text{out}} > v_{\text{esc,halo}}$ ). It is probable that the wind is clumpy, which

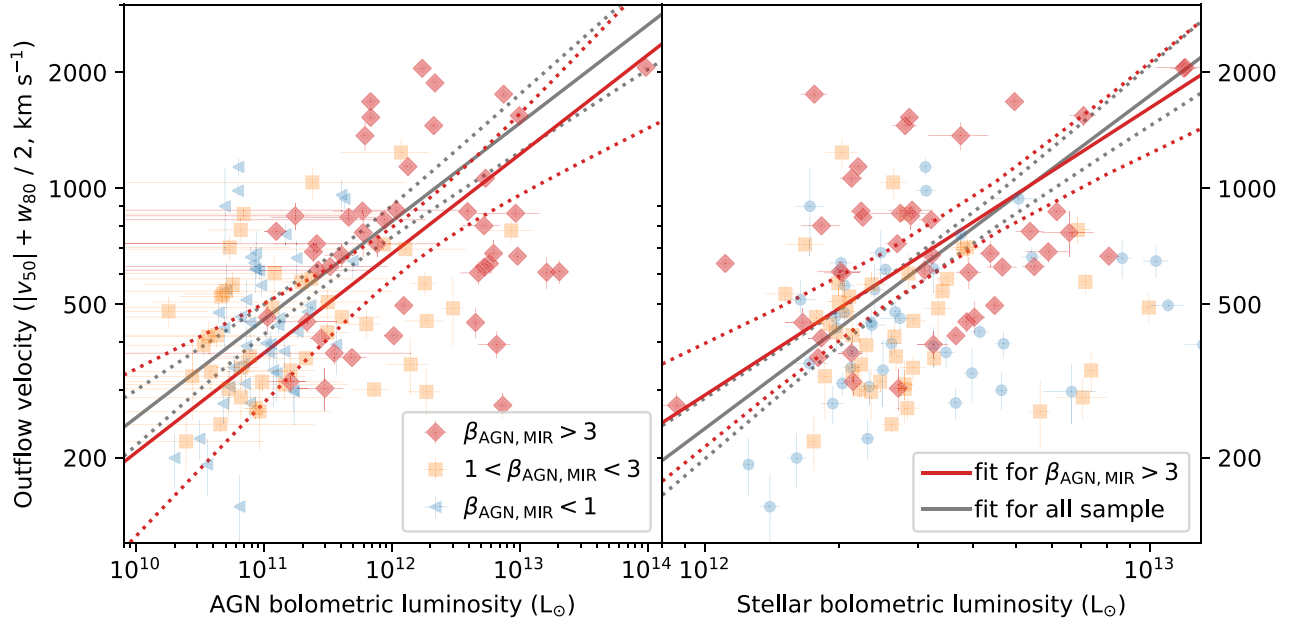


**Figure 17.** The [O III] outflow velocity ( $v_{\text{out}}$ ) vs. AGN ( $L_{\text{AGN}}$ ; left) and SF ( $L_{\text{SF}}$ ; right) bolometric luminosity for 136 galaxies with an [O III] line detection. The red, orange, and blue symbols correspond to the detection ratios of AGN MIR excess (see Section 4.1 and Figure 10). Note that for the galaxies with no AGN detection ( $\beta_{\text{AGN, MIR}} < 1$ ), the shown  $L_{\text{AGN}}$  is the estimated upper limit. The gray solid line is the ordinary least-squares bisector fitting function for the entire sample, and the red solid line is for the sources with significantly detected AGNs (red diamonds). The dotted lines denote the 95% confidence bands of the fitting lines.

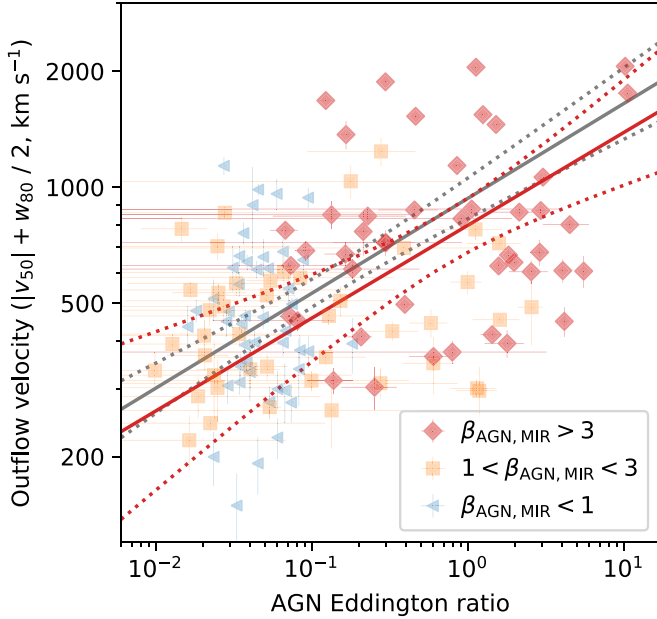


**Figure 18.** The [O III] outflow velocity ( $v_{\text{out}}$ ) vs. AGN Eddington ratio ( $\lambda_{\text{Edd}}$ ). The lines and symbols are the same as in Figure 17.

could pass through the ISM without a severe influence on the star-forming region.

Positive AGN feedback, i.e., outflow compressing the ISM and enhancing SF, could be an alternative possibility. Ishibashi et al. (2013) discussed the scenario that the AGN feedback triggers SF and contributes to the buildup of the outskirts region as the gas is being pushed out by the outflow. Their scheme predicts that the triggered SFR (about  $100 M_{\odot} \text{ yr}^{-1}$ ) scales with the outflow velocity. Direct evidence for SF within the galactic outflow itself in a merging system, IRAS F23128–5919, has been reported by Maiolino et al. (2017). The SFR in the outflow,  $15\text{--}30 M_{\odot} \text{ yr}^{-1}$ , can contribute to

about 25% of the total SFR in the galaxy. A spatially resolved spectroscopic survey to map the outflow and SF activity is required to determine if a much higher SFR ( $300\text{--}3000 M_{\odot} \text{ yr}^{-1}$ ) can be enhanced by AGN-driven wind in the AKARI-selected ULIRGs.

### 5.3. No Clear Evidence of the Evolution Path from SF- to AGN-dominated ULIRGs

In the commonly accepted scenario of the evolution of massive galaxies (e.g., Sanders et al. 1988; Hopkins et al. 2008; Netzer 2009; Casey et al. 2014; Ichikawa et al. 2014), ULIRGs play an intermediate role in the transition from normal star-forming galaxies to quiescent elliptical galaxies that host luminous quasars as they evolve from a cold (red MIR–FIR color), SF-dominated phase to a warm (blue MIR–FIR color), AGN-dominated phase. Figure 20 shows the SF dust luminosity ( $L_{\text{SF, dust}} = L_{\text{ISM}} + L_{\text{BC}}$ , where  $L_{\text{ISM}}$  and  $L_{\text{BC}}$  are the dust luminosity in the diffuse region and the birth clouds, respectively) and AGN torus dust luminosity ( $L_{\text{torus}}$ ) of AKARI-selected ULIRGs estimated from the SED decomposition. In order to compare the results of the ULIRGs to other samples, here we take the dust reemitted luminosities instead of the intrinsic primary radiation discussed in Section 4. The AGN IR contribution can be described as  $f_{\text{AGN, IR}} = L_{\text{torus}} / (L_{\text{torus}} + L_{\text{SF, dust}})$ . The optical–IR SED fitting derives an empirical function between  $f_{\text{AGN, IR}}$  and the AGN bolometric contribution  $f_{\text{AGN}}$ , i.e.,

$$\frac{f_{\text{AGN, IR}}^{-1} - 1}{f_{\text{AGN}}^{-1} - 1} = \frac{L_{\text{SF, dust}} / L_{\text{star}}}{L_{\text{torus}} / L_{\text{AGN}}} = 4 \pm 2, \quad (17)$$

for the 149 AKARI-selected ULIRGs.

In Figure 20, we also show the  $L_{\text{SF, dust}}$  and  $L_{\text{torus}}$  of LIRGs ( $10^{11} L_{\odot} \leq L_{1-1000} < 10^{12} L_{\odot}$ ) and normal star-forming galaxies ( $L_{1-1000} < 10^{11} L_{\odot}$ ), which are also selected from the AKARI FIR catalog (see Section 2), as well as the AKARI-selected

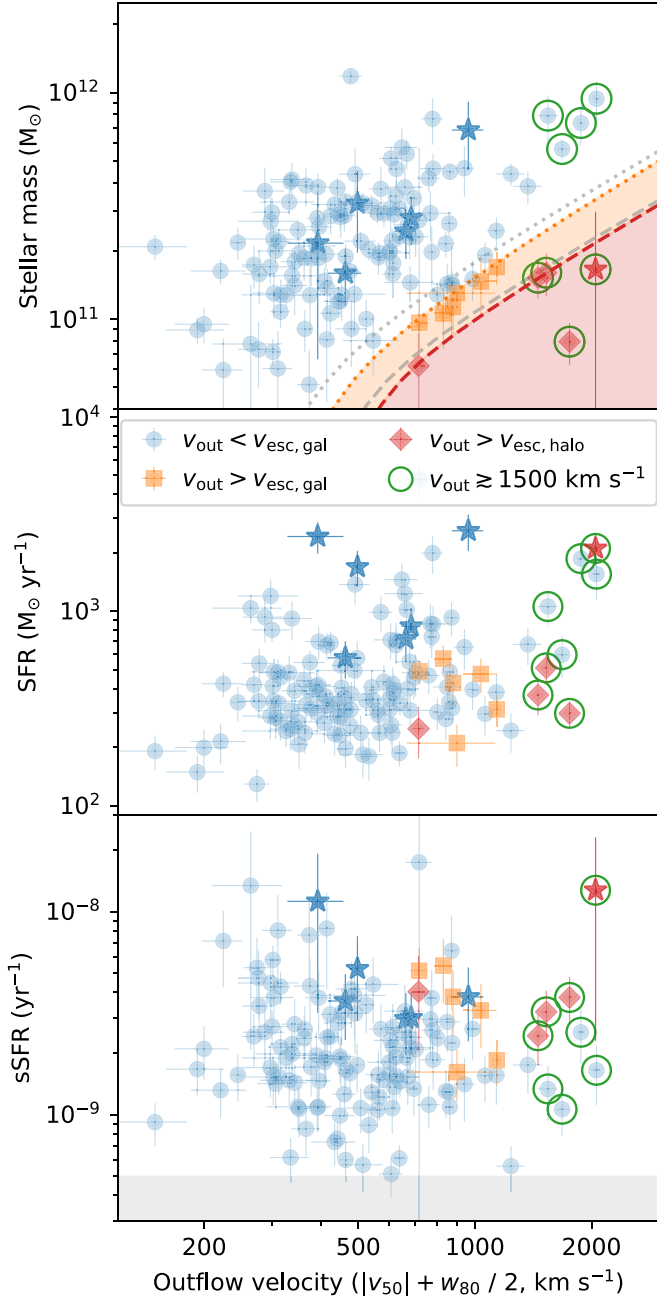


**Figure 19.** Top panel: stellar mass of the HG vs. outflow velocity ( $v_{\text{out}}$ ). The galaxies with  $v_{\text{out}} > v_{\text{esc,halo}}$ ,  $v_{\text{esc,gal}} < v_{\text{out}} \leq v_{\text{esc,halo}}$ , and  $v_{\text{out}} \leq v_{\text{esc,gal}}$  are shown in red diamonds, orange squares, and blue circles, respectively. Stars denote the galaxies spectroscopically identified by FOCAS. The green open circles mark the eight galaxies with extremely fast outflow ( $v_{\text{out}} \gtrsim 1500 \text{ km s}^{-1}$ ). The red dashed and orange dotted curves show the escape velocity of the halo and galaxy, i.e.,  $v_{\text{esc,halo}}$  and  $v_{\text{esc,gal}}$ , respectively, starting from the galaxy center for a galaxy at  $z = 0.23$ , the average redshift of the sample. The gray dashed and dotted curves show the same estimates but starting from the galaxy outskirts region, i.e., approximately 5 kpc from the center. Middle panel: SFR vs.  $v_{\text{out}}$  for AKARI-selected ULIRGs, with the same symbols as the upper panel. Bottom panel: sSFR vs.  $v_{\text{out}}$  with the same symbols. The gray shaded region denotes the star-forming main sequence ( $z = 0-0.5$ ; Peng & Maiolino 2014).

ULIRGs identified as type 1 quasars with optical spectra (see Section 3.1). The  $L_{\text{SF,dust}}$  and  $L_{\text{torus}}$  are estimated using the two-band method (Equation (3)) for the LIRGs, star-forming galaxies, and quasars. In addition, we also plot the results of the local optically selected Seyfert 2 galaxies presented by

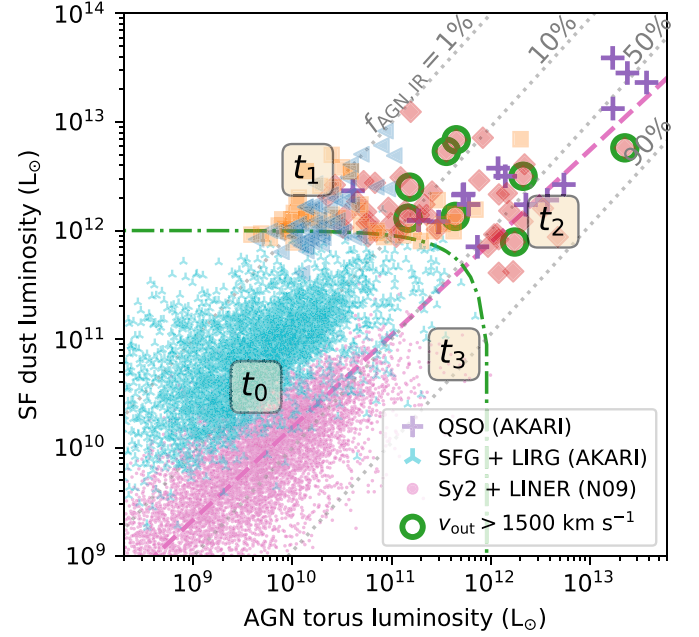


**Figure 20.** The SF dust luminosity ( $L_{\text{SF,dust}}$ ) vs. AGN torus luminosity ( $L_{\text{torus}}$ ) of AKARI-selected ULIRGs. The red diamonds, orange squares, and blue circles denote the ULIRGs with AGN MIR excess ratios  $\beta_{\text{AGN,MIR}} < 1$ ,  $1 < \beta_{\text{AGN,MIR}} < 3$ , and  $\beta_{\text{AGN,MIR}} > 3$ , respectively (see Section 4.1 and Figure 10). The green open circles show the eight ULIRGs with  $v_{\text{out}} \gtrsim 1500 \text{ km s}^{-1}$ . The green dashed-dotted curve shows the rough selection threshold for ULIRGs ( $L_{\text{IR,total}} \simeq L_{\text{SF,dust}} + L_{\text{torus}} \geq 10^{12} L_{\odot}$ ). The violet plus signs show the AKARI-selected luminous type 1 quasars (see Section 3.1). The cyan symbols denote the normal star-forming galaxies and LIRGs selected from the AKARI sample with  $L_{1-1000} < 10^{12} L_{\odot}$ . The purple dots with the dashed fitting line show the local Seyfert 2 galaxy sample of Netzer (2009). See Section 5.3 for the estimation method of  $L_{\text{SF,dust}}$  and  $L_{\text{torus}}$  for the reference quasars and galaxies. The gray dotted lines denote the positions with AGN IR contributions ( $f_{\text{AGN,IR}} = L_{\text{torus}} / (L_{\text{torus}} + L_{\text{SF,dust}})$ ) of 1%, 10%, 50%, and 90%.

Netzer (2009). The  $L_{\text{torus}}$  of the Seyfert 2 galaxies is estimated from the reported AGN bolometric luminosity (Netzer 2009; see their Figure 13) with the empirical  $L_{\text{AGN}}-L_{\text{MIR}}$  relationship of Ichikawa et al. (2014).

The time tags, i.e.,  $t_0-t_3$ , in Figure 20 show a suggested evolution path for a “single event” merger (Netzer 2009). The merger occurring at time  $t_0$  leads to a catastrophic gas inflow and intense SF activity, which moves the system to an SF-dominated ULIRG period at  $t_1$ . As the inflowing gas reaches into the central region of the galaxy, the luminosity of the AGN increases with peak activity at  $t_2$ . The SFR begins to decrease due to the consuming of the gas and the feedback effect of the SB and/or AGN. Finally, both the SF and AGN activities decay as a result of the diminishing supply of cold gas of the star-forming region and the central black hole ( $t_3$ ).

One prediction of the evolutionary scenario is that as the ULIRG evolves to the AGN luminous phase, the outflow becomes intense and provides one of the main mechanisms to blow out the gas and dust, finally terminating the SF in the galaxy. The correlation between outflow and AGN activity is consistent with our results from the [O III] and MIR observations (Section 5.1). However, the ULIRGs with extreme outflows do not show the suppression of SFR compared to the ULIRGs with moderate outflows (Section 5.2).

Another prediction of the merger scenario is that ULIRGs experience continuous buildup of stellar mass as a result of the intense SFR during their lifetimes (e.g.,  $t_1-t_2$  in Figure 20);

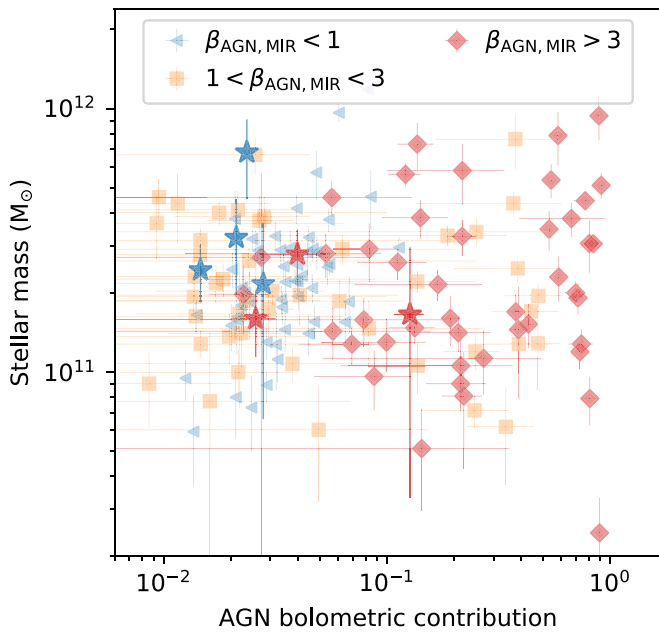


**Figure 21.** Total stellar mass ( $M_{\text{star,tot}}$ ) vs. AGN bolometric contribution ( $f_{\text{AGN}}$ ) of AKARI-selected ULIRGs. The red, orange, and blue symbols correspond to the detection ratios of AGN MIR excess (see Section 4.1 and Figure 10). The stars denote the galaxies spectroscopically identified by FOCAS, and the other symbols show the galaxies spectroscopically identified by SDSS. The result suggests that there is no apparent difference in stellar mass between SF- and AGN-dominated ULIRGs, i.e., a noncorrelation between  $M_{\text{star,tot}}$  and  $f_{\text{AGN}}$ .

thus, the later-stage, AGN-dominated (higher  $f_{\text{AGN}}$ ) ULIRGs are expected to possess larger stellar mass than the early-stage, SF-dominated ULIRGs. The comparison between the total stellar mass ( $M_{\text{star,tot}}$ ) and the bolometric AGN contribution ( $f_{\text{AGN}}$ ) is shown in Figure 21. However, the coefficient  $r_s$  is close to zero (0.03) with a high  $p$ -value of 0.7, which indicates that there is no correlation between  $M_{\text{star,tot}}$  and  $f_{\text{AGN}}$ . The result of the noncorrelation still holds if only ULIRGs with  $\beta_{\text{AGN}} > 3$  are considered ( $r_s$  of 0.07 and  $p$ -value of 0.6). Therefore, we consider that there is no clear evidence of stellar buildup from SF- to AGN-dominated ULIRGs with the AKARI-selected sample.

A similar check is performed for the  $E(B - V)$  estimated from stellar continua, which reflect the diffuse dust extinction in the star-forming region. Within the evolutionary scenario, the AGN-dominated ULIRGs are expected to possess more transparent star-forming regions with lower  $E(B - V)$ , as a result of the intense outflow that blows the gas and dust out of the star-forming regions (e.g., Veilleux et al. 2009; Hou et al. 2011). However, the result from the AKARI-selected sample still shows no correlation between  $E(B - V)$  and  $f_{\text{AGN}}$ , with a small coefficient,  $r_s = -0.1$ , and a high  $p$ -value of 0.1.

In summary, although we find the correlation between outflow and AGN activity, our results do not show clear evidence, e.g., stellar buildup, of the transition link from SF- to AGN-dominated ULIRGs. One possible explanation is that the timescale of the phase transition is much shorter than the lifetime of the ULIRGs; i.e., it takes a much shorter time for gas to move into the vicinity of the central black hole than the duration of intense SBs (e.g., 100 Myr), and thus the SF- and AGN-dominated ULIRGs could possess similar stellar populations. Several simulation works reported that the fast transition is possible at some conditions; e.g., the mass ratio of the progenitor galaxies of the merger is much larger than 1:1

(Johansson et al. 2008). It is also possible that the selected ULIRG sample is biased to massive galaxies ( $10^{11}$ – $10^{12} M_{\odot}$ ); thus, the accumulated stellar mass during the ULIRG phase (e.g.,  $10^{10.5} M_{\odot}$ , assuming an SFR of  $300 M_{\odot} \text{ yr}^{-1}$  and 100 Myr duration) could not significantly affect the total stellar mass of the galaxy.

## 6. Conclusions

In order to understand the stellar population and outflow properties of ULIRGs to place observational constraints on their evolutionary path, we construct a  $90 \mu\text{m}$  flux-limited catalog of 1077 ULIRGs, which are selected from the AKARI FIR all-sky survey by utilizing the SDSS optical and WISE MIR imaging data. Of the 1077 ULIRGs, 202 are spectroscopically identified by SDSS and Subaru/FOCAS observations, in which 149 ULIRGs possess galaxy-dominated optical spectra. Thanks to the deeper depth and higher resolution of AKARI compared to the previous IRAS survey and reliable identification from WISE MIR pointing, the sample is unique in identifying optically faint ( $i \sim 20$ ) IR-bright galaxies, which could be missed in previous surveys. Compared to previous works on the stellar population of ULIRGs that focused on narrow-line objects (e.g., Hou et al. 2011), our ULIRG sample also provides the unique opportunity to study the evolution of ULIRGs with extremely fast outflows. The main results are as follows.

(1) A self-consistent spectrum–SED decomposition method, which constrains stellar population properties in SED modeling based on spectral fitting results, has been employed for 149 ULIRGs with HG-dominated spectra (Section 3). They are identified as massive galaxies ( $M_{\text{star}} \sim 10^{11}$ – $10^{12} M_{\odot}$ ) associated with intense SF activity (SFR  $\sim 400$ – $2000 M_{\odot} \text{ yr}^{-1}$ ). Twelve ULIRGs possess SFRs exceeding  $1000 M_{\odot} \text{ yr}^{-1}$ , and the ULIRG J115458.02+111428.8 even shows an SFR up to  $5000 M_{\odot} \text{ yr}^{-1}$ , indicating one of the most intense SBs at  $z \sim 0.5$  (Section 4.2).

(2) The ULIRGs cover a large range of AGN activity, with bolometric luminosity from  $10^{10}$  to  $10^{13} L_{\odot}$ , and the outflow velocity measured from the [O III] 5007 Å emission line shows a correlation with the AGN bolometric luminosity. Several galaxies show extremely fast outflow with  $v_{\text{out}}$  close to  $2000 \text{ km s}^{-1}$ . The outflow velocity of five ULIRGs even exceeds the escape velocity of the host halos. However, the coexistence of the strong outflows and vigorous SBs suggests that the SF has not yet been suppressed by the outflow during the ULIRG phase (Sections 4.1, 4.3, 5.1, and 5.2).

(3) There are no significant discrepancies of the stellar population, e.g., stellar mass and dust extinction, between ULIRGs with weak and powerful AGNs. The results do not show evidence of the transition from SF- to AGN-dominated ULIRGs as predicted by the merger-induced evolutionary scenario. One possible explanation is that the timescale of the phase transition from SF- to AGN-dominated ULIRGs is much shorter than the lifetime of ULIRGs (Section 5.3).

We thank the anonymous referee for the constructive advice. We thank Marko Stalevski for providing the SKIRTor torus SED library and Angelos Nersesian for the discussion of the THEMIS ISM dust model. This work was supported by the Program for Establishing a Consortium for the Development of Human Resources in Science and Technology, Japan Science and Technology Agency (JST), and partially supported by the

Japan Society for the Promotion of Science (JSPS) KAKENHI (18K13584; KI). This research is based on data collected at Subaru Telescope, which is operated by the National Astronomical Observatory of Japan. This research is based on observations with AKARI, a JAXA project with the participation of ESA. This publication makes use of data products from the Wide-field Infrared Survey Explorer, which is a joint project of the University of California, Los Angeles, and the Jet Propulsion Laboratory/California Institute of Technology, funded by the National Aeronautics and Space Administration. Funding for the Sloan Digital Sky Survey IV has been provided by the Alfred P. Sloan Foundation, the U.S. Department of Energy Office of Science, and the Participating Institutions. The SDSS-IV acknowledges support and resources from the Center for High-Performance Computing at the University of Utah. The SDSS website is [www.sdss.org](http://www.sdss.org). The SDSS-IV is managed by the Astrophysical Research Consortium for the Participating Institutions of the SDSS Collaboration, including the Brazilian Participation Group, the Carnegie Institution for Science, Carnegie Mellon University, the Chilean Participation Group, the French Participation Group, Harvard-Smithsonian Center for Astrophysics, Instituto de Astrofísica de Canarias, The Johns Hopkins University, Kavli Institute for the Physics and Mathematics of the Universe (IPMU)/University of Tokyo, the Korean Participation Group, Lawrence Berkeley National Laboratory, Leibniz Institut für Astrophysik Potsdam (AIP), Max-Planck-Institut für Astronomie (MPIA Heidelberg), Max-Planck-Institut für Astrophysik (MPA Garching), Max-Planck-Institut für Extraterrestrische Physik (MPE), the National Astronomical Observatories of China, New Mexico State University, New York University, the University of Notre Dame, Observatório Nacional/MCTI, The Ohio State University, Pennsylvania State University, Shanghai Astronomical Observatory, the United Kingdom Participation Group, Universidad Nacional Autónoma de México, the University of Arizona, the University of Colorado Boulder, the University of Oxford, the University of Portsmouth, the University of Utah, the University of Virginia, the University of Washington, the University of Wisconsin, Vanderbilt University, and Yale University.

## Appendix A

### Details of the Optical Spectral Fitting Procedure

The optical spectral fitting procedure is modified from the Quasar Spectral Fitting package (QSFit, v1.3.0; Calderone et al. 2017), which is an IDL package based on MPFIT (Markwardt 2009). The original code of QSFit is optimized to the analyses of spectra of AGN-dominated systems, e.g., quasar spectra with broad Balmer lines. We modified the codes to support the fitting with the HG component with multiple stellar populations, as well as the automatic separation between quasar and HG spectra under a given threshold. The details of the fitting procedure are explained as follows.

#### A.1. Components in Spectral Fitting

The model used to fit the observed spectrum is a collection of several components, which can be classified into three categories: (1) AGN continua (Table A1), e.g., power-law continuum; (2) HG continua, e.g., (Table A2) stellar

continuum; and (3) emission lines (Table A3), e.g., H $\alpha$  and [O III]. The AGN continua consist of a bending power-law continuum, a Balmer emission continuum, and an iron emission line pseudocontinuum. The power-law continuum, i.e.,  $L_\lambda \propto \lambda^\alpha$ , represents the radiation directly from the accretion disk. In the spectral fitting, the index  $\alpha$  is a free parameter with an initial value of  $-1.76$  (Vanden Berk et al. 2001) and a range of  $\pm 0.5$ . The Balmer continuum is described by the electron temperature ( $T_e$ ) and optical depth ( $\tau_{\text{BE}}$ ) at the Balmer edge (3645 Å; Dietrich et al. 2012). In order to avoid a degeneracy between the parameters, we fix  $\tau_{\text{BE}} = 1$ , following Dietrich et al. (2012). Here  $T_e$  is set as a free parameter to obtain a variable slope of the Balmer continuum, with an initial value of  $T_e = 10,000$  K and a range of 7500–30,000 K. In addition, the pseudocontinuum generated from blending high-order Balmer emission lines (H11–H50) is also considered in the fitting procedure. The line intensities are tied using the theoretical ratios of Storey & Hummer (1995) at a fixed electron density of  $10^9 \text{ cm}^{-3}$  with the same temperature as the Balmer continuum. The last AGN continuum component is the iron pseudocontinuum from the blending of Fe II emission lines. The iron templates of narrow-line Seyfert 1 galaxy I ZW 1 from Vestergaard & Wilkes (2001, hereafter VW2001; 1420–3090 Å), Véron-Cetty et al. (2004, hereafter VC2004; 3500–7200 Å), and Tsuzuki et al. (2006, hereafter TK2006; 2200–3500 and 4200–5600 Å) are used in the fitting procedure. In order to obtain a continuous iron template, we renormalize the UV template of VW2001 to TK2006 using the integrated flux at 2200–2700 Å and the optical template of VC2004 to TK2006 using the integrated flux at 5100–5600 Å. Finally, the continuous iron template is generated by connecting the VW2001 template at 1420–2200 Å, the TK2006 template at 2200–3500 Å, and the VC2004 template at 3500–7200 Å. Note that the public templates of VW2001, VC2004, and TK2006 were unreddened using different Galactic extinction laws; therefore, before the connection with each other, we redden the public templates with the different extinction laws to reproduce the original observed spectra. The generated template is then corrected for the Galactic extinction using the same CCM extinction law (Cardelli et al. 1989) with  $E(B - V) = 0.105$  (Vestergaard & Wilkes 2001) and corrected for the intrinsic extinction using the Calzetti et al. (2000) extinction law with  $E(B - V) = 0.10$  (Tsuzuki et al. 2006).

As for the SFH in the spectral fitting, we assume two stellar populations. One is a underlying MS population, and the other represents the ongoing SB population. Each population is described with a composite stellar population ( $S_{\text{CSP}}$ ), which can be calculated by convolving the single stellar population ( $S_{\text{SSP}}(t, Z)$ ) and the SFH ( $\text{SFR}(t)$ ),

$$S_{\text{CSP}}(t_p) = \int_{t_0}^{t_p} \text{SFR}(t) S_{\text{SSP}}(t_p - t, Z) dt, \quad (\text{A1})$$

assuming that both the IMF and metallicity are time-independent, where  $t_p$  and  $t_0$  are the present time and the time when the galaxy began to form. In this work, we adopt the SSP library of Bruzual & Charlot (2003) with a Salpeter (1955) IMF and solar metallicity ( $Z = 0.02$ ). The  $\text{SFR}(t)$  values of the MS and SB components are modeled with  $\text{SFR}_{\text{MS}}(t) = \text{SFR}_{\text{MS}}(t_0) \exp(-(t - t_0)/\tau_{\text{SF}})$  and  $\text{SFR}_{\text{SB}}(t) = \text{constant}$ , respectively. In order to avoid the degeneracy between the timescale of SF ( $\tau_{\text{SF}}$ ) and the beginning time of the galaxy ( $t_{0, \text{gal}}$ ), we fix  $\tau_{\text{SF}}$  to 1 Gyr, which is a typical

value for local massive galaxies with stellar mass  $M_{\text{star}} > 10^{10} M_{\odot}$  in the simulation of galaxy evolution (0.5–1.5 Gyr; Hahn et al. 2017; Wright et al. 2019). Therefore, the  $S_{\text{CSP}}$  of the MS and SB components is only determined by the maximum stellar age ( $A_{\text{max}} = t_p - t_0$ ) of each population. The  $A_{\text{max}}$  of the MS and SB populations is constrained in the range of [1 Gyr, min(15 Gyr,  $A_{\text{universe}}$ )] and [30 Myr, 300 Myr], respectively, where  $A_{\text{universe}}$  denotes the age of the universe at the redshift of the galaxy in units of Gyr. The range of  $A_{\text{max}}$  of the SB population is determined according to the simulation result of galaxy merging (Hopkins et al. 2008), which suggests a typical duration of the SB of 100 Myr.

In the fitting procedure, we account for most of the emission lines that could be covered by the observed spectrum from Ly $\alpha$  to [S III] 9531 Å. The majority of the emission lines are represented with narrow and broad Gaussian profiles.<sup>28</sup> The velocity shift ( $v_{\text{off}}$ ) relative to the systemic redshift for the narrow and broad components is constrained in the range of [−500, 500] and [−1500, 500] km s<sup>−1</sup>, respectively. The FWHMs of the narrow and broad components are constrained in the range of [100, 1000] and [1000, 10<sup>4</sup>] km s<sup>−1</sup>, respectively. The line intensity of the Balmer emission lines (H $\alpha$ –H10) is tied with the theoretical ratios of Storey & Hummer (1995). The initial ratios for both narrow and broad Balmer lines are taken with an electron temperature of 10<sup>4</sup> K and electron density of 100 cm<sup>−3</sup> to represent the condition of the H II region or AGN NLR. If the spectrum is identified as quasar-dominated (in the following step 2), broad Balmer lines from AGN BLRs are considered, and the line ratios are taken with an electron temperature of 10<sup>4</sup> K and electron density of 10<sup>9</sup> cm<sup>−3</sup>. The velocity shift and FWHM of the Balmer lines are tied to each other for the narrow and broad components, respectively.<sup>29</sup> The tied Balmer emission lines are used not only to estimate the extinction in the nebular gas by comparing the theoretical and observed ratios but also to improve the fitting quality of the stellar continuum by reducing the contamination of emission lines in the decomposition of absorption line features. The Balmer absorption line series, e.g., the H7 and Ca H complex, are important features to identify the contribution of the stellar continuum and estimate the ages of the MS and SB populations. One example is shown in Figure A1. In addition to Balmer lines, we also fix the ratios of a series of forbidden line doublets, e.g., [O II] 3726, 3729 Å and [O III] 4959, 5007 Å, for which the line ratios are fixed to theoretical ratios calculated using P<sub>YNeb</sub> (Luridiana et al. 2015) under the typical temperature ( $T_e = 10^4$  K) and electron density ( $n_e = 100$  cm<sup>−3</sup>) of the H II regions and AGN NLR. The theoretical line ratios for Balmer lines and other forbidden line doublets are summarized in Table A4. Note that although the velocity shift and FWHM of the [S II] 6716, 6731 Å doublets are tied to each other, the line ratios for both the narrow and broad components are not fixed to theoretical values but rather set as free parameters in the fitting procedure. The individual absorption component is only enabled for Ly $\alpha$ , Si IV 1394 Å, C IV 1548 Å, and C III 1909 Å to account for the absorbers in the

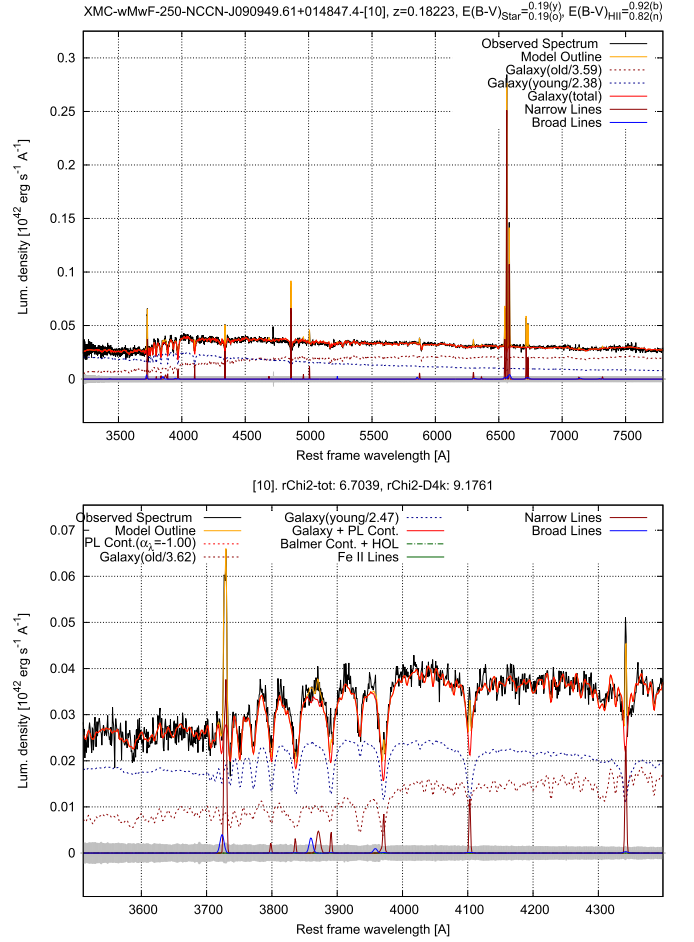


**Figure A1.** Example of tied Balmer emission lines (H $\alpha$ –H10; top panel) and the fitting for Balmer absorption lines around 4000 Å (bottom panel) for the ULIRG J090949.61+014748.4. The observed spectrum is shown in black, and the measurement error is shown in gray. The red and blue dotted curves denote the best-fit continuum of MS and TSB, respectively. The red and blue solid curves show the narrow and broad emission lines, respectively.

AGN BLR. The “unknown lines” in the original QSFIT code are disabled to avoid invoking unknown uncertainties.

In the spectral fitting, the dust reddening ( $E(B - V)$ ) is a general parameter for all of the continuum and line components, although not all of them are free parameters. In the default case, the  $E(B - V)$  values of the MS stellar continuum, iron pseudocontinuum, and narrow and broad Balmer lines are fit independently, and the extinctions of other components are tied to one of the above four components. If the narrow (or broad) component of the second-brightest Balmer line (which is usually H $\beta$  or H $\gamma$  when H $\alpha$  is not available) is severely weak, i.e., with S/N < 1, then the extinction of narrow (or broad) lines is also tied to the value of other components, e.g., the  $E(B - V)$  of the MS stellar continuum. A detailed tying relationship of extinction estimation is summarized in Table A5.

In order to build a self-consistent spectrum–SED decomposition method, we adopt the extinction law calculated by Jones et al. (2013) with the DustEM dust extinction and emission calculator (Compiègne et al. 2011) for the THEMIS dust model, which is used in the following SED decomposition method to reproduce the thermal emission of interstellar dust. Note that the detailed extinction law depends on the size distribution of ISM dust; for the sake of simplicity, in this

<sup>28</sup> The NV 1239 Å line only has narrow component to avoid the blending with Ly $\alpha$ . The Mg II 2796 Å line only has one component with a wide FWHM range ([100, 10<sup>4</sup>] km s<sup>−1</sup>) to avoid degeneracy with the iron template.

<sup>29</sup> We set a tolerance of 50 km s<sup>−1</sup> for the velocity shift of the narrow Balmer lines for a good fitting result.

**Table A1**  
Parameters AGN-related Continuum Components

Component	Parameter	Range	Fixed/Tied
Power-law cont.	Normalization		
	Extinction $E(B - V)$	[0, 3]	Yes <sup>a</sup>
	Bending wavelength $\lambda_0$	Obs. wavelength range	
	Slope at blue end $\alpha_1$	$-1.76 \pm 0.5$	
	Slope at red end $\alpha_2$	$-0.44 \pm 0.5$	
	Curvature	100	Yes
Balmer cont.	Norm. of continuum part		
	Norm. of blended high-order lines		
	Velocity shift ( $\text{km s}^{-1}$ )	[-1000, 1000]	Yes
	Velocity FWHM ( $\text{km s}^{-1}$ )	[1000, 3000]	Yes
	Extinction $E(B - V)$	[0, 3]	Yes
	Electron temperature (K)	[7500, 30,000]	
	Electron density ( $\text{cm}^{-3}$ )	$10^9$	Yes
	Optical depth at Balmer edge	0	Yes
Fe II cont.	Normalization		
	Velocity shift ( $\text{km s}^{-1}$ )	[-1000, 1000]	
	Velocity FWHM ( $\text{km s}^{-1}$ )	[1000, 3000]	
	Extinction $E(B - V)$	[0, 3]	Yes

**Note.**

<sup>a</sup> “Yes” means that this is not a free parameter, which is fixed to a given value or tied to another parameter in the fitting.

work, we adopt a fixed extinction law from the standard core-mantle diffuse ISM dust model (Jones et al. 2013; Köhler et al. 2014).

In addition to the dust extinction, the other two general parameters for all continuum (except for power-law continuum) and line components are velocity shift ( $v_{\text{off}}$ ) and FWHM. The  $v_{\text{off}}$  and FWHM of emission lines can be directly obtained from the position and width of the Gaussian profile. The  $v_{\text{off}}$  of the continuum components, i.e., MS, SB, Balmer, and iron (pseudo)continua, can also be estimated from the shifting distance relative to systemic redshift. The  $v_{\text{off}}$  of all of the continuum components is set as a free parameter. However, in order to estimate the FWHM of a given continuum component, the template should first be convolved with a Gaussian profile with different width (the convolution is performed in a logarithmic wavelength grid) and then fit with the observed spectrum. Since the convolution is time-consuming, the FWHMs of the continuum components are fixed to their intrinsic value; thus, no convolution is required until the last step. The intrinsic FWHMs of the stellar and iron (pseudo) continua are about 70 (Bruzual & Charlot 2003) and 900 (Vestergaard & Wilkes 2001)  $\text{km s}^{-1}$ , respectively, while for the Balmer continuum and pseudocontinuum, the FWHM is set as 2000  $\text{km s}^{-1}$ , a typical dispersion velocity in the AGN BLR. During the last step, the FWHMs of two stellar continua and iron pseudocontinua are set as free parameters, while the FWHM of the Balmer continuum and pseudocontinuum is tied to the value of the broad Balmer emission lines.

### A.2. Spectral Fitting Processes

The spectral fitting for a given galaxy usually contains tens of free parameters and tens of tied parameters (see Tables A1–A3 for details), which make it impossible to look for the global minimum  $\chi^2$ , where  $\chi^2 = \sum (f_{\text{obs}} - f_{\text{model}})^2 / \sigma_{\text{err}}^2$ , from the entire parameter space. The fast minimization method, e.g., the LM algorithm, which is the core procedure in the QSFIT and

MPFIT packages, is necessary to solve the fitting problem. The modified fitting process can be divided into the following steps.

(1) Preliminary fit with all components enabled. Since the LM algorithm finds only a local minimum, which is not necessarily the global minimum, this feature indicates that the spectral fitting result could significantly depend on the initial values of the parameters. In order to reduce the dependency on the initial parameters, we follow the approach of Calderone et al. (2017) to add (or enable) the continuum and line components step by step—(i) only with power-law and stellar continua, (ii) add Balmer and iron (pseudo)continua, and (iii) add emission lines—and rerun the process at each step. The best-fit results from the last step are transferred into the next step and become proper initial (or guessing) values of existing components in the next step. Finally, all of the continuum and line components discussed above are included in the fitting to obtain the best fit.

(2) Spectral type identification using BLR features. In step (1), all of the components are enabled in the fitting process, while it is not physical in most cases. For example, if the spectrum is HG-dominated, then iron pseudocontinuum is not necessary. Therefore, in this step, we identify the type of each spectrum, i.e., HG- or quasar-dominated, and then update the fitting component set according to the identification results. The quasar-dominated spectra are separated from the HG-dominated spectra using two indicators of AGN BLR features, i.e., the EW of the observed Fe II and Balmer (pseudo)continua and the 80% width of the line profile for permitted lines (H $\beta$  and Mg II). See Section 3.1 for the details of the spectral identification.

If the spectrum is identified as HG-dominated (e.g., Figure A1), the AGN-related continua (power-law, Balmer, and iron) are then disabled in the following steps. If the spectrum is quasar-dominated, in order to reduce the degeneracy between the power-law and SB stellar continua (which can be featureless in the observed wavelength range and similar to the power-law continuum), the SB stellar component

**Table A2**  
Parameters of HG-related Continuum Components

Component	Parameter	Range	Fixed/Tied
MS cont.	Normalization		
	Velocity shift (km s <sup>-1</sup> )	[-500, 500]	
	Velocity FWHM (km s <sup>-1</sup> )	[100, 500]	
	Extinction $E(B - V)$	[0, 3]	
	Maximum stellar age (Myr)	[1000, age of universe]	
	Minimum stellar age (Myr)	0.1	Yes
	Exponential timescale ( $\tau_{\text{SF}}$ , Myr)	1000	Yes
TSB cont.	Normalization		
	Velocity shift (km s <sup>-1</sup> )	[-500, 500]	Yes
	Velocity FWHM (km s <sup>-1</sup> )	[100, 500]	Yes
	Extinction $E(B - V)$	[0, 3]	Yes
	Maximum stellar age (Myr)	[30, 300]	
	Minimum stellar age (Myr)	0.1	Yes
	Exponential timescale ( $\tau_{\text{SF}}$ , Myr)	— <sup>a</sup>	Yes
	Metallicity ( $Z_{\odot}$ )	1	Yes

**Note.**

<sup>a</sup> An SFH with a constant SFR is assumed for TSB.

**Table A3**

Parameters of Emission Line Components

Component	Parameter	Range	Fixed/Tied
Narrow-line	Normalization	— <sup>a</sup>	
	Velocity shift (km s <sup>-1</sup> )	[-500, 500]	— <sup>a</sup>
	Velocity FWHM (km s <sup>-1</sup> )	[100, 1000]	— <sup>a</sup>
	Extinction $E(B - V)$	[0, 3]	— <sup>b</sup>
Broad-line	Normalization	— <sup>a</sup>	
	Velocity shift (km s <sup>-1</sup> )	[-1500, 500]	— <sup>a</sup>
	Velocity FWHM (km s <sup>-1</sup> )	[1000, 3000] <sup>c</sup>	— <sup>a</sup>
	Extinction $E(B - V)$	[0, 3]	— <sup>b</sup>

**Notes.**

<sup>a</sup> The fluxes and velocities of Balmer lines and other doublet emission are tied.

See Section 3.1 and Table A4 for details.

<sup>b</sup> See Table A5 for details.

<sup>c</sup> The upper limit is 10,000 km s<sup>-1</sup> if the spectrum is quasar-identified.

is disabled, while the MS stellar component is kept to represent the contribution of the HG. In addition, in the quasar case, the theoretical line ratios of broad Balmer lines are modified from NLR ( $T_e = 10^4$  K,  $n_e = 100$  cm<sup>-3</sup>) to BLR ( $T_e = 10^4$  K,  $n_e = 10^9$  cm<sup>-3</sup>) conditions, as discussed above. We rerun the process after updating the fitting components to obtain a more physical and reliable fitting result.

(3) Correction for systemic redshift. Based on the fitting result in step (2), we can correct the systemic redshift from the SDSS archived value with the  $v_{\text{off}}$  of the stellar continuum in HG-dominated case or the  $v_{\text{off}}$  of the narrow permitted lines (e.g., H $\alpha$  and H $\beta$ ) in the quasar-dominated case. The fitting process is rerun after the correction; thus, the output shift velocities of all of the components are relative to the updated systemic velocity. Seventeen galaxies show a deviation between the updated and SDSS archived redshifts over 300 km s<sup>-1</sup>, while the median deviation for the entire sample is estimated to be 130 km s<sup>-1</sup>. The median uncertainty of the measurement of the systemic redshift is about 40 km s<sup>-1</sup>.

(4) Convolution of continua. Since the convolution of continua is time-consuming, the FWHMs of the (pseudo)

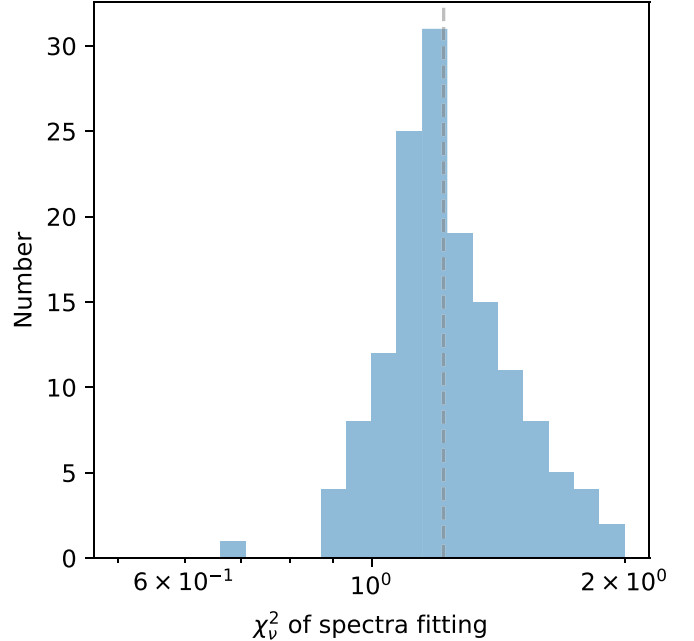


**Figure A2.** Reduced  $\chi^2$  of spectral fitting for AKARI-selected ULIRGs. The vertical dashed line denotes the median  $\chi^2_v$  of 1.2.

continuum components (MS, SB, Balmer, and iron) are fixed in the previous fitting process. During this step, the FWHMs of two stellar continua and the iron pseudocontinuum are set as free parameters with a minimum limit of their intrinsic values, while the FWHM of the Balmer continuum and pseudocontinuum is tied to the value of the broad Balmer emission lines. This is the last step in the fitting process for a given spectrum. The distribution of the reduced  $\chi^2$  for the sample is shown in Figure A2.

(5) Uncertainty estimation with Monte Carlo simulation. We perform the Monte Carlo resampling method to estimate the uncertainties of output results in the fitting process. The method is based on the assumption that the uncertainties on the observed

**Table A4**  
Theoretical Flux Ratios of Emission Lines

Lines	Ratio
Balmer lines <sup>a</sup> (H II or NLR)	0.053: 0.073 : 0.105 : 0.159 : 0.259: 0.468 : 1.000 : 2.863
Balmer lines (BLR)	0.087: 0.109 : 0.142 : 0.198 : 0.297: 0.500 : 1.000 : 2.615
[Ne V] 3346, 3426 Å	1.00 : 2.73
[O II] 3726, 3729 Å	1.00 : 1.36
[Ne III] 3869, 3967 Å	3.32 : 1.00
[O III] 4959, 5007 Å	1.00 : 2.92
[O I] 6300, 6364 Å	3.13 : 1.00
[N II] 6548, 6583 Å	1.00 : 2.94

**Note.**

<sup>a</sup> H10, H9, H8, H7, H $\delta$ , H $\gamma$ , H $\beta$ , H $\alpha$ .

**Table A5**  
Extinction Fit in the Spectral Fitting

Independent Components	Tied Components
Quasar-dominated Spectrum	
Iron pseudocontinuum	Power-law continuum
Broad Balmer lines	Balmer continuum
	Other broad permitted lines
Narrow Balmer lines	All other lines
HG-dominated Spectrum	
MS stellar continuum	SB stellar continuum
Narrow Balmer lines	All other lines <sup>a</sup>
HG-dominated Spectrum, Balmer Lines Are Weak or Not Available	
MS stellar continuum	SB stellar continuum
	All emission lines

**Note.**

<sup>a</sup> Since the broad H $\beta$  or H $\gamma$  in ULIRGs is usually weak, we use the  $E(B - V)$  of narrow Balmer lines to correct for the extinction of the narrow and broad components of all other emission lines.

spectrum are Gaussian-distributed with measurement errors as standard deviations, i.e.,  $f_{\text{observed}} = f_{\text{intrinsic}} + e_{\text{measured}}$ , where  $f_{\text{intrinsic}}$  is the ideal intrinsic spectrum without any uncertainties from the observation. A typical approach is to assume  $f_{\text{intrinsic}} \simeq f_{\text{model}}$ , where  $f_{\text{model}}$  is the best-fit model spectrum, and then generate mock spectra by adding random noise to the model spectrum, i.e.,  $f_{\text{mock}} = f_{\text{model}} + r_{\text{NG}} e_{\text{measured}}$ , where  $r_{\text{NG}}$  is the random noise following a normal Gaussian distribution. However, the assumption of  $f_{\text{intrinsic}} \simeq f_{\text{model}}$  can be effective only if the fitting quality is good within the entire wavelength range; otherwise, the method will make the mock spectra biased to the model spectrum and result in an underestimated uncertainty, for example, a weak broad line but with a relatively high S/N. Therefore, we modified the mock function to

$$\begin{aligned}
 f_{\text{mock}} &= f_{\text{observed}} + r_{\text{NG}} e_{\text{measured}} \\
 &= f_{\text{intrinsic}} + e_{\text{measured}} + r_{\text{NG}} e_{\text{measured}} \\
 &\simeq f_{\text{intrinsic}} + \sqrt{2} e_{\text{measured}}.
 \end{aligned} \tag{A2}$$

In this work, for each observed spectrum, 30 mock spectra are generated using Equation (A2). Similar fitting processes are performed for the mock spectra; finally, for each of the parameters, we obtain a distribution of the best-fit values. The

uncertainty of a given parameter ( $U_p$ ) can be estimated using the standard deviation ( $\sigma$ ) of the distribution of the best-fit values, i.e.,  $U_p \simeq \sigma/\sqrt{2}$ , with the underlying assumption that the scatter of the best-fit values increases by the same number of times (i.e.,  $\sqrt{2}$ ) as the increasing factor of the scatters in the mock spectra.

As discussed above, the fitting procedure is a local  $\chi^2$  minimizer, and the output may significantly depend on the initial values of the parameters. In order to include the systemic errors in the estimated uncertainties of the output parameters, in the fitting process of each mock spectrum, we employ a set of randomized initial values, i.e.,  $p_{\text{init, mock}} = p_{\text{best, real}} + r_{\text{NG}} w_{\text{parameter}}$ , where  $p_{\text{init, mock}}$  and  $p_{\text{best, real}}$  are the initial values of the mock spectrum and the best-fit output of the real spectrum, respectively;  $w_{\text{parameter}}$  is the width of the parameter range.<sup>30,31</sup>

## Appendix B Details of the Multiband SED Decomposition

### B.1. Dust Absorbers and Emitters in HGs

A widely adopted strategy of multiband SED decomposition is the so-called ‘‘energy balance,’’ which requires conservation between the attenuated primary radiation from stars and/or AGNs and the reemitted emission by the dust surrounding the primary emitters.

We first consider the dust absorption and reemission in HGs. The real conditions and properties of dust in the galaxies can be very complicated (e.g., Galliano et al. 2008, 2018). In the fitting procedure, we employ a modified two-component model presented by Charlot & Fall (2000, hereafter CF2000). The CF2000 model provides a simple and brief scenario in which the young stars are embedded in their birth clouds during a finite timescale (e.g.,  $t_{\text{BC}}$ ). The birth clouds are dispersed by strong stellar self-winds or winds due to nearby supernova explosions after  $t_{\text{BC}}$ , and then the young stars are exposed to the diffuse ISM dust. Therefore, the emission of young stars is absorbed by their natal clouds at  $t < t_{\text{BC}}$  and the diffuse ISM dust at  $t > t_{\text{BC}}$ , while the old stars are only attenuated by diffuse ISM.

In the spectral fitting (Appendix A), we tie the extinction of the SB component to the value of the MS component. Within the scenario of the CF2000 model, the optically observed SB components represent the young stars for which the natal clouds have been destroyed and migrate to the diffuse ISM dust. For the sake of simplicity, hereafter, we refer to the young stellar population embedded in optically thin diffuse ISM as the TSB component and the young stars that are almost fully absorbed by optically thick natal clouds as the ASB component. Under the framework of the CF2000 model, the ASB and TSB components are separated by a certain timescale,  $t_{\text{BC}}$ . The timescale  $t_{\text{BC}}$  is considered to be from 10 Myr for normal star-forming galaxies to 100 Myr for ULIRGs (da Cunha et al. 2008, 2010), which is similar to the range of age of SB components in our spectral fitting procedure. In this work, we employ another, partly different scenario, that the ASB and TSB components are not separated by  $t_{\text{BC}}$  but have a similar age. A possible explanation for the modified scenario is that the

<sup>30</sup> If the generated  $p_{\text{init, mock}}$  exceeds the parameter range, then  $p_{\text{init, mock}}$  is taken as the maximum/minimum of the parameter range.

<sup>31</sup> If the parameter is a normalization with a range of  $p \geq 0$ , then we employ  $w_{\text{parameter}} = p_{\text{best, real}}$ .

natal clouds are not fully isotropic. The SF radiation could be observed as TSB components in the directions where the UV-optical light is allowed to intersect the clouds to freely stream away into the diffuse ISM regions; or observed as ASB components in the other directions where the stellar light is fully attenuated by dust. (e.g., Popescu et al. 2011). Within this scenario, we can assume the ASB component has the same stellar population as the TSB component, except for extinctions. The extinction estimated from optical spectral fitting can be used for the MS and TSB components that are embedded in optically thin diffuse ISM. The birth clouds in star-forming regions (e.g., giant molecular clouds) can have heavy extinction ( $A_V \sim 50\text{--}150$ ; Reipurth & Schneider 2008). Using the  $9.7\ \mu\text{m}$  silicate features, da Cunha et al. (2010) estimated the optical depths for 16 local ULIRGs with  $\tau_V \sim 30\text{--}40$ . In this work, we assume  $A_V = 100$  for the ASB component for all galaxies, which corresponds to a typical dense collapsing cloud with a spatial scale of 0.2 pc,  $n_{\text{H}_2} = 2 \times 10^5\ \text{cm}^{-3}$ , and a V-band opacity of  $3 \times 10^3\ \text{m}^2\ \text{Kg}^{-1}$  (Shu et al. 1987).

The distribution of starlight intensities needs to be assumed to model the dust radiation. The diffuse ISM dust is usually considered to be exposed in ambient starlight with a constant intensity. The heating for dust in the birth cloud is considered to be dominated by its stellar progeny. In the literature, the dust in the region with an intense radiation field (so-called ‘‘PDR’’ components) is usually described using a power law–distributed starlight intensity, i.e.,  $dM/dU \propto U^{-\alpha}$  (Dale & Helou 2002; Draine & Li 2007; Dale et al. 2014). Suggesting that the dust surrounding the star follows  $\rho \propto r^{-\beta}$ , the two parameters  $\alpha$  and  $\beta$  are correlated as  $\alpha \simeq (5 - \beta)/2$  in a moderate extinction condition, indicating that dust with a more concentrated distribution is exposed to a greater heating intensity and heated to a higher temperature when it is in thermal equilibrium with the radiation field.

A detailed ISM dust model is required to reproduce the observed IR SED, which depends on a series of dust properties, e.g., the abundance of carbon, silicate, and other elements; the compositions and structures of dust particles (e.g., crystalline, amorphous, etc.); the distribution of sizes of dust grains; and so on. In this work, we employ the THEMIS model, which is based on the optical properties of amorphous hydrocarbon and silicate materials measured in the laboratory (Jones et al. 2013; Köhler et al. 2014). The dust extinction curve and radiation SED in the THEMIS model are calculated with the `DustEM` codes using the interstellar radiation field (ISRF; Mathis et al. 1983). We take the updated version presented by Nersesian et al. (2019), in which the model is mainly described with five parameters: (1) the mass fraction of small aromatic feature emitting grains,  $q_{\text{HAC}}$ ; (2) the average heating intensity for diffuse ISM dust,  $\langle U \rangle$ ; (3) the minimum and (4) maximum heating intensity, i.e.,  $U_{\text{min}}$  and  $U_{\text{max}}$ ; and (5) the power-law slope for dust in birth clouds,  $\alpha$ . Here  $q_{\text{HAC}}$  controls the intensity of the line features in the MIR range ( $3\text{--}20\ \mu\text{m}$ ). In the fitting process, we take the range of  $q_{\text{HAC}}$  from the minimum value in the THEMIS model, i.e., 0.02, to the value of the Milky Way, i.e., 0.17, with an additional extended lower limit of 0.005 to represent the extreme region where the small dust grains are destroyed by a strong radiation field, e.g., close to an O/B star (Galliano et al. 2018). With the THEMIS model, the dust temperature can be approximately estimated from the intensity of the radiation field (Nersesian et al. 2019), i.e.,  $T_{\text{dust}} = 18.3 U^{1/5.79}$ , where  $T_{\text{dust}}$  and  $U$  are in units of K and intensity of the ISRF, respectively. Following Draine & Li (2007)

and Nersesian et al. (2019), we assume  $U_{\text{min}} = \langle U \rangle$ , which represents a smooth temperature transition from the external layer of birth clouds to diffuse ISM dust. We also assume the diffuse ISM dust heated by the MS and TSB components has the same  $U_{\text{min}}$ , because in practice, they are hard to distinguish. The value of  $U_{\text{min}}$  is constrained in the range of [2, 80], which corresponds to the temperature range of [20, 40] K. For the galaxies with only one or two photometric detections in the FIR range ( $>50\ \mu\text{m}$ ), we only test four temperatures: the typical temperatures of elliptical and star-forming galaxies, 30 K ( $U = 17$ ) and 25 K ( $U = 7$ ), respectively (Nersesian et al. 2019), and the two typical temperature of ULIRGs, 35 K ( $U = 40$ ) and 40 K ( $U = 80$ ; da Cunha et al. 2010). The  $U_{\text{max}}$  in the model is fixed to  $10^7$ , corresponding to a temperature of about 300 K and a distance of 7 au to a massive star of  $10 L_{\odot}$ . The heating intensity power-law slope  $\alpha$  is taken from three values, i.e., 2, 2.5, and 3, which corresponds to the mass density index of 1, 0, and  $-1$  with the approximate relationship  $\alpha = (5 - \beta)/2$  assuming mass density follows  $\rho = K_{\rho} r^{-\beta}$ . Here  $\beta = 1$  indicates that the dust concentrated at the center of the birth clouds, representing the early phase of SF when the star just formed in the center of the collapsing natal cloud, whereas  $\beta = -1$  suggests that the majority of the dust locates at the outer region, representing the late phase when the natal cloud is blown out by the stellar wind. In summary, in our SED fitting process, the dust surrounding stars can be described by three parameters:  $q_{\text{HAC}}$ ,  $U_{\text{min}}$  (or  $\langle U \rangle$ ), and  $\alpha$ .

## B.2. MIR Radiation from AGN Torus

In addition to the dust surrounding stars, the AGN can also contribute to the IR SED of a galaxy by thermal emission from a thick layer of dust surrounding an accretion disk. The UV–optical radiation from the accretion disk is absorbed by the torus and then reemitted as torus thermal radiation. Since the inner radius of the dusty torus can reach a 0.5–1 pc scale, the dust can be heated up to the sublimation temperature, e.g., 1000–1500 K, which is much higher than the typical temperature of star-heated dust, e.g.,  $\sim 100$  K in PDR or 20–40 K in star-forming regions. The torus with a much higher temperature shows a significant MIR excess, peaking at  $\sim 3\ \mu\text{m}$ , in the SED of the galaxy. Therefore, the MIR torus feature is widely used to identify the AGN activity in galaxies (e.g., Ciesla et al. 2015; Małek et al. 2017).

In this work, we employ the SKIRTor torus model developed by Stalevski et al. (2012) and updated in Stalevski et al. (2016) with the 3D Monte Carlo radiative transfer code `SKIRT` (Baes et al. 2003, 2011). The SKIRTor model consists of a two-phase medium, i.e., a large number of high-density clumps embedded in a smooth dusty component of low-density grains. Compared to the pure smooth or clumpy torus model, the SKIRTor with a two-phase medium can produce attenuated silicate features and a pronounced NIR emission at the same time. In the current SED library, the fraction of total dust mass inside clumps is fixed to 0.97, corresponding to a volume filling factor of 0.25. The clumpy and smooth dust grains are spatially distributed with density following  $\rho(r, \theta) \propto r^{-p} e^{-q|\cos\theta|}$ , where  $r$  and  $\theta$  are the radius and angle in the polar coordinate system. The value of  $r$  is limited by the inner and outer radius, i.e.,  $R_{\text{in}}$  and  $R_{\text{out}}$ . The model is assumed to be scaled with the AGN bolometric luminosity, and the radial scale of the torus is described using the radius ratio  $R_{\text{out}}/R_{\text{in}}$ . A larger  $R_{\text{out}}/R_{\text{in}}$  corresponds to a torus with cooler dust, i.e., an SED with peak at a longer wavelength. The polar angle  $\theta$  of the torus is limited by the half-opening angle  $\Theta$ , which is related to the covering factor of the torus,

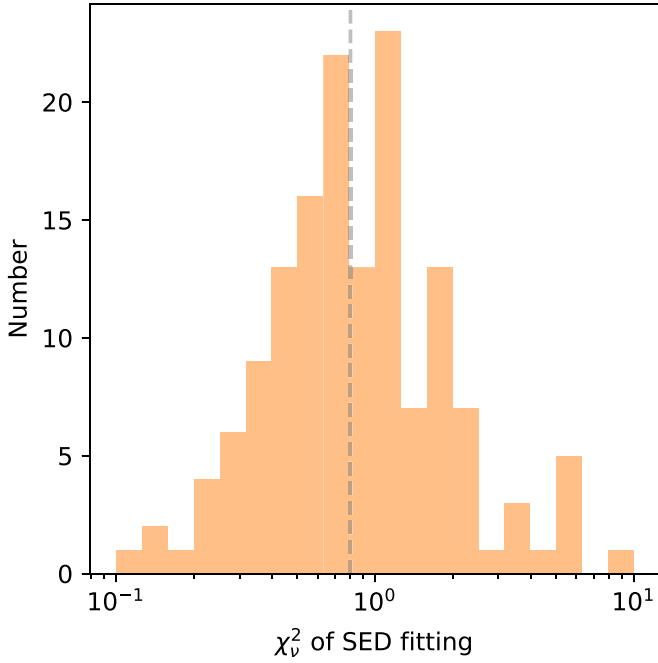


**Figure B1.** Reduced  $\chi_v^2$  of the SED decomposition. The vertical dashed line denotes the median  $\chi_v^2$  of 0.8.

$\text{CF} = \sin\Theta$ . The amount of dust of the torus is described using the  $9.7 \mu\text{m}$  optical depth in the equatorial direction, i.e.,  $\tau_{9.7}$ .

Within the framework of the SKIRTor model, not only the dusty torus but also the primary central source is anisotropic, with the flux following  $F(\theta) \propto \cos\theta(1 + 2\cos\theta) \sim \cos\theta$ . It is a more reasonable assumption to describe a disklike heating source compared to the other torus model with an isotropic pointlike central source. The primary source follows a commonly adopted multislope bending power-law SED (Schartmann et al. 2005). The anisotropic torus is the fundamental scenario for the AGN unified scheme. If the inclination  $\varphi$  follows  $\varphi + \Theta \leq \pi/2$ , the primary source is blocked in the line of sight, and the AGN is in type 2 geometry; otherwise, the central radiation freely streams away, and the AGN is in type 1 geometry.

Except for the fixed clumpy fraction, there are six parameters in the SKIRTor model. As explained in Section 3.1, in this work, we focus on type 2 AGNs (for which the optical spectrum is dominated by a galaxy component); therefore, we only take  $\varphi + \Theta \leq \pi/2$ . Recently, a study of X-ray-selected AGNs reported that the typical covering factor is about 0.6 (Stalevski et al. 2016; Mateos et al. 2017; Ichikawa et al. 2019), which corresponds to  $\Theta \sim 30^\circ$ . Due to the degeneracy between  $\varphi$  and  $\Theta$  and the limited number of data points, it is a proper choice to fix it to the typical value from the literature, i.e.,  $30^\circ$ . Thus, the inclination  $\varphi$  is constrained in the range of  $[60^\circ, 70^\circ, 80^\circ, 90^\circ]$ . We also fix the spatial distribution to one case with  $p = 1$  and  $q = 0.5$  and then take the full available range of  $R_{\text{out}}/R_{\text{in}}$ , i.e.,  $[10, 20, 30]$ , and the extinction  $\tau_{9.7}$ , i.e.,  $[3, 5, 7, 9, 11]$ .

Note that even though we only focus on type 2 AGNs with  $\varphi + \Theta \leq \pi/2$ , the primary radiation of the accretion disk is not fully extinct. A part of the radiation of the accretion disk could penetrate the dusty torus, and the fraction of the penetrating radiation depends on the inclination, the amount of the

extinction, and the spatial distribution of the dust. Since the penetrating component extends from MIR to NIR and optical bands, it is necessary to evaluate whether it significantly affects the fitting of the optical spectrum or not. In the SEDs (torus + accretion disk) used in this work, the one with  $\tau_{9.7} = 11$  and  $\varphi = 60^\circ$  shows the bluest optical–IR color, i.e., the largest contribution to the optical bands, and a flux density ratio of  $S_{3.4\mu\text{m}}/S_{0.8\mu\text{m}} \sim 100$ , in which the wavelengths are taken as the central wavelength of the WISE W1 band and SDSS  $i$  band, respectively. On the other hand, for the 149 ULIRGs with galaxy-dominated optical spectra, the average flux ratio  $F_{\text{W1}}/F_i$  is  $3.8 \pm 4.7$ . The result suggests that even the bluest SED in the template is still much redder than the observed SED in the optical–NIR bands; therefore, the contamination of the penetrating component in the optical spectrum could be ignored.

### B.3. Connection from Optical Spectral Fitting to SED Decomposition

In order to connect the spectral fitting results to the SED fitting process, we consider the energy conservation in each emitter–absorber system and the entire galaxy. The equations that represent the energy balance in the dust surrounding stars are listed in Equation (B1),

$$\frac{\int_{912\text{\AA}}^{1\text{mm}} S_{\text{MS}}^{\text{sp}} [1 - 10^{-0.4(\tau_\lambda/\tau_V)A_{\text{V,MS}}^{\text{sp}}}] d\lambda}{\int_{100\text{\AA}}^{1\text{mm}} S_{\text{MS}}^{\text{sp}} d\lambda} = \frac{L_{\text{ISM,MS}}}{L_{\text{MS}}} = \frac{L_{\text{ISM,MS}}}{C_{\text{ape,MS}} L_{\text{MS}}^{\text{sp}}},$$

$$\frac{\int_{912\text{\AA}}^{1\text{mm}} S_{\text{TSB}}^{\text{sp}} [1 - 10^{-0.4(\tau_\lambda/\tau_V)A_{\text{V,TSB}}^{\text{sp}}}] d\lambda}{\int_{100\text{\AA}}^{1\text{mm}} S_{\text{TSB}}^{\text{sp}} d\lambda} = \frac{L_{\text{ISM,TSB}}}{L_{\text{TSB}}} = \frac{L_{\text{ISM,TSB}}}{C_{\text{ape,TSB}} L_{\text{TSB}}^{\text{sp}}},$$

$$\frac{\int_{912\text{\AA}}^{1\text{mm}} S_{\text{ASB}}^{\text{sp}} [1 - 10^{-0.4(\tau_\lambda/\tau_V)A_{\text{V,ASB}}^{\text{sp}}}] d\lambda}{\int_{100\text{\AA}}^{1\text{mm}} S_{\text{ASB}}^{\text{sp}} d\lambda} = \frac{L_{\text{ISM,ASB}}}{L_{\text{ASB}}}, \quad (\text{B1})$$

where  $S_{\text{MS}}^{\text{sp}}$  means the intrinsic stellar spectrum of MS stars,  $A_{\text{V,MS}}^{\text{sp}}$  means the extinction of diffuse ISM dust around MS stars, and  $L_{\text{MS}}$  and  $L_{\text{ISM,MS}}$  denote the total luminosity for the MS population and the dust heated by MS stars. Similar variables are defined for the TSB and ASB components and the dust around them. All variables with an “sp” suffix suggest that the spectra and values are taken from the spectral fitting results; e.g.,  $S_{\text{MS}}^{\text{sp}}$  is the best-fit continuum for the MS components in the spectral fitting results. Note that two factors, i.e.,  $C_{\text{ape,MS}}$  and  $C_{\text{ape,TSB}}$ , are employed to correct for the aperture loss of the SDSS fibers. We allow the MS and TSB components to have different correctors. Here  $\tau_\lambda$  denotes the extinction (opacity) curve used in the SED fitting, which is the same one used in the spectral fitting. In order to build a self-consistent method, we adopt the extinction curve derived from the THEMIS dust model, which is used to reproduce the dust emission in the SED

fitting process. Note that in the integration of absorbed luminosity by dust, we set a lower limit of wavelength 912 Å, with an underlying assumption that most of the photons with energy higher than 13.6 eV are absorbed by the photoionization process of hydrogen and helium gas in the H II region, rather than attenuated by the dust (Draine & Li 2007). As explained in Section B.1, within the variables in Equation (B1), we assume  $A_{V,TSB}^{sp} = A_{V,MS}^{sp}$  and  $A_{V,ASB} = 100$ ;  $S_{ASB}^{sp} = S_{TSB}^{sp}$ , and thus the ASB component has the same intrinsic spectrum as the TSB components. Only three variables, i.e.,  $C_{ape,MS}$ ,  $C_{ape,TSB}$ , and  $L_{ASB}$ , are the independent parameters that will be estimated in the fitting process.

As for the energy conservation of AGN and torus radiation, we directly adopt the result in the SKIRTor model, which is calculated by a radiation transfer program. A similar equation can be explained as Equation (B2). Note that since both of the primary and dust SEDs are anisotropic, they are shown in flux units in the equation:

$$\frac{\int_{\Omega_{\text{torus}}} \int_{912\text{\AA}}^{1\text{mm}} F_{\text{AD}} [1 - 10^{-0.4(\tau_{\lambda}/\tau_V)A_{V,\text{Tor}}} ] d\lambda d\omega}{\int_{4\pi} \int_{100\text{\AA}}^{1\text{mm}} F_{\text{AD}} d\lambda d\omega} = \frac{\int_{4\pi} \int_{100\text{\AA}}^{1\text{mm}} F_{\text{torus}} d\lambda d\omega}{L_{\text{AGN}}/D_L(z)^2}. \quad (\text{B2})$$

For the SED model with parameters of given values, the expected fluxes in each band can be calculated by convolving the model SED  $S_{\text{comp}}$  with the transmission curve of each band  $T_{\text{band}}$ ,

$$F_{\text{band}}^{\text{mod}} = \Sigma_{\text{comp}} \frac{L_{\text{comp}}}{4\pi D_L^2(z)} \frac{\int S_{\text{comp}}(z) T_{\text{band}} d\lambda}{\int S_{\text{comp}}(z) d\lambda \int T_{\text{band}} c/\lambda^2 d\lambda}, \quad (\text{B3})$$

and the best-fit SED parameters (e.g.,  $q_{\text{HAC}}$ ) and the normalizations,  $L_{\text{comp}}$  (e.g.,  $L_{\text{AGN}}$ ), can be obtained by minimizing  $\chi^2 = (F_{\text{band}}^{\text{obs}} - F_{\text{band}}^{\text{mod}})^2 / \sigma_{\text{band}}^{\text{obs}2}$ , where  $F_{\text{band}}^{\text{obs}}$  and  $\sigma_{\text{band}}^{\text{obs}}$  are the observed fluxes and their measurement errors. All of the primary radiation components, i.e., MS, TSB, ASB, and AGN (accretion disk), and the dust reemitted components, i.e., ISM heated by MS and TSB, BC heated by ASB, and torus heated by AGNs, are included in the calculation. In order to reproduce the contribution of emission lines to the broadband photometry in the optical bands, we also include the optical emission line spectrum from the decomposition of the observed spectrum (Section 3.1) in Equation (B3). The emission line spectrum is corrected for aperture loss using the average of  $C_{ape,MS}$  and  $C_{ape,TSB}$ . The four outputs directly from Equation (B3) are two aperture correction factors ( $C_{ape,MS}$  and  $C_{ape,TSB}$ ), the total luminosity of the primary radiation of the ASB component ( $L_{\text{ASB}}$ ), and the AGN accretion disk ( $L_{\text{AGN}}$ ). The inputs and outputs of the SED decomposition are summarized in Table C1. The distribution of the  $\chi^2_{\nu}$  is shown in Figure B1, with a median reduced  $\chi^2$  of 0.8.

For each ULIRG, 100 mock photometric observations are generated by adding the random noise to the observed fluxes. The random noise is Gaussian-distributed with the amplitude from the measurement error in each band. The same fitting processes are employed for the mock photometric data, and the

**Table C1**  
Summary of the Variables in the SED Decomposition Equation

Components	Parameters
	Input (from Spectral Fitting)
HG	$S_{\text{MS}}^{\text{sp}}, S_{\text{TSB}}^{\text{sp}}, a, A_{V,MS}^{\text{sp}}, b, L_{\text{MS}}^{\text{sp}}, L_{\text{TSB}}^{\text{sp}}$
	Input (Parameters of Undetermined SED)
HG	$q_{\text{HAC}}, U_{\text{min}}, \alpha$
AGN	$\varphi, R_{\text{out}}/R_{\text{in}}, \tau_{7.9}$
	Output (Directly from Equation (B3))
HG	$C_{ape,MS}, C_{ape,TSB}, L_{\text{ASB}}$
AGN	$L_{\text{AGN}}$

**Notes.**

<sup>a</sup> Same for  $S_{\text{ASB}}^{\text{sp}}$ .

<sup>b</sup> Same for  $A_{V,TSB}^{\text{sp}}$ ; we assume  $A_{V,ASB} = 100$ .

scatters of the best-fit values are taken as the uncertainties of the parameters.

## Appendix C

### Possible Effect of the Galactic-scale Dust Heated by AGNs

An underlying assumption of the typical SED decomposition method for galaxies is that the dust heated by stellar light dominates the bulk of the observed FIR radiation, and the AGN dusty torus mainly contributes to the MIR excess due to a higher dust temperature (e.g., Section 3.2; see also Ciesla et al. 2015; Małek et al. 2017). However, an equatorial optically thick torus is only a first-order approximation of the circumnuclear dust environment around AGNs, and the dust can also exist in the polar direction, i.e., the direction perpendicular to the equatorial plane of the torus (e.g., Lyu & Rieke 2018). The dust emission in the polar direction is supported by recent high spatial resolution MIR observations (Asmus et al. 2016; Asmus 2019; Fuller et al. 2019). The polar dust can also contribute to the FIR emission if it extends to a large scale ( $\sim 10^2 - 10^3$  pc). Dust models combining the torus and polar dust with sophisticated geometry have been developed using radiation transfer codes to explain the observed interferometric image (e.g., Hönig & Kishimoto 2017; Stalevski et al. 2017). The best-fit geometry usually depends on the particular observational constraints for individual AGNs. Here we introduce a simpler method to model the AGN-heated dust at a large scale to quickly test the possible effect of the additional dust component on the analysis of the evolution of ULIRGs. Since at a large distance, the dust can be assumed to be heated by a pointlike radiation source, we consider that the polar dust component follows a scaled PDR-like structure (Appendix B.1), and the energy conservation between the absorption and the reemitted thermal radiation can be calculated as

$$\frac{\int_{912\text{\AA}}^{1\text{mm}} F_{\text{AD}}(i=0) [1 - 10^{-0.4(\tau_{\lambda}/\tau_V)A_{V,\text{Pol}}} ] d\lambda}{\int_{100\text{\AA}}^{1\text{mm}} F_{\text{AD}}(i=0) d\lambda} = \frac{L_{\text{polar}}}{L_{\text{AGN}}} \left( 1 - \left( \frac{\Omega_{\text{torus}}}{4\pi} \right)^2 \right)^{-1}, \quad (\text{C1})$$

where  $F_{\text{AD}}(i=0)$  denotes the assumed SED of the AGN accretion disk in the polar direction,  $\tau_{\lambda}/\tau_V$  and  $A_{V,\text{Pol}}$  are the

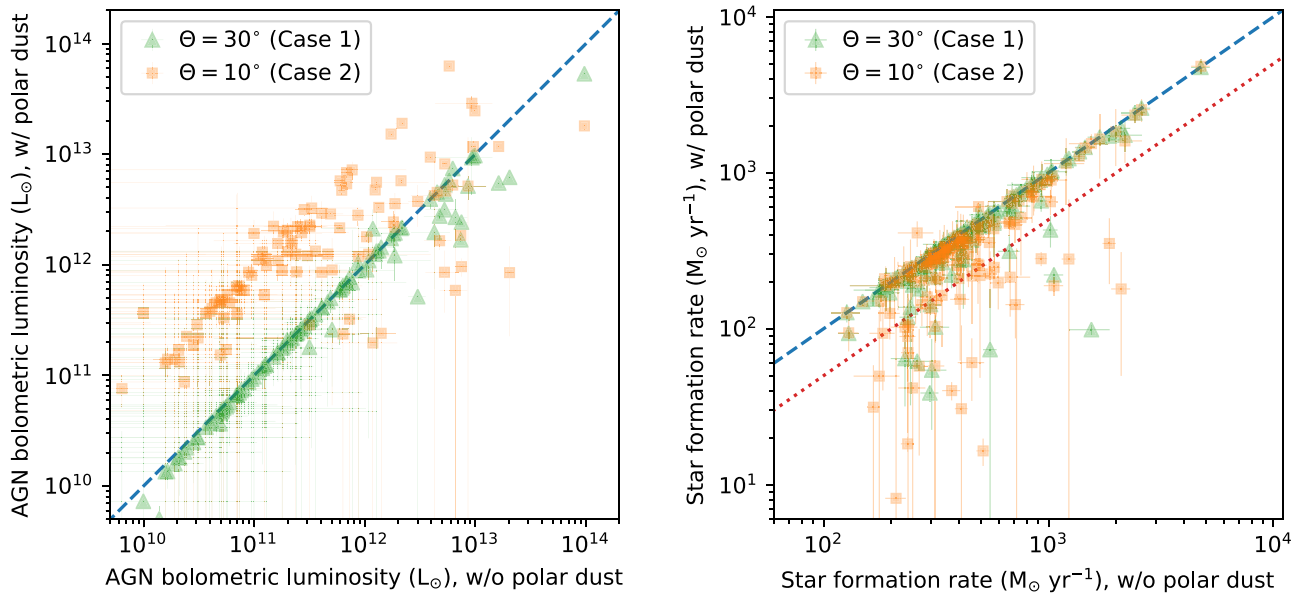


**Figure C1.** Left: comparison between AGN bolometric luminosity ( $L_{\text{AGN}}$ ) estimated with (y-axis) and without (x-axis) the polar dust component. The green triangles and orange squares denote the results with  $\Theta = 30^\circ$  and  $10^\circ$ , respectively, where  $\Theta$  is the half-opening angle of the torus. The blue dashed line shows the 1:1 ratio position. Right: comparison between SFR estimated with (y-axis) and without (x-axis) the polar dust component. The symbols are the same as in the left panel. The red dotted line denotes the 2:1 ratio position; e.g., the estimated SFR decreases by 50% with the polar dust component.

dust opacity and extinction in the polar direction,  $L_{\text{polar}}$  and  $L_{\text{AGN}}$  denote the luminosity of the polar dust and the bolometric luminosity of the AGN, and  $\Omega_{\text{torus}}/4\pi$  is the covering factor of the torus, which is related to the half-opening angle ( $\Theta$ ) by  $\Omega_{\text{torus}}/4\pi = \sin \Theta$ . The polar dust is assumed to be isotropic, but only the dust directly facing the AGN, i.e., in the direction that is not covered by the torus, is included in the energy conservation equation. We neglect the contribution from scattered light. The component is considered to be optically thin, and the extinction measured from the optical stellar continuum is assumed for the polar dust, i.e.,  $A_{\text{V,pol}} = A_{\text{V,MS}}$ . Following the diffuse interstellar dust, we still employ the THEMIS dust model and its opacity in the calculation. The inner edge of the polar dust is fixed using  $U = 10^7$ , which is similar to the sublimation radius of the torus. We assume the dust at the outer edge has the same temperature as the ISM dust; thus, the outer radius of the polar dust can be parameterized using the average heating intensity in the ISM region. For an AGN with  $L_{\text{AGN}} = 10^{11} L_{\odot}$  and an outer dust temperature of 30 K, the inner and outer radii of the polar dust are approximately 3 pc and 2 kpc, respectively. For simplicity, we only consider two cases with fixed torus opening angles  $\Theta = 30^\circ$  (hereafter case 1) and  $\Theta = 10^\circ$  (hereafter case 2). The half-opening angle in case 1 is the same as that in the previously discussed default case without polar dust (hereafter case 0). A smaller  $\Theta$  in case 2 means that the AGN can eject more energy into the polar dust, i.e., contribute more FIR radiation.

The two panels in Figure C1 show the  $L_{\text{AGN}}$  and SFR estimated from the SED decompositions with the polar dust component and the comparison to the results in the default case without polar dust. The  $L_{\text{AGN}}$  from case 1 is nearly the same as the  $L_{\text{AGN}}$  from case 0, because the  $L_{\text{AGN}}$  is limited by the MIR torus emission, and the same  $\Theta = 30^\circ$  corresponds to (almost) the same  $L_{\text{AGN}}-L_{\text{torus}}$  correlation ( $L_{\text{AGN}}$  and  $L_{\text{torus}}$  are the

bolometric luminosity of the AGN (accretion disk) and the luminosity of the torus). In case 2,  $\Theta = 10^\circ$  suggests a smaller energy conversion fraction from AGN to torus and yields a 10 times higher  $L_{\text{AGN}}$ . The average energy conversion fractions of the polar dust ( $f_{\text{polar}} = L_{\text{polar}}/L_{\text{AGN}}$ ) for cases 1 and 2 are  $0.23 \pm 0.05$  and  $0.28 \pm 0.05$ , respectively. The average energy conversion fractions of the torus dust ( $f_{\text{torus}} = L_{\text{torus}}/L_{\text{AGN}}$ ) for cases 1 and 2 are  $0.21 \pm 0.01$  and  $0.03 \pm 0.01$ , respectively.

Since the radiation of polar dust is assumed extend to the FIR wavelength range, the SFR from the SED decomposition with polar dust can be reduced. For simplicity, we define the reduced ratio as  $f_{\text{SFR,red}} = 1 - \text{SFR}_{\text{with polar}}/\text{SFR}_{\text{no polar}}$ . In case 1, 11 out of the 149 ULIRGs show  $f_{\text{SFR,red}} > 50\%$ , while 114 ULIRGs show  $f_{\text{SFR,red}} < 10\%$ , indicating that with a torus of  $\Theta = 30^\circ$ , the effect of polar dust on the estimation of SFR is small for most of the galaxies. However, in case 2, 33 ULIRGs show  $f_{\text{SFR,red}} > 50\%$ , in which six galaxies even show  $f_{\text{SFR,red}} > 90\%$ , which is due to the much cooler and redder AGN dust SED ( $L_{\text{polar}}/L_{\text{torus}} \sim 9$ ; for comparison, the ratio for case 1 is  $\sim 1$ ).

The high  $f_{\text{SFR,red}}$  in case 2 could suggest a quenching pattern; i.e., the SFR decreases as the AGN becomes luminous, which we do not find in the default analysis. The quenching correlation should be treated with caution, since the result is highly dependent on the assumption of the model, e.g., the distribution and extinction of the polar dust component. Since the merger can trigger massive inflows of gas and dust into the nuclear region, the highly obscured AGN embedded in the galactic-scale dusty environment could exist in some cases, e.g., hot dust-obscured-galaxies (hot DOGs; Lyu & Rieke 2018). The possible effect of the AGN on large-scale dust indicates that considerable uncertainties remain in the study of ULIRG evolution. A submillimeter observation, e.g., the Atacama Large Millimeter/submillimeter Array, directly determining the dust emission distribution around the AGN is required to address the question.

## ORCID iDs

Xiaoyang Chen  <https://orcid.org/0000-0003-2682-473X>  
 Masayuki Akiyama  <https://orcid.org/0000-0002-2651-1701>  
 Kohei Ichikawa  <https://orcid.org/0000-0002-4377-903X>  
 Yoshiki Toba  <https://orcid.org/0000-0002-3531-7863>  
 Toshihiro Kawaguchi  <https://orcid.org/0000-0002-3866-9645>  
 Abdurro' UF  <https://orcid.org/0000-0002-5258-8761>  
 Mitsuru Kokubo  <https://orcid.org/0000-0001-6402-1415>

## References

- Aguado, D. S., Ahumada, R., Almeida, A., et al. 2019, *ApJS*, **240**, 23  
 Akiyama, M., Minowa, Y., Kobayashi, N., Ohta, K., Ando, M., & Iwata, I. 2008, *ApJS*, **175**, 1  
 Arribas, S., Colina, L., Bellocchi, E., Maiolino, R., & Villar-Martín, M. 2014, *A&A*, **568**, A14  
 Asmus, D. 2019, *MNRAS*, **489**, 2177  
 Asmus, D., Hönig, S. F., & Gandhi, P. 2016, *ApJ*, **822**, 109  
 Assef, R. J., Stern, D., Noirot, G., et al. 2018, *ApJS*, **234**, 23  
 Baes, M., Davies, J. I., Dejonghe, H., et al. 2003, *MNRAS*, **343**, 1081  
 Baes, M., Verstappen, J., De Looze, I., et al. 2011, *ApJS*, **196**, 22  
 Baldwin, J. A., Phillips, M. M., & Terlevich, R. 1981, *PASP*, **93**, 5  
 Berney, S., Koss, M., Trakhtenbrot, B., et al. 2015, *MNRAS*, **454**, 3622  
 Boquien, M., Burgarella, D., Roehly, Y., et al. 2019, *A&A*, **622**, A103  
 Boroson, T. A., & Green, R. F. 1992, *ApJS*, **80**, 109  
 Bridge, C. R., Appleton, P. N., Conselice, C. J., et al. 2007, *ApJ*, **659**, 931  
 Brinchmann, J., Charlot, S., White, S. D. M., et al. 2004, *MNRAS*, **351**, 1151  
 Bruzual, G., & Charlot, S. 2003, *MNRAS*, **344**, 1000  
 Calderone, G., Nicastro, L., Ghisellini, G., Dotti, M., Sbarrato, T., Shankar, F., & Colpi, M. 2017, *MNRAS*, **472**, 4051  
 Calzetti, D., Armus, L., Bohlin, R. C., et al. 2000, *ApJ*, **533**, 682  
 Cappellari, M. 2012, pPXF: Penalized Pixel-Fitting Stellar Kinematics Extraction  
 Cardelli, J. A., Clayton, G. C., & Mathis, J. S. 1989, *ApJ*, **345**, 245  
 Casey, C. M., Narayanan, D., & Cooray, A. 2014, *PhR*, **541**, 45  
 Charlot, S., & Fall, S. M. 2000, *ApJ*, **539**, 718  
 Chen, X., Akiyama, M., Noda, H., et al. 2019, *PASJ*, **71**, 29  
 Ciesla, L., Charmandaris, V., Georgakakis, A., et al. 2015, *A&A*, **576**, A10  
 Compiègne, M., Verstraete, L., Jones, A., et al. 2011, *A&A*, **525**, A103  
 Cutri, R. M., et al. 2014, *ycat*, **2328**, 0  
 da Cunha, E., Charlot, S., & Elbaz, D. 2008, *MNRAS*, **388**, 1595  
 da Cunha, E., Charmandaris, V., Diaz-Santos, T., et al. 2010, *A&A*, **523**, A78  
 Dale, D. A., & Helou, G. 2002, *ApJ*, **576**, 159  
 Dale, D. A., Helou, G., Magdis, G. E., et al. 2014, *ApJ*, **784**, 83  
 Dasyra, K. M., Tacconi, L. J., Davies, R. I., et al. 2006, *ApJ*, **638**, 745  
 Di Matteo, T., Springel, V., & Hernquist, L. 2005, *Natur*, **433**, 604  
 Dietrich, M., Peterson, B. M., Grier, C. J., et al. 2012, *ApJ*, **757**, 53  
 Draine, B. T., & Li, A. 2007, *ApJ*, **657**, 810  
 Elvis, M., Willner, S. P., Fabbiano, G., et al. 1984, *ApJ*, **280**, 574  
 Feigelson, E. D., & Nelson, P. I. 1985, *ApJ*, **293**, 192  
 Finkbeiner, D. P., Schlafly, E. F., Schlegel, D. J., et al. 2016, *ApJ*, **822**, 66  
 Fiore, F., Feruglio, C., Shankar, F., et al. 2017, *A&A*, **601**, A143  
 Fitzpatrick, E. L. 1999, *PASP*, **111**, 63  
 Fuller, L., Lopez-Rodriguez, E., Packham, C., et al. 2019, *MNRAS*, **483**, 3404  
 Galliano, F., Galametz, M., & Jones, A. P. 2018, *ARA&A*, **56**, 673  
 Galliano, F., Madden, S. C., Tielens, A. G. G. M., Peeters, E., & Jones, A. P. 2008, *ApJ*, **679**, 310  
 Glikman, E., Helfand, D. J., White, R. L., et al. 2007, *ApJ*, **667**, 673  
 Goto, T., Arnouts, S., Malkan, M., et al. 2011, *MNRAS*, **414**, 1903  
 Goulding, A. D., Zakamska, N. L., Alexandroff, R. M., et al. 2018, *ApJ*, **856**, 4  
 Hahn, C., Tinker, J. L., & Wetzel, A. 2017, *ApJ*, **841**, 6  
 Harrison, C. M., Alexander, D. M., Mullaney, J. R., & Swinbank, A. M. 2014, *MNRAS*, **441**, 3306  
 Harrison, C. M., Alexander, D. M., Swinbank, A. M., et al. 2012, *MNRAS*, **426**, 1073  
 Hönig, S. F., & Kishimoto, M. 2017, *ApJL*, **838**, L20  
 Hopkins, P. F., Hernquist, L., Cox, T. J., et al. 2006, *ApJS*, **163**, 1  
 Hopkins, P. F., Hernquist, L., Cox, T. J., & Kereš, D. 2008, *ApJS*, **175**, 356  
 Hou, L. G., Han, J. L., Kong, M. Z., & Wu, X.-B. 2011, *ApJ*, **732**, 72  
 Huchra, J. P., Macri, L. M., Masters, K. L., et al. 2012, *ApJS*, **199**, 26  
 Hwang, H. S., Serjeant, S., Lee, M. G., Lee, K. H., & White, G. J. 2007, *MNRAS*, **375**, 115  
 Ichikawa, K., Imanishi, M., Ueda, Y., et al. 2014, *ApJ*, **794**, 139  
 Ichikawa, K., Ricci, C., Ueda, Y., et al. 2017, *ApJ*, **835**, 74  
 Ichikawa, K., Ricci, C., Ueda, Y., et al. 2019, *ApJ*, **870**, 31  
 Inayoshi, K., Ichikawa, K., & Haiman, Z. 2018, *ApJL*, **863**, L36  
 Indebetouw, R., Mathis, J. S., Babler, B. L., et al. 2005, *ApJ*, **619**, 931  
 Ishibashi, W., Fabian, A. C., & Canning, R. E. A. 2013, *MNRAS*, **431**, 2350  
 Isobe, T., Feigelson, E. D., Akritas, M. G., & Babu, G. J. 1990, *ApJ*, **364**, 104  
 Isobe, T., Feigelson, E. D., & Nelson, P. I. 1986, *ApJ*, **306**, 490  
 Johansson, P. H., Naab, T., & Burkert, A. 2008, *AN*, **329**, 956  
 Jones, A. P., Fanciullo, L., Köhler, M., et al. 2013, *A&A*, **558**, A62  
 Kartaltepe, J. S., Sanders, D. B., Le Floch, E., et al. 2010, *ApJ*, **721**, 98  
 Kauffmann, G., & Haehnelt, M. 2000, *MNRAS*, **311**, 576  
 Kauffmann, G., Heckman, T. M., Tremonti, C., et al. 2003, *MNRAS*, **346**, 1055  
 Kennicutt, R. C. J. 1998, *ARA&A*, **36**, 189  
 Kewley, L. J., Dopita, M. A., Sutherland, R. S., Heisler, C. A., & Trevena, J. 2001, *ApJ*, **556**, 121  
 Kileric Eser, E., Goto, T., & Doi, Y. 2014, *ApJ*, **797**, 54  
 Kirkpatrick, A., Pope, A., Alexander, D. M., et al. 2012, *ApJ*, **759**, 139  
 Köhler, M., Jones, A., & Ysard, N. 2014, *A&A*, **565**, L9  
 Kroupa, P. 2001, *MNRAS*, **322**, 231  
 Lavalley, M., Isobe, T., & Feigelson, E. 1992, in ASP Conf. Ser. 25, Astronomical Data Analysis Software and Systems I, ed. D. M. Worrall, C. Biemesderfer, & J. Barnes (San Francisco, CA: ASP), 245  
 Liu, G., Zakamska, N. L., Greene, J. E., Nesvadba, N. P. H., & Liu, X. 2013, *MNRAS*, **436**, 2576  
 Łokas, E. L., & Mamon, G. A. 2001, *MNRAS*, **321**, 155  
 Luridiana, V., Morisset, C., & Shaw, R. A. 2015, *A&A*, **573**, A42  
 Lyu, J., & Rieke, G. H. 2018, *ApJ*, **866**, 92  
 Maiolino, R., Russell, H. R., Fabian, A. C., et al. 2017, *Natur*, **544**, 202  
 Makarov, D., Prugniel, P., Terekhova, N., Courtois, H., & Vauglin, I. 2014, *A&A*, **570**, A13  
 Malek, K., Bankowicz, M., Pollo, A., et al. 2017, *A&A*, **598**, A1  
 Manzano-King, C. M., Canalizo, G., & Sales, L. V. 2019, *ApJ*, **884**, 54  
 Marconi, A., Risaliti, G., Gilli, R., et al. 2004, *MNRAS*, **351**, 169  
 Markwardt, C. B. 2009, in ASP Conf. Ser. 411, Astronomical Data Analysis Software and Systems XVIII, ed. D. A. Bohlender, D. Durand, & P. Dowler (San Francisco, CA: ASP), 251  
 Mateos, S., Alonso-Herrero, A., Carrera, F. J., et al. 2012, *MNRAS*, **426**, 3271  
 Mateos, S., Carrera, F. J., Barcons, X., et al. 2017, *ApJL*, **841**, L18  
 Mathis, J. S., Mezger, P. G., & Panagia, N. 1983, *A&A*, **500**, 259  
 Mihos, J. C., & Hernquist, L. 1996, *ApJ*, **464**, 641  
 Moshir, M., et al. 1990, IRAS Faint Source Catalogue, version 2.0, 251  
 Moster, B. P., Naab, T., & White, S. D. M. 2013, *MNRAS*, **428**, 3121  
 Navarro, J. F., Frenk, C. S., & White, S. D. M. 1996, *ApJ*, **462**, 563  
 Nersesian, A., Xilouris, E. M., Bianchi, S., et al. 2019, *A&A*, **624**, A80  
 Netzer, H. 2009, *MNRAS*, **399**, 1907  
 Netzer, H., Lutz, D., Schweitzer, M., et al. 2007, *ApJ*, **666**, 806  
 Noll, S., Burgarella, D., Giovannoli, E., et al. 2009, *A&A*, **507**, 1793  
 Peng, Y.-j., & Maiolino, R. 2014, *MNRAS*, **443**, 3643  
 Perna, M., Brusa, M., Cresci, G., et al. 2015, *A&A*, **574**, A82  
 Popescu, C. C., Tuffs, R. J., Dopita, M. A., et al. 2011, *A&A*, **527**, A109  
 Reines, A. E., & Volonteri, M. 2015, *ApJ*, **813**, 82  
 Reipurth, B., & Schneider, N. 2008, Handbook of Star Forming Regions, Volume I (San Francisco, CA: ASP), 36  
 Rigopoulou, D., Spoon, H. W. W., Genzel, R., et al. 1999, *AJ*, **118**, 2625  
 Rodríguez Zaurín, J., Tadhunter, C. N., & González Delgado, R. M. 2010, *MNRAS*, **403**, 1317  
 Rodríguez Zaurín, J., Tadhunter, C. N., Rose, M., & Holt, J. 2013, *MNRAS*, **432**, 138  
 Ross, N. P., Hamann, F., Zakamska, N. L., et al. 2015, *MNRAS*, **453**, 3932  
 Rupke, D. S., Veilleux, S., & Sanders, D. B. 2005, *ApJ*, **632**, 751  
 Rupke, D. S. N., & Veilleux, S. 2011, *ApJL*, **729**, L27  
 Rupke, D. S. N., & Veilleux, S. 2013, *ApJ*, **768**, 75  
 Saito, T., Iono, D., Espada, D., et al. 2017, *ApJ*, **834**, 6  
 Salim, S., Rich, R. M., Charlot, S., et al. 2007, *ApJS*, **173**, 267  
 Salpeter, E. E. 1955, *ApJ*, **121**, 161  
 Sanders, D. B., & Mirabel, I. F. 1996, *ARA&A*, **34**, 749  
 Sanders, D. B., Soifer, B. T., Elias, J. H., et al. 1988, *ApJ*, **325**, 74  
 Schartmann, M., Meisenheimer, K., Camenzind, M., Wolf, S., & Henning, T. 2005, *A&A*, **437**, 861  
 Schlafly, E. F., & Finkbeiner, D. P. 2011, *ApJ*, **737**, 103  
 Schlegel, D. J., Finkbeiner, D. P., & Davis, M. 1998, *ApJ*, **500**, 525  
 Schmitt, J. H. M. M. 1985, *ApJ*, **293**, 178  
 Shen, S., Mo, H. J., White, S. D. M., et al. 2003, *MNRAS*, **343**, 978  
 Shu, F. H., Adams, F. C., & Lizano, S. 1987, *ARA&A*, **25**, 23  
 Skrutskie, M. F., Cutri, R. M., Stiening, R., et al. 2006, *AJ*, **131**, 1163

- Sofue, Y., Honma, M., & Omodaka, T. 2009, *PASJ*, 61, 227
- Soto, K. T., Martin, C. L., Prescott, M. K. M., & Armus, L. 2012, *ApJ*, 757, 86
- Stalevski, M., Asmus, D., & Tristram, K. R. W. 2017, *MNRAS*, 472, 3854
- Stalevski, M., Fritz, J., Baes, M., Nakos, T., & Popović, L. Č. 2012, *MNRAS*, 420, 2756
- Stalevski, M., Ricci, C., Ueda, Y., et al. 2016, *MNRAS*, 458, 2288
- Stéphan, G., Schilke, P., Le Bourlot, J., et al. 2018, *A&A*, 617, A60
- Storey, P. J., & Hummer, D. G. 1995, *MNRAS*, 272, 41
- Stoughton, C., Lupton, R. H., Bernardi, M., et al. 2002, *AJ*, 123, 485
- Su, S., Kong, X., Li, J., & Fang, G. 2013, *ApJ*, 778, 10
- Toba, Y., Bae, H.-J., Nagao, T., et al. 2017a, *ApJ*, 850, 140
- Toba, Y., Nagao, T., Wang, W.-H., et al. 2017b, *ApJ*, 840, 21
- Toomre, A. 1977, in *Evolution of Galaxies and Stellar Populations*, ed. B. M. Tinsley, D. C. Larson, & R. B. Gehret (New Haven, CT: Yale Univ. Observatory), 401
- Tsuzuki, Y., Kawara, K., Yoshii, Y., et al. 2006, *ApJ*, 650, 57
- Ueda, Y., Hashimoto, Y., Ichikawa, K., et al. 2015, *ApJ*, 815, 1
- Urrutia, T., Lacy, M., & Becker, R. H. 2008, *ApJ*, 674, 80
- Vanden Berk, D. E., Richards, G. T., Bauer, A., et al. 2001, *AJ*, 122, 549
- Veilleux, S., Cecil, G., & Bland-Hawthorn, J. 2005, *ARA&A*, 43, 769
- Veilleux, S., Kim, D.-C., Peng, C. Y., et al. 2006, *ApJ*, 643, 707
- Veilleux, S., Meléndez, M., Sturm, E., et al. 2013, *ApJ*, 776, 27
- Veilleux, S., Rupke, D. S. N., Kim, D.-C., et al. 2009, *ApJS*, 182, 628
- Véron-Cetty, M. P., Joly, M., & Véron, P. 2004, *A&A*, 417, 515
- Vestergaard, M., & Wilkes, B. 2001, in *ASP Conf. Ser. 247, Spectroscopic Challenges of Photoionized Plasmas*, ed. G. Ferland & D. W. Savin (San Francisco, CA: ASP), 359
- Westmoquette, M. S., Clements, D. L., Bendo, G. J., & Khan, S. A. 2012, *MNRAS*, 424, 416
- Wright, E. L., Eisenhardt, P. R. M., Mainzer, A. K., et al. 2010, *AJ*, 140, 1868
- Wright, R. J., Lagos, C. D. P., Davies, L. J. M., et al. 2019, *MNRAS*, 487, 3740
- Xu, L., Rieke, G. H., Egami, E., et al. 2015, *ApJS*, 219, 18
- Zakamska, N. L., & Greene, J. E. 2014, *MNRAS*, 442, 784